Numerical simulation approaches and methodologies for multi-physic comprehensions of titanium alloy (Ti–6Al–4V) CUTTING

Yancheng Zhang

No. d' ordre: 2011ISAL0098 **Année 2011**

THESE

Présentée devant

(INSTITUT NATIONAL DES SCIENCES APPLIQUEES DE LYON)

Pour obtenir

LE GRADE DE DOCTEUR

Ecole Doctorale des Sciences de l'Ingénieur de Lyon:

Mécanique, Energétique, Génie civil, Acoustique (MEGA)

Spécialité:

MECANIQUE – GENIE MECANIQUE

Par

Yancheng ZHANG

NUMERICAL SIMULATION APPROACHES AND METHODOLOGIES FOR MULTI-PHYSIC COMPREHENSIONS OF TITANIUM ALLOY (Ti–6Al–4V) CUTTING

APPROCHES NUMERIQUES ET METHODOLOGIES POUR UNE COMPREHENSION MULTI-PHYSIQUES DE LA COUPE DE L'ALLIAGE DE TITANE (Ti–6Al–4V)

Thèse soutenue le 29 septembre 2011 devant la commission d'examen

Rapporteurs :	
Amine AMMAR	Professeur des universités (ENSAM ParisTech, France)
Olivier CAHUC	Professeur des universités (Université de Bordeaux I, France)
Examinateurs :	
Domenico UMBRELLO	Professeur des universités (Università della Calabria, Italy)
Hédi HAMDI	Maître de Conférences/HDR (ENISE, France)
Jean François RIGAL	Professeur des universités (INSA de Lyon, France)
Invité :	
Mathias SEVE	Ingénieur procédés d'usinage (SNECMA, France)
Directeurs de thèse :	
Tarek MABROUKI	Maître de Conférences (INSA de Lyon, France)
Daniel NELIAS	Professeur des universités (INSA de Lyon, France)

LaMCoS, INSA-Lyon, CNRS UMR5259, F69621.
(Laboratoire de Mécanique des Contacts et des Structures)
20, Av. Albert Einstein, 69621 Villeurbanne Cedex, France.

INSA Direction de la Recherche - Ecoles Doctorales – Quinquennal 2011-2015

SIGLE	ECOLE DOCTORALE	NOM ET COORDONNEES DU RESPONSABLE
CHIMIE	**CHIMIE DE LYON** **http://www.edchimie-lyon.fr** Insa : R. GOURDON	M. Jean Marc LANCELIN Université de Lyon – Collège Doctoral Bât ESCPE 43 bd du 11 novembre 1918 69622 VILLEURBANNE Cedex Tél : 04.72.43 13 95 directeur@edchimie-lyon.fr
E.E.A.	**ELECTRONIQUE, ELECTROTECHNIQUE, AUTOMATIQUE** **http://edeea.ec-lyon.fr** Secrétariat : M.C. HAVGOUDOUKIAN eea@ec-lyon.fr	M. Gérard SCORLETTI Ecole Centrale de Lyon 36 avenue Guy de Collongue 69134 ECULLY Tél : 04.72.18 60 97 Fax : 04 78 43 37 17 Gerard.scorletti@ec-lyon.fr
E2M2	**EVOLUTION, ECOSYSTEME, MICROBIOLOGIE, MODELISATION** **http://e2m2.universite-lyon.fr** Insa : H. CHARLES	Mme Gudrun BORNETTE CNRS UMR 5023 LEHNA Université Claude Bernard Lyon 1 Bât Forel 43 bd du 11 novembre 1918 69622 VILLEURBANNE Cédex Tél : 04.72.43.12.94 e2m2@univ-lyon.fr
EDISS	**INTERDISCIPLINAIRE SCIENCES-SANTE** **http://ww2.ibcp.fr/ediss** Sec : Safia AIT CHALAL Insa : M. LAGARDE	M. Didier REVEL Hôpital Cardiologique de Lyon Bâtiment Central 28 Avenue Doyen Lépine 69500 BRON Tél : 04.72.68 49 09 Fax :04 72 35 49 16 Didier.revel@creatis.uni-lyon1.fr
INFOMATHS	**INFORMATIQUE ET MATHEMATIQUES** http://infomaths.univ-lyon1.fr	M. Johannes KELLENDONK Université Claude Bernard Lyon 1 LIRIS - INFOMATHS Bâtiment Nautibus 43 bd du 11 novembre 1918 69622 VILLEURBANNE Cedex Tél : 04.72. 43.19.05 Fax 04 72 43 13 10 infomaths@bat710.univ-lyon1.fr
Matériaux	**MATERIAUX DE LYON** Secrétariat : M. LABOUNE PM : 71.70 –Fax : 87.12 Bat. Saint Exupéry	M. Jean-Yves BUFFIERE INSA de Lyon MATEIS Bâtiment Saint Exupéry 7 avenue Jean Capelle 69621 VILLEURBANNE Cédex Tél : 04.72.43 83 18 Fax 04 72 43 85 28 Jean-yves.buffiere@insa-lyon.fr
MEGA	**MECANIQUE, ENERGETIQUE, GENIE CIVIL, ACOUSTIQUE** Secrétariat : M. LABOUNE PM : 71.70 –Fax : 87.12 Bat. Saint Exupéry mega@insa-lyon.fr	M. Philippe BOISSE INSA de Lyon Laboratoire LAMCOS Bâtiment Jacquard 25 bis avenue Jean Capelle 69621 VILLEURBANNE Cedex Tél :04.72.43.71.70 Fax : 04 72 43 72 37 Philippe.boisse@insa-lyon.fr
ScSo	**ScSo*** M. OBADIA Lionel Sec : Viviane POLSINELLI Insa : J.Y. TOUSSAINT	M. OBADIA Lionel Université Lyon 2 86 rue Pasteur 69365 LYON Cedex 07 Tél : 04.78.69.72.76 Fax : 04.37.28.04.48 Lionel.Obadia@univ-lyon2.fr

*ScSo : Histoire, Geographie, Aménagement, Urbanisme, Archéologie, Science politique, Sociologie, Anthropologie

To Parents
&
Wife

Acknowledgments

This thesis would have not been possible without the support and confidence of my advisors. I would like to express my heartfelt thanks to Professor D. Nelias for accepting me as his student and give me his wise guidance. His scientific expertise in the numerical simulation of mechanical problems especially contact is the most impressive. I really appreciate the help of my co-advisor: Prof. T. Mabrouki shared his knowledge in the modeling of machining, the experimental design, especially the never-ending patience and encouragement for my research work.

I would like to thank the rest of committee numbers, Prof. A. Ammar, Prof. O. Cahuc, Prof. D. Umbrello, Prof. A. Hamdi, M. M. SEVE, and Prof. J. F. Rigal for their time, and valuable comments to improve the quality of this work.

I would like to express my special thanks to Prof. Y. Gong (Northeastern University, China) who helps me get the finical support for the thesis and develop the cooperation between LaMCoS and AMI (Advanced Manufacturing Institute, China).

I would like to thank C. Courbon, M. Asad, A. Mondelin, Syed Mushtaq Ahmed Shah for discussing the simulation and experimental problem of cutting. The help form my collogues: T. Chaise, G. Beaurin, C. Bagault, J. Li, J. Leroux., F. Caleyron, B. Trolle, A. Brunon, B. Fulleringer … And my collogues from China: J. Cheng, J. Qiu, Y. Liu, J. Wang, and F. Liu.

Thanks should be also addressed for the discussion with the professors from LaMCoS, Prof. M. Brunet, Prof. H. Maigre, and Dr. M. Coret, and the experimental support from Prof. J. Rech (ENISE), M. P. Polly (ENISE) and M. C. Godeau for their valuable help in the machining test and the preparation of specimens.

I would like to acknowledge the financial assistance provided by the China Scholarship Council (CSC) from China in collaboration with French government through an Overseas Research scholarship Program.

Finally, I would like to take this opportunity to express my heartfelt thanks to my parents, my wife, my aunt, my sisters and my brothers for their utmost love and constant encouragement. Special thanks to Jikai Liu, Jing Xie, Zhe Li, Ting Li, Senbin Chen, Jing Wang for their unremitting support, friendship and understanding during this time.

It's the early birds that get the worm, and please learn to walk before you run.

Abstract

The objective of this study is to model material removal with cutting tool in the case of the machining of Titanium alloy (Ti–6Al–4V) and to bring a multi-physic comprehension of chip formation and the tool/workpiece interaction by adopting finite element approaches and methodologies.

For that, the present contribution begins by a macroscopic modeling of the orthogonal cutting process. The cut material behavior considered is supposed based on JC law. Moreover, in order to simulate properly the chip genesis, the material fracture energy concept is adopted for controlling the material damage evolution. This allows capturing the shear strain localization and consequently the chip segmentation for a given set of cutting parameters. The frictional contact model considers the influence of temperature on the limiting shear stress at the tool/chip interface. As a result, this reliable model has the capability to simulate the cutting process even with high coefficient of friction and with large cutting edge radius. The parametric study carried out by referring to this model shows a very interesting corroboration with experimental results.

In a second step, the present research work presents a material microstructure-level cutting model (MML cutting model) for cutting simulation. The crystal plasticity theory is adopted for modeling the cutting of the Titanium alloy Ti–6Al–4V in orthogonal case. In this model, the grains of the studied material are explicitly considered, and their orientation angles and slip system strength anisotropy are considered as the main source of the microstructure heterogeneity in the cutting material. To simulate the material degradation process, the continuum intra-granular damage and discrete cohesive zone inter-granular damage models are developed, wherein the zero thickness cohesive elements are implemented to simulate the bond between grain interfaces. The material model is validated by a comparison of compression tests from literature.

Finally, simulation results demonstrate the possibility to capture the influence of the microstructure on the material removal in terms of chip formation. It is demonstrated that the grain orientation angle plays an important role for the chip segmentation and its periodicity during the cutting process. This certainly can affect the evolution of the cutting force. Additionally, the surface integrity is discussed based on the MML cutting model for different

cutting speeds and feed rates. Indeed, a parametric study shows that the surface integrity is seriously affected by the machining parameters, and the affected region is limited within three layer grains for the present MML cutting model.

Keywords: Finite element simulation, Orthogonal cutting model, Johnson-Cook, Fracture energy, Damage evolution, Limiting shear stress, Material microstructure-level cutting model (MML cutting model), Crystal plasticity, Intra-granular damage model, Inter-granular damage model, Vumat user routine, Ti–6Al–4V, Surface integrity.

Résumé

Ce travail de thèse est focalisé sur l'établissement d'un modèle de coupe orthogonale simulant l'usinage de l'alliage de Titane (Ti–6Al–4V). L'objectif principal est de contribuer à des approches et des méthodologies numériques permettant la modélisation de la formation du copeau de ce type d'alliage et l'amélioration de la compréhension des phénomènes multi-physiques induits par l'enlèvement de matière et qui découle de l'interaction outil-matière.

Pour se faire, ce travail de recherche commence par la présentation d'une méthodologie macroscopique et robuste permettant d'établir un modèle de coupe en adoptant la loi de comportement phénoménologique de Johnson et Cook. L'une des améliorations apportées dans ce modèle consiste à adopter le critère de l'énergie de rupture pour contrôler l'évolution de l'endommagement de la matière et pouvoir par conséquent simuler pertinemment la genèse du copeau. Cela a permis de capturer la localisation de la déformation maximale par cisaillement et par la suite de dimensionner les formes caractéristiques liées au phénomène de segmentation du copeau selon les conditions de coupe adoptées. Le modèle de frottement à l'interface outil-matière découpée a également été affiné en intégrant une contrainte de cisaillement limite à l'interface copeau-outil. L'effet de la température sur cette contrainte limite a également été considéré et implémenté dans une routine utilisateur. Cela a permis de modéliser la formation du copeau même sous des conditions de frottement agressives et avec des rayons d'acuité d'arête de coupe élevés. L'étude paramétrique ainsi effectuée montre une très bonne adéquation avec les résultats expérimentaux.

Dans un second temps un modèle qui peut-être qualifié de multi-echelles a été élaboré. Ce modèle de coupe tient compte de la microstructure du matériau à découper. Il est basé sur la théorie de la plasticité cristalline pour simuler la coupe orthogonale de l'alliage de Titane Ti–6Al–4V. Dans cette approche, les grains de la matière traitée sont présentés explicitement dans le maillage avec des formes hexagonales caractérisées par différentes orientations et systèmes de glissement. Dans ce cas d'étude le processus de dégradation de la matière sous différentes sollicitations thermomécaniques est le résultat de la cœxistence de deux types d'endommagement. En effet, il est supposé une rupture de la matière au niveau des grains qualifiée de dommage intra-granulaire et un dommage éventuel, aux interfaces des grains, qualifié d'inter-granulaire. Ce dernier est simulé par des éléments cohésifs d'épaisseurs nulles

traduisant la possibilité de la décohésion des gains de la matière. Ce modèle est validé par des résultats de compression provenant de la littérature.

Les résultats de la simulation montrent la possibilité de reproduire l'influence de la microstructure sur la morphologie du copeau formé au cours du processus de coupe. L'un des apport originaux de cette thèse est de démontrer que l'orientation du grain joue un rôle primordial quant au phénomène de la segmentation du copeau et sa périodicité. Cela affectera certainement l'évolution de l'effort de coupe et l'intégrité de la surface générée. Cette approche de modélisation numérique est complétée par une étude paramétrique mettant en exergue l'évolution de certains critères qualifiant l'intégrité de la surface en fonction des conditions de coupe.

Mots Clés: Simulation éléments finis, Modèle de coupe orthogonale, Johnson-Cook, Energie de rupture, Modèle de découpe de matériaux microstructure, Evolution de l'endommagement intra-granulaire, modèle d'endommagement inter-granulaire, Routine utilisateur VUMAT, Ti–6Al–4V, Intégrité de surface.

Contents

List of figures

List of tables

Nomenclature

Symbols	Signification	Symbols	Signification
A	Initial yield stress (MPa) (JC)	P	Hydrostatic pressure
a	Half contact width (mm)	P_c	Contact force per unit length (N/mm) (MPa)
a_p	Cutting depth (mm)	p_0	Maximum contact pressure (N/mm^2)
B	Hardening modulus (MPa) (JC)	q_o	Tangential traction at $x = 0$ (N/mm^2)
C	Strain rate dependency coefficient (MPa)	R	Radius of a cylinder (mm)
C_p	Specific heat ($J/kg^{-1}C^{-1}$)	R_n	Cutting edge radius (μm)
D	Overall damage variable	S	Deviatoric stress (MPa)
$D_1 \ldots D_5$	Coefficients of Johnson-Cook material shear failure initiation criterion	t_c	Cutting time (μs)
E_1	Tool insert Young's modulus (MPa)	t_i	Time increment
E_2	Machined material Young's modulus (MPa)	$\bar{u}_F^p$	Equivalent plastic displacement at failure (mm)
e	Strain deviator	$\bar{u}^p$	Equivalent plastic displacement (mm)
f	Feed rate (mm/rev)	V_c	Cutting speed (m/min)
f_c	Chip segmentation frequency (kHz)	V_{chip}	Local chip sliding speed (m/min)
F_c	Cutting force (N)		
F_f	Feed force (N)		
G_f	Fracture energy (N/m)		
G	Shear modulus (MPa)		
K	Bulk modulus (MPa)		
K_C	Fracture toughness ($MPa\sqrt{m}$)		
L	Characteristic length (mm)		
L_c	Chip segmentation wavelength (mm)		
m	Thermal softening coefficient (JC)		
m_1	Contact coefficient		
N	Work-hardening exponent		
n_1	Contact coefficient		

Nomenclature

Symbols	Signification	Symbols	Signification
α_0	Flank angle (deg)	σ_I	Principal stresses (I=1…3) (MPa)
α_d	Expansion coefficient (μm/m/ºC)		
γ	Shear strain in the primary shear zone	$\bar{\sigma}_{JC}$	Johnson-Cook plastic equivalent stress (MPa)
γ_0	Rake angle (deg)		
$\dot{\bar{\varepsilon}}^p$	Equivalent plastic strain rate (s^{-1})		
$\dot{\bar{\varepsilon}}_0^p$	Reference plastic strain rate ($1s^{-1}$)	$\bar{\sigma}$	von Mises equivalent stress (MPa)
$\bar{\varepsilon}_{0i}$	Equivalent plastic strain at the onset of damage	σ_Y	Yield stress (MPa)
$\bar{\varepsilon}_F^{\,p}$	Equivalent plastic strain at failure	τ_f	Limiting shear stress (MPa)
$\Delta\bar{\varepsilon}^p$	Equivalent plastic strain increment	τ_Y	Shear stress calculated by yield stress (MPa)
$\bar{\varepsilon}^p$	Plastic strain		
θ_w	Workpiece computed temperature (ºC)		
θ_m	Melting temperature of the Titanium alloy Ti-6Al-4V (1630°C)		
θ_o	Room temperature (25 °C)		
λ	Thermal conductivity (W/m/ºC)		
μ	Value of coefficient of friction (CoF)		
N	Poisson's ratio		
υ	Volumetric strain		
ρ	Density (kg/m^3)		
ω	Damage initiation criterion		

Nomenclature (MML cutting model)

Symbols	Signification	Symbols	Signification
α_P α_S β	Primary α phase Second α phase β phase	γ_p^s	Plastic strain to determine the damage initiation in slip system
α_T	Taylor model related coefficient	γ_p^c	Plastic strain for complete damage in slip system
φ_1, Φ, φ_2	Euler angles from specimen coordinate system to the crystal coordinate system	$d_C{}^\alpha$	Critical damage in slip system
		Δd_{NC}^α	Damage increment without correction
$\mathbf{C}_c$ $\mathbf{C}_s$	Base vector matrix representing the crystal coordinate Basic vector matrix representing the specimen coordinate system	τ_c, a_D	Coefficient in the delayed damage model
		c, d,	Related coefficient for describing the kinematic hardening in the slip system
$\mathbf{g}=\mathbf{g}_{\varphi_2}\cdot\mathbf{g}_\Phi\mathbf{g}_{\varphi_1}$	Transformation matrix relating the specimen and crystal coordinate systems	R_0, Q, b, n ,m	Related coefficient for describing the kinematic hardening in the slip system
τ^α	Resolved shear stress in the slip system	$\underline{\underline{\sigma}}^g$	Stress tensor of the grain
x^α	Kinematic hardening in the slip system	$\underline{\underline{\varepsilon}}^{pg}$	Plastic strain tensors of a grain
		f^g	Volume fraction of grains having the same orientation
r^α	Isotropic hardening in the slip system	$\underline{\underline{\underline{\underline{\Lambda}}}}$	Fourth order elastic properties tensor
$\dot{\gamma}^\alpha$	Viscoplastic slip rate		
γ_{cum}^α	The accumulated slip	k_n	Stiffness of cohesive zone in normal direction
$\underline{\underline{\mu}}^\alpha$	The Schmid factor		
$\bar{n}^\alpha$, $\bar{m}^\alpha$	The normal to the slip plane and the slip direction of the slip system, respectively.	k_t	Stiffness of cohesive zone in tangential direction

Nomenclature (MML cutting model)

Symbols	Signification	Symbols	Signification
T_n^0, T_t^0	Material parameters specifying the normal and tangential fracture strengths of the cohesive zone		
δ_n^0, δ_t^0	Traction displacements in normal and tangential directions, respectively		
δ_n^1, δ_t^1	The maximum values of δ_n and δ_t achieved during prior loading		
δ_c	The critical opening displacement for total failure		
D_n, D_t	Damage variables for describing the traction process		

List of abbreviations

Abbreviations	Full names
ALE	Arbitrary Lagrangian-Eulerian formulation
BCC	Body-centred cubic
CoF	Coefficient of friction
CRSS	Critical shear stress
CSS	Crystallographic Slip Systems
DRX	The dynamic recrystallization
FE	Finite element
GOA	Grain orientation angle
HCP	Hexagonal close-packed
ISV	Internal state variable
J-C	Johnson-Cook
MML	Material microstructure-level
REV	Representative Volume Element
RS	Residual stress
SDEG	Scalar stiffness degradation
UCT	Undeformed chip thickness
2D/3D	Two/Three dimensional model
ODF	Orientation distribution function

Introduction

Due to the appreciated characteristics such as high strength-to-weight ratio, low coefficient of expansion, their ductility and excellent corrosion resistance even at high temperature, the Titanium and its alloys have received considerable interest with wide range of applications in aerospace (Fig. 0.0.1), automotive, chemical, and medical industry [ARR09].

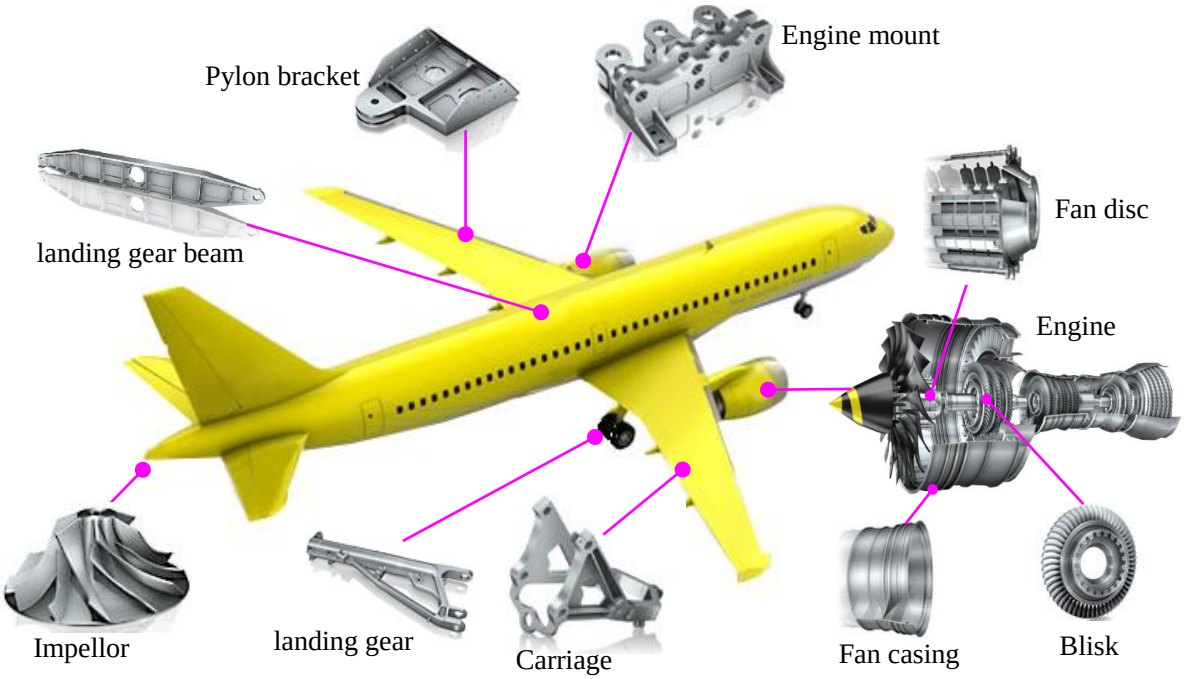

Fig. 0.0.1 Typical aerospace parts shaped by machining [SAN11]

However, Titanium alloys are classified as hard machining materials because of their high chemical reactivity and low thermal conductivity [PUE07]. The high chemical reactivity increases with temperature and produces an early damage of the cutting tool affecting the surface quality and increasing the production costs. Their low thermal conductivity hinders

the evacuation of the heat generated during the cutting process resulting in a temperature rise of the workpiece [EZU09].

In order to increase productivity and tool-life in machining of Titanium alloys, it is necessary to study the physics of chip segmentation and the effects of the working parameter variation on material cutting performance. For that, it is interesting to build a reliable finite element model (FE-model) allowing more understanding of the tool-workpiece interaction during the cutting of this type of material.

In this general framework, this thesis aims to study and improve the machining technologies, from both macro and micro aspects, for the widely used Titanium alloy (Ti–6Al–4V). Particularly, the essential key of the present work is to bring a multi-physical comprehension concerning the chip formation and its consequences on tool-workpiece interaction via the elaboration of numerical cutting models.

Problem statement and objectives

Various thermo-mechanical models of macro and micro-cutting processes have been presented by numerous researchers [CHU02, MAB08]. Nevertheless, the robustness of a given numerical model is strongly dependent on the material constitutive model, material fracture criterion, the work material contact nature at cutting tool-chip interface, both tool and workpiece material thermal parameters [BON08, UMB08], etc. Consequently, many scientific problems are still open for discussion according to the elaborated cutting model, e.g., the friction contact behaviour between the tool and the chip is still not clear according to the given formulae [DIR01, OBI00], especially when the temperature influence is considered. What's more, the approach of cutting model considering microstructure of Ti–6Al–4V has not been yet reported. At the same time, the integrity of the machined surface seems more complex to be modelled because of the material characteristic of α, β phases. So, the specific objectives of this thesis could be underlined as following:

1) The exploitation of a robust FE model to simulate 2D orthogonal cutting with segmented chip formation.

2) Improvement of the friction contact model at the tool/chip interface from the aspect of contact mechanics, to incorporate the influence of coefficient of friction (CoF) and temperature variation. This aim is to resolve the element distortion of the new formed chip surface even for high friction coefficient.

3) Development of a cutting model considering the material microstructure and the crystal plasticity theory. The intra-granular ductile damage model and inter-granular cohesive damage model are used to simulate two kinds of damage to better describe the material degradation. One of the objectives here is to highlight the importance of grain orientation angle (GOA) on the chip morphology.

4) Investigation of the integrity of the machined surface, considering the effect of the phase texture for the residual stress profile along the normal direction of the machined surface.

Outlines of the thesis

For a clear and comprehensive presentation of the scientific research work, the manuscript is organized in four chapters.

In chapter one, a literature review on the cutting process and the FE modeling of machining process for the aeronautical material Ti–6Al–4V is provided. A literature review on the importance of the cutting material microstructure for studying the machinability of Titanium alloy Ti–6Al–4V is considered.

Chapter two presents the elaborated cutting model based on the FE commercial code ABAQUS/Explicit. The material fracture energy is adopted for controlling the evolution of the damage within the material. This is considered to capture the shear strain localization and produce the segmented chip formation. Also, the friction contact model is improved by considering the influence of the temperature on the limiting the shear stress at the tool/chip interface. Finally, this reliable model has the capability to simulate the cutting process even with high coefficient of friction (CoF) and with large cutting edge radius.

In chapter three, the experimental studies for different cutting speeds and feed rates are performed firstly, and the chip and cutting forces are collected correspondingly. To qualify the pertinence degree of the new developed cutting model, a parametric calibration study is carried out with different rake angles and numerical results compared to experimental data. Based on the robust cutting model, the effects of various cutting speeds, CoFs, rake angles on the chip morphology are investigated. Furthermore, the residual stress prediction model is introduced, and the influence of tool flank wear on residual stress distribution is analysed.

In chapter four, a material microstructure level (MML) model for cutting simulation based on the crystal plasticity theory is adopted for modeling the cutting of the Titanium alloy Ti–6Al–4V in orthogonal case. In this model, the grains of the studied material are explicitly

presented, and their orientation angles and slip system strength anisotropy are considered as the main source of the microstructure heterogeneity in the machined material. To obtain the material degradation process, the continuum intra-granular damage and discrete cohesive zone inter-granular damage models have been implemented, wherein the zero thickness cohesive elements are introduced to simulate the bond between grain interfaces. The material model is validated by simulation of a compression test and results are compared with experimental data from the literature. Simulation results demonstrate the ability of the MML cutting model to capture the influence of the material microstructure, in terms of grain orientation angles, on the material removal during chip formation.

Based on the MML cutting model, the chip formation, temperature, equivalent plastic strain, and residual stress distribution are studied with different cutting speed and feed.

Finally, the manuscript is ended by a general conclusion including the major points outlined in this dissertation and a discussion of possible research directions in future as a continuation of the present contribution.

1 Cutting simulations: the current and future trend

1.1 Introduction

Metal cutting is one of the most widely used machining processes, in which the unnecessary material is removed by the action of a cutting edge of the tool. Moreover, it is one of the important processes inducing high rate material removal, allowing the cutting of complex geometry structure, permitting high precision surface with relatively small cost, etc. Recently, micromechanical cutting processes show their superiorities in producing devices concerned with bio-MEMS [WAN08].

In order to improve the cutting process, many methodologies were adopted in the past years with different studies' approaches. For that, the main researchers' aim was to well understand the generation of cutting forces, chip morphology, temperatures, and surface integrity. Indeed, lots of research works have been reported about machining processes and manufacturing productivity, wherein, the "Metal cutting principles" by Shaw [SHA84] is one of the first books that carefully discuss, in a descriptive way, the different parameters that influence the chip formation mechanism. Later, the analytical slip-line models taking into account chip curl were developed by Merchant [MER44] and Lee and Shaffer [LEE51]. Nevertheless, the study of metal cutting is still a challenging work after more than one century, due to the diversity of physical phenomena (Coupled thermo-mechanical algorithm, the ambiguities of friction/contact formulation, and the complicated chip separation criteria) involved in the cutting process.

Fortunately, the FE method brings new insights into the art of cutting studies from the pioneering works by Klamecki [KLA73], Usui and Shirakashi [SHI74, USU82], which makes

it possible to provide more precise information concerning variables like plastic strain, strain rate or stress during tool/workpiece interaction that are difficult to measure experimentally. Consequently, more knowledge about the chip genesis phenomenon can be deduced. As FE method takes into accounts both material thermo-mechanical behavior and contact non-linearity, it brings more accurate than analytical models [MER44].

Despite some limitations and constraints: difficulties in identification of input parameters, lack of robustness in some quantitative results and so on, numerical simulations still can be considered promising to study cutting process and potentially allowing to reduce the experimental cost [ARR05]. Moreover, it is noticed that during the last 60 years, numerous FE cutting models have been developed to understand the machinability of materials. Researchers have tried to improve the cutting model by modifying the material constitutive model, acting on contact algorithm, adopting different solving algorithms, or implementing the latest numerical techniques to get reliable and accurate prediction model. Correspondingly, this chapter emphasizes on the material microstructure properties studied in the present work, the principal of orthogonal cutting, the review on both Lagrangian and Eulerian cutting models. Moreover, a state on the art concerning on the material constitutive model, the thermal material properties, the tool-workpiece assumption in term of friction evolution, and the scale of macro to micro levels are defined, presented and discussed.

In the objective to elaborate a numerical model for cutting the Titanium alloy Ti–6Al–4V, it seems to be necessary to give the reader a succinct idea about the physical properties and the microstructure of this kind of material. This will help to apprehend some microstructure vocabulary used for the next.

1.2 Titanium alloy Ti–6Al–4V properties and microstructure

1.2.1 Composition and properties

The chemical composition of Titanium alloy Ti–6Al–4V is reported in Table 1.1. The Titanium (Ti), the Aluminium (Al), and the Vanadium (V) are the principal components. Although the additional elements (iron, oxygen, nitrogen, etc.) are present in very small quantities, they significantly alter the physical properties of the alloy. The physical properties are presented in Table 1.1 and Fig. 1.1. It can be seen that the value of thermal conductivity is very small even for the high temperature of 1000°C.

Description	Values
Al	5.50 – 6.75
C	≤ 0.0800
H	≤ 0.0150
Fe	≤ 0.400
N	≤0.300
O	≤ 0.200
Ti	87.725 - 91.0
V	3.50 - 4.50
Other, each	S<0.0500
Other, total	≤ 0.300
Young's modulus	210 GPa
Poisson ratio	0.3
Mass density	4430 kg/m^3
Specific heat (See Fig. 1.a)	J/kg/°C
Thermal conductivity (See Fig. 1.b)	W/m/°C

Table 1.1 Physical and chemical properties of Ti–6Al–4V [MAT08]

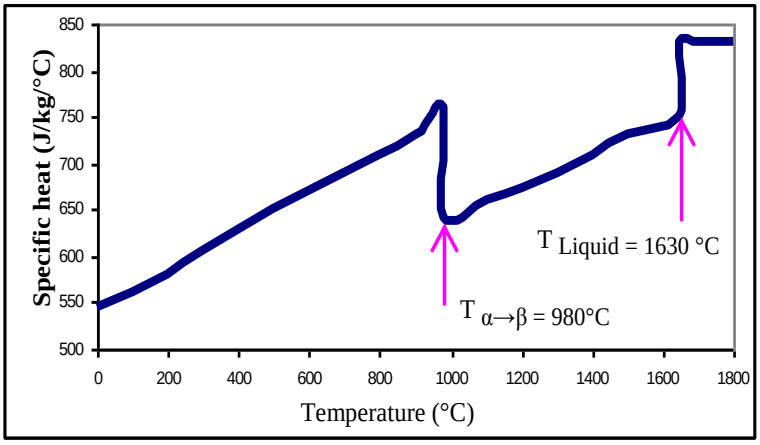

(a)

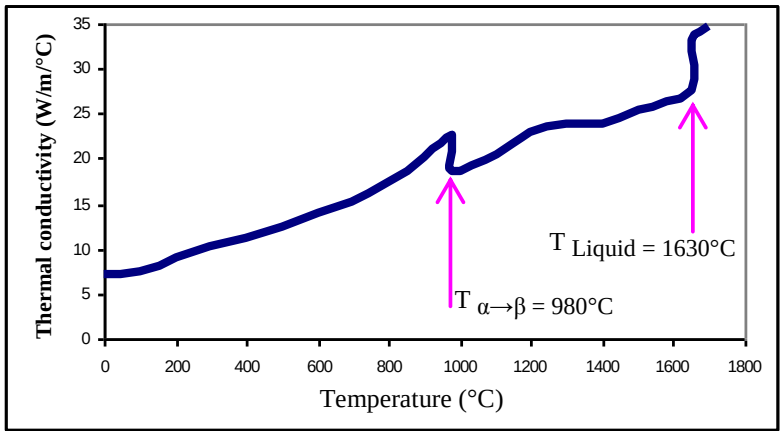

(b)

Fig. 1.1 Physical properties of the Ti–6Al–4V alloy as a function of temperature: (a) variation of specific heat and (b) variation of thermal conductivity [MIL02]

1.2.2 Material microstructure

The Titanium alloy Ti–6Al–4V is a typically formed two phases consisting of hexagonal close-packed (HCP) α-phase and body-centred cubic (BCC) β-phase. The material consists of a duplex structure with a 60 % volume fraction of equiaxed primary α-phase. The remaining 40 % consists of a lamellar structure of secondary α plate layered with β.

The temperature at which α phase changes to β (β-transus) depends on the compositions of (Al) and (V) (See Fig. 1.2). The β-transus is also sensitive to interstitial impurity; for example, higher amount of (O_2) will raise β-transus, whereas higher amounts of (Fe) will lower it. Depending on the processing conditions, this alloy can form two stable phases (α and β), two metastable phases (α' and α") and the intermetallic phase α_2 [BAD08].

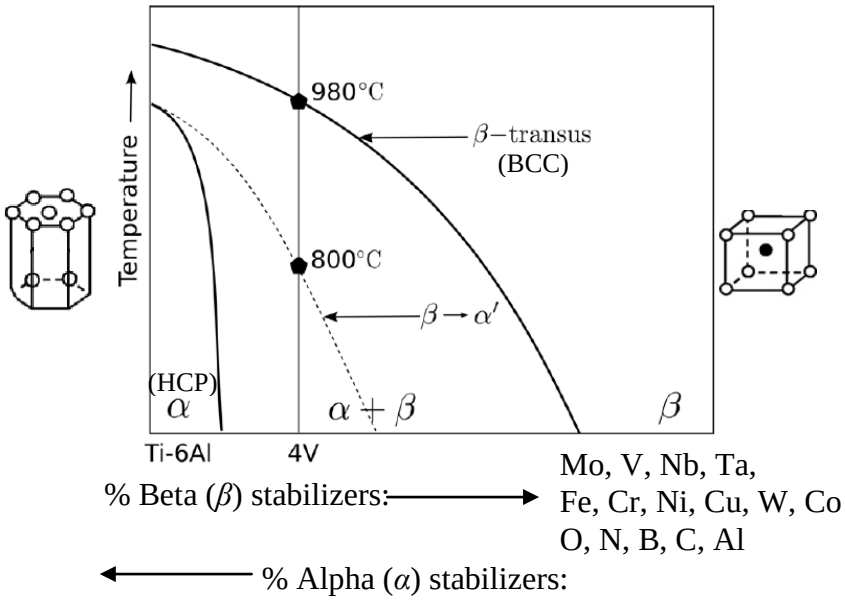

Fig. 1.2 Ternary phase diagram [BAD08]

When cooled from β - transus temperature (980°C), the HCP α - phase starts to form as plates with basal plane parallel to a special plane in β- phase. The growth is fast among the plates as compared to the perpendicular direction. Later, this develops to parallel to α plates with β trapped between them. Also, the plates formed parallel to one plane of β will meet plates formed with another plane which is demonstrated schematically in Fig. 1.3. This process is referred to as sympathetic nucleation an d growth which results in a structure commonly known as “Widmanstatten” [LUT03].

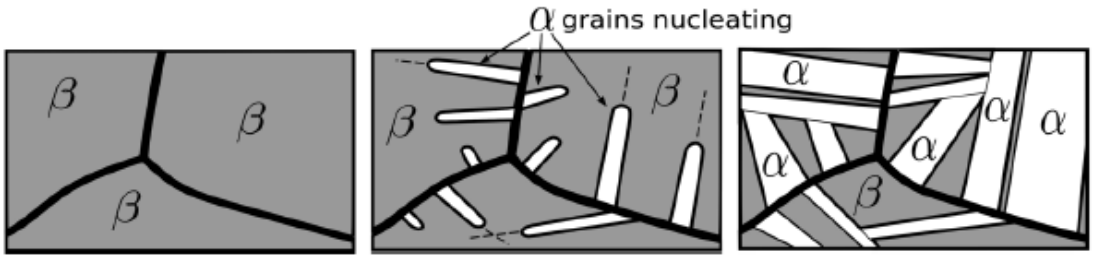

Fig. 1.3 Formation of Widmanstatten structure [BAD08].

1.3 Principal of orthogonal cutting

In most industrial operations treating the metal shaping by material removal, complex insert geometries with various chip breakage are widely adopted for machining operation. To avoid this complexity in the case of modeling cutting process, two dimensional plane strain assumptions are usually proposed. These elaborated cutting models are known as orthogonal cutting ones. In these conditions, the tool cutting edge is simultaneously orthogonal to the cutting velocity and the feed velocity as it is presented in Fig. 1.4. In a general case, the orthogonal cutting corresponds to a given insert with an edge inclination λ and entering angles κ equal to 0° and 90°, respectively.

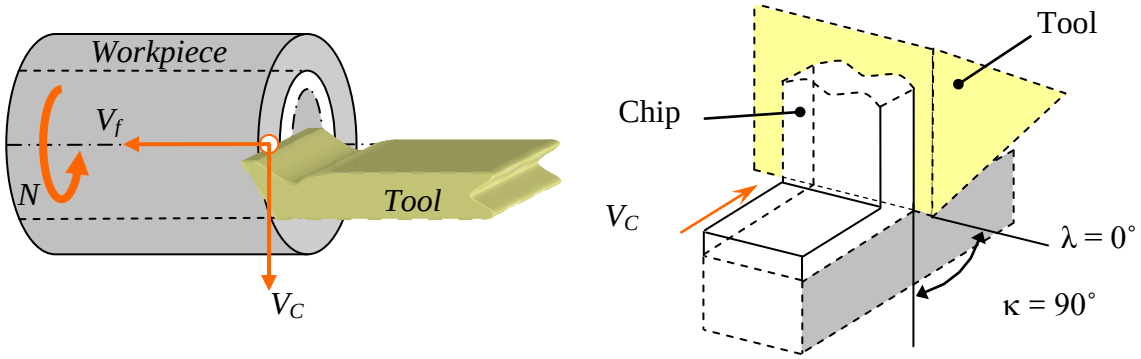

Fig. 1.4 Schematic representation of the orthogonal cutting case

1.4 Chip formation

In many published papers, the great interest on machining study is focused on the chip formation which is obviously a waste. Nevertheless, the aim is to study the conditions accompanying the formation of this chip and what can imply to the interaction between the chip and tool/workpiece. Indeed, the cutting process is accompanied by complex phenomena and its morphology is affected by the whole machining system: the dynamic behaviour of the

machine, the type of lubrication and characteristic of the cutting fluid, the cutting parameters, the tool material grade and its geometry, and the physical and chemical characteristics of the material to be machined.

The experimental studies concerning cutting forces, metallographic chip investigations, surface integrities, etc. allow to investigate some interesting phenomena of mechanical, tribological and surface engineering aspects. However, these phenomena which are localised in the cutting zone (Fig. 1.5) during tool-chip interaction are difficult to capture only through the method of experiments. According to the literature [ASA11a] the chip formation is characterised by five zones:

- Zone 1: Primary shear zone. It is the result of the change of the material flow direction. This zone undergoes sudden deformation by shear. In addition, to high strain rates, a strong rise in temperature by plastic work is also generated.
- Zone 2: Secondary shear zone. It is induced by friction on insert rake face. This zone is simultaneously subjected to high strain rates and strong rise in temperature due to plastic deformation and the dissipation of heat by friction.
- Zone 3. Separation zone of the workpiece. It is characterised by an intense deformation due to tool compression. The latter also provokes elastic and plastic deformations which, by means of "spring back", induce residual stresses on the surface of the machined workpiece.
- Zone 4. In this zone, machined surface is solicited by the insert clearance face which is affected by the wear phenomenon due to friction.
- Zone 5: This is the zone limiting the workpiece deformation during the tool-workpiece interaction.

In each of these zones, different thermo-physical and chemical phenomena like adhesion, welding, diffusion, chemical transformation, etc. can occur. This induces metallurgical structure transformation mainly due to mechanical loadings and rise in temperature.

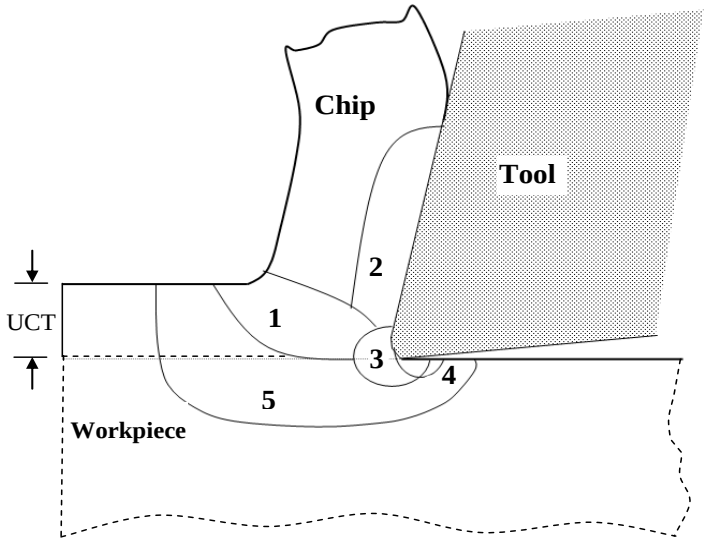

Fig. 1.5 Principal affected zones in chip formation

1.5 Finite element modeling of machining process

1.5.1 Modeling solution strategies

Among the literature published [VAZ07] in the topic of machining modeling based on FE method, it can be underlined that the Lagrangian approach is widely used to model the movement description inside cutting model. This is due to the fact that this approach gives satisfies geometry in terms of chip morphology. Nevertheless, this approach introduces model mesh distortion which can be avoided by adopting Eulerian and Arbitrary Lagrangian - Eulerian (ALE) approaches. The latter can be employed at the cost of non-real chip and calculation time. The three different methods are discussed below.

The Lagrangian formulation assumes that the FE mesh is attached to material and follows its deformation. This provides simpler schemes to simulate transient processes and discontinuous chip formation. However, element distortion has restricted the analysis to incipient chip formation or machining ductile materials using larger rake angles and /or low-friction conditions [LO00, BAR05]. Re-distorted meshes [SHE03, OHB05] or re-meshing [ÖZE00, VAZ01] have been used to minimize the problem.

In Eulerian formulation, the mesh is fixed in space and material flows through the element faces allowing large strains without causing numerical problems. Moreover, this strategy is not affected by element distortion and allows a steady state machining to be simulated. However, Eulerian approach does not permit element separation or chip breakage and requires a proper modeling of the convection terms associated with material properties. In addition,

such formulations also require the prior knowledge of the chip geometry and chip-tool contact length, thereby restricting the application range. In order to overcome this shortcoming, various authors have adopted iterative procedures to adjust the chip geometry and/or chip/tool contact length [KIM99, RAC04].

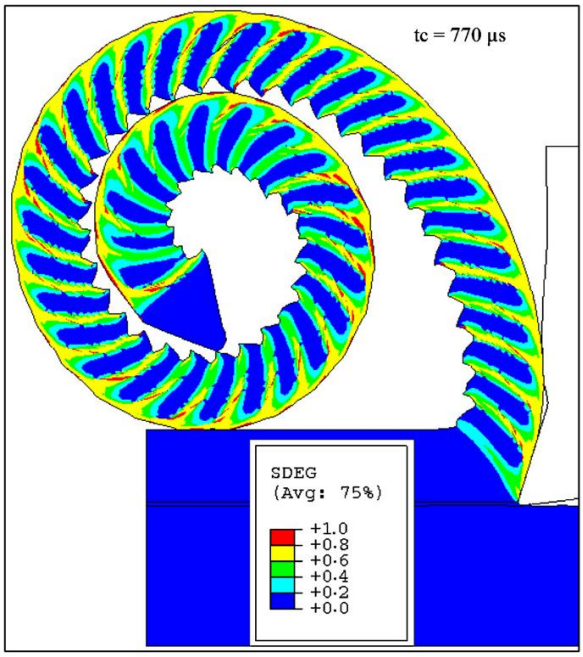

a) Lagrangian formulation [MAB08] here is the damage distribution in the chip

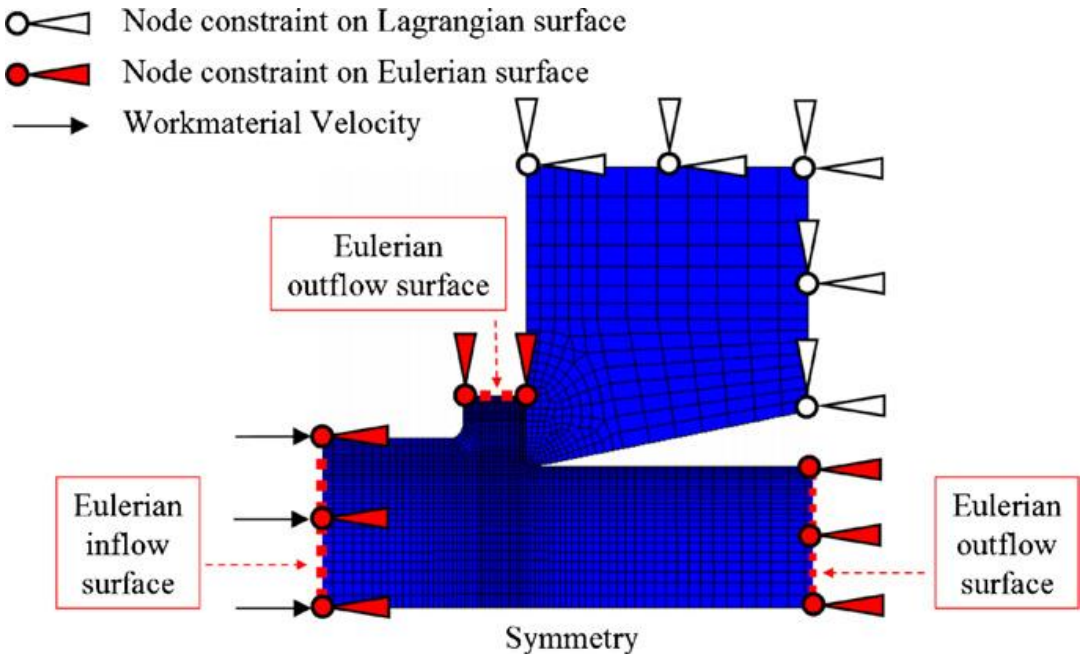

b) Arbitrary Lagrangian - Eulerian formulation [BON08]

Fig. 1.6 Orthogonal chip formation adopted

In an attempt to combine advantages of both Lagrangian and Eulerian formulation, a mixed approach, known as Arbitrary Lagrangian - Eulerian formulation (ALE) has been proposed to model machining operations. This method applies Lagrangian and Eulerian steps sequentially and uses so-called operator split, as illustrated in Fig. 1.7. The first step assumes that the mesh follows the material flow, in which a Lagrangian problem is solved for displacements. Subsequently, the reference system is moved (the mesh is repositioned) and an advection problem (Eulerian step) is solved for velocities. Despite the fact that ALE methods reduce the element distortion problem typical of Lagrangian approaches, a careful numerical treatment of the advection terms is required. More elaborate discussion on the use of ALE formulations in modeling metal machining are presented by ([MOV00], [JBE04], [NAS07], [BON08]), Fig. 1.7.

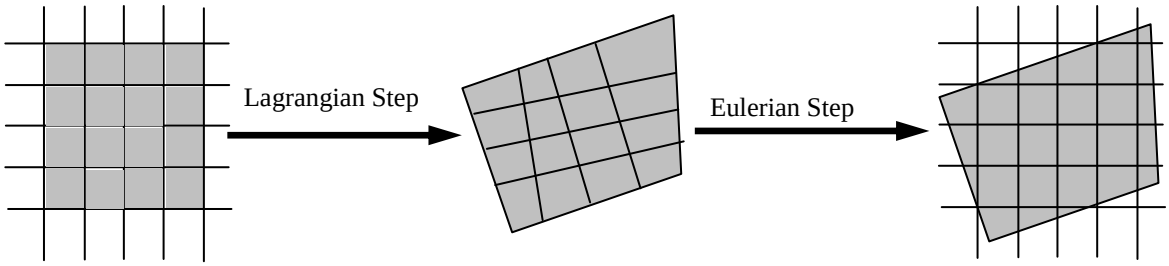

Fig. 1.7 The ALE operator split [JBE04]

Recently, Lagrangian smoothed particle hydrodynamics (SPH)-based model have been employed to manage large material distortions that occur in the cutting problem, and SPH contact control permits a ‘‘natural’’ workpiece/chip separation (Fig. 1.8). [LIM07, CAL09]. The SPH cutting model has been proved to account for continuous to shear localized chip formation and also correctly estimates the cutting forces [LIM07].

SPH is a Meshfree method that is originated in 1977 for astrophysics applications. Over the past three decades, the method is being improving and extending to continuum mechanics scales. During the fifteen more recent years the method has been proved to be stable in a mathematical point of view [LAC98] and stresses and strains tensors can now be computed through behaviour laws ranging from pure fluids to brittle solids. The main advantage of the SPH method is to bypass the requirement for a numerical grid to calculate spatial derivatives. Material properties and state variables are approximated at a discrete set of disordered points,

called SPH particles. This avoids severe problems associated with mesh tangling and distortion which usually occur in Lagrangian analyses involving large deformation and/or strain rates and extreme loading events [LIM07].

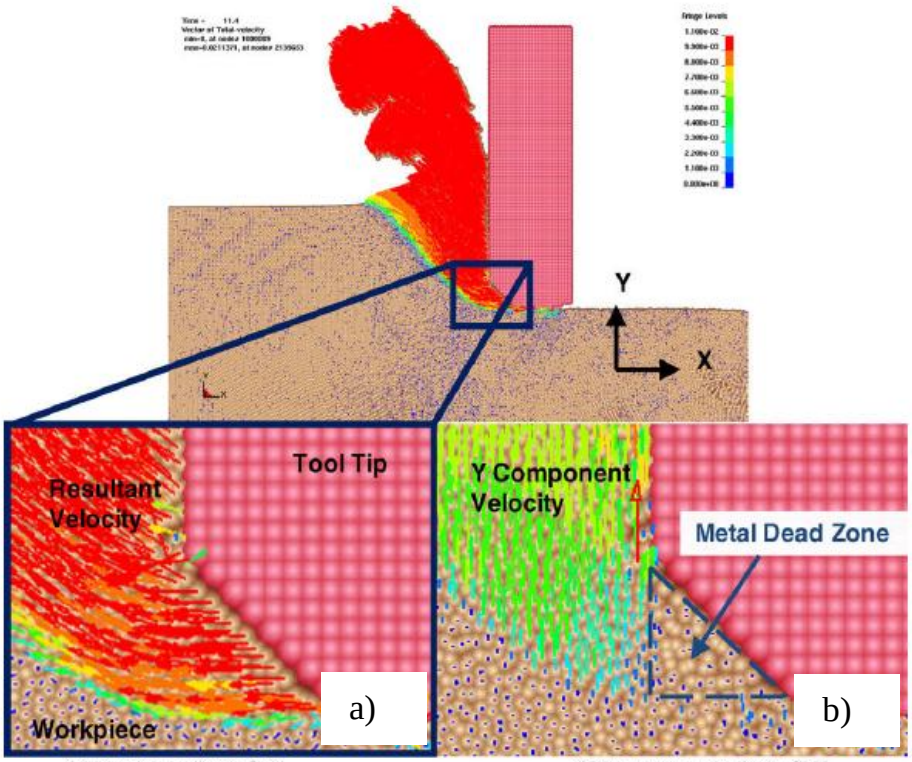

a) Resultant velocity field b) Y component velocity field

Fig. 1.8 Velocity field at tool tip: Metal dead zone identification [CAL09]

1.5.2 Constitutive material models and chip separation techniques

The flow stress characteristics of the material greatly influence the FE cutting simulation for different cutting regimes. The material constitutive model is usually required to relate the flow stress to strain, strain rate and temperature.

Various numerical studies have been performed using a wide of constitutive models for the concerned workpiece, such as rigid plastic [CER99], rigid - viscoplastic [KOU02], elasto - viscoplastic [UMB04]. Elastic to plastic materials have been the most commonly used in simulations, with the plastic strain rate dependency being included in some studies [LIN92, YAN02]. One of the most popular material formulation (elasto- thermo-visco-plastic) adopted in the present study is that proposed by Johnson and Cook (J-C) [JOH85a]. Several modeling studies have shown the effectiveness of this material flow stress model [JIN04, GUO04].

Later, Calamaz et al. [CAL09] developed a new material constitutive law, which takes into account the influence of strain, strain rate and temperature on the flow stress and also introduces a strain softening effect. Similar to Calamaz et al., Sima and Ozel [SIM10] also improved the J-C model by considering the temperature-depend flow softening, in which the flow softening phenomenon, strain hardening and thermal softening effects and their interactions are coupled.

The critical algorithms which can be evoked during FE based simulation (For the Lagrangian formulations) of the cutting process are specified as the technique of chip separation criteria which can be classified in the following three aspects:

- Node separation technique (named also debonding method): is a geometry - based approach [HAS99, GUO00]. A predefined parting line is used to separate the chip layer from the workpiece. At each point on the parting line, two nodes are tied together initially and chare the same degree of freedom. When the tool approached the tied pair of nodes, they separate based on a pre-specified criterion is met. Other commonly used criterion is the tool node distance, critical effective stress, and critical effective plastic strain.
- Element deletion technique [RAM02]: is also a geometry based approach in which the chip layer is predefined by a sacrificial element zone positioned at the bottom of the chip. When the tool approaches a sacrificial element, the later will be deleted based on a given criterion such as critical effective plastic strain or critical energy density.
- Mechanical fracture approach: According to certain publication [SCH00] the using of later criterion to determine chip separation is controversial since there is no consensus in the literature on whether chip formation indeed occurs by fracture or not. However, this technique is being used by many researchers and promising results are obtained [MAB08]. Lately, Subbiah and Melkote [SUB08] have shown that fracture occurs in the tool edge vicinity through the experimental study for machining of the aluminium alloy Al2024.

1.5.3 Heat generation and thermal assumption

Another important feature of the cutting simulation is the consideration of the heat generation due to the simultaneous phenomena of inelastic deformation and friction. This in turn changes the material properties. Therefore, it's necessary to capture the stress, strain and temperature

simultaneously with the thermo-mechanical modeling when the material is being removed. So, the coupled temperature - displacement analysis has to be performed.

Nevertheless, some studies have generated physical results with adiabatic hypothesis [MAB06, WEN06]. The solution of the temperature field equation for the heat conduction is not required when this assumption is made, but this approximation can only be safely adopted for low diffusivity materials in high-speed processes. The temperature increase is calculated directly at the material integration points according to the adiabatic thermal balance. If the cooling at room temperature is needed in order to evaluate residual stresses inside the workpiece, it is not advisable to adopt this simplification [VAZ07]. If such numerical model assumes that the working condition imply adiabatic assumption (for example at a given cutting speed), this is probably not true. Indeed, a calculation based on the criterion developed by Recht [REC64] or that given by Frost and Ashby [FRO82] should to be checked to see whether conditions are in fact adiabatic or not.

Certainly, for specific cutting parameters both inelastic heating and conduction of the heat are important. So, a coupled temperature - displacement analysis must be included as it is adopted in the present work. The heat transfer modeling formulation adopted in the present study is detailed in the following chapter.

1.5.4 Tool/chip interface friction models

Friction between chip and tool constitutes one of the most important and complex aspects of machining process. It potentially can determine, not only the tool wear and the quality of the machined surface, but also the structural loads and the needed power to remove a certain volume of metal.

The temperature independent, stick -slip friction model which has been developed by Zorev's [ZOR63] is one of the most commonly used approximations to frictional contact between chip and tool. Zorev advocated the existence of two distinct chip/tool contact regions: near the tool tip, shear stresses τ_f are assumed to be equal to shear strength of the material being machined, τ_Y, whereas, in the sliding region, the frictional stress is proportional to the normal stress, σ_n

$$\tau_f = \begin{cases} \tau_Y, & 0 \le \ell \le \ell_C \ (\mu\sigma_n \ge \tau_Y) \rightarrow stick \\ \mu\sigma_n, & \ell > \ell_C \ (\mu\sigma_n < \tau_Y) \quad \rightarrow slide \end{cases} \tag{1.1}$$

in which μ is commonly associated with Coulomb's friction coefficient an l_c is a part of the contact length characterising a transitional contact zone, assumed to be known in advance in

most cases (see Fig. 1.9). Similar approaches have been applied to simulate machining processes. For example, defining an average friction coefficient over the rake face, separate coefficients for each region, different length for the sticking region, or even neglecting altogether the low stress variation of shear and normal stresses and simply assuming $\tau_f = m\tau_Y$ (m<1) along the rake face [JIA04, GUO06].

Other researchers [SHI74, USU82, OBI96, OBI97] have attempted to use more realistic friction models. In this context, experimental models were introduced by Usui and co-workers [USU82] in order to feed a non-linear friction model relating normal stress to frictional one as

$$\tau_f = \tau_Y \left[1 - \exp(-\frac{\mu\sigma_n}{\tau_Y}) \right] \tag{1.2}$$

Where μ is a tool/chip material constant and τ_Y is the maximum shear stress of the chip surface layer in contact with the rake face of the tool. Eq. 1.2 approaches $\tau_f = \tau_Y$ for large normal stresses (sticking region) and the classical Coulomb's law, $\tau_f = \mu\sigma_Y$, for smaller values of σ_n (sliding zone), as illustrated by the dashed line in Fig. 1.9.

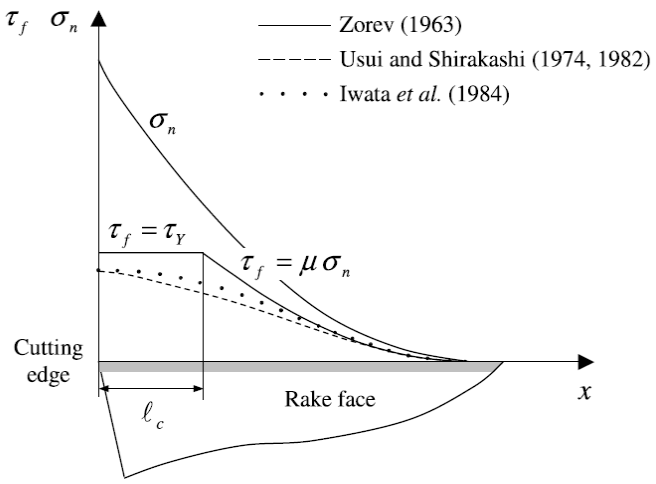

Fig. 1.9 Frictional and normal stresses along the rake face

Childs and co-workers [DIR01, OBI00] introduced further modifications in Eq. 1.3 so that

$$\tau_f = m\tau_Y \left[1 - \exp(-\frac{\mu\sigma_n}{m\tau_Y})^n \right]^{1/n} \tag{1.3}$$

In which *n* controls the transition from the sticking to the sliding region and *m* accounts for a lubrication effect.

Özel [ÖZE06], by comparing experimental results with several friction models based on Eqs. 1.1 to 1.3 concluded that predictions are more accurate when utilising friction models based on the measured normal and frictional stresses on the tool rake face and when implemented as variable friction models at tool-chip contact in the FE simulations.

Based on the experiment where a bar-shaped tool slides over the inner surface of a ring specimen, Iwata et al. [IWA84] proposed an expression for frictional stress dependence on Coulomb's friction coefficient, normal stress and Vickers hardness of the workpiece material, H_v, as:

$$\tau_f = \frac{H_V}{0.07}\tanh\left(\frac{\mu\sigma_n}{H_V/0.07}\right) \rightarrow \tau_f = m\tau_f \tanh\left(\frac{\mu\sigma_n}{m\tau_Y}\right) \quad (1.4)$$

Which was later approximated using the shear stress flow stress to guarantee that $\tau_f < \tau_Y$ in the element immediately in contact with the rake face. Noticeably, Eq. 1.4 yields a close approximation of Usui's friction model when $H_V/0.07\tau_f \rightarrow m\tau_Y$, as illustrated by the dotted line depicted in Fig. 1.9.

Finally, frictionless contact has also been assumed by several authors [BAK03, BAK05, BAK06]. Despite the importance of friction in machining simulation, most authors agree that the existing models present limitations and further experimental-numerical efforts are still required to describe interaction between tool and workpiece.

1.5.5 Micro-scale effect and material microstructure

Worthy scientific researches have been made recently for the physical comprehension of the size effect phenomenon in the domain of micro cutting processes [BAC52, LAR73, DIN01]. The term size effect in machining is usually attributed to define the nonlinear increase in specific cutting energy when uncut chip thickness (UCT) reaches few microns. Numerous experimental and numerical studies have been dedicated to explain this scaling phenomenon. The investigations have shown that there are multiple factors that can increase material strength and contribute to the size effect in micro machining operations. From the material point of view, Backer et al. [BAC52] have accounted the increase of the SCE in orthogonal turning tests performed on SAE 1112 steel to the size effect.

While Larsen-Base and Oxley [LAR73] highlighted the importance of the increase in strain rate in primary shear zone with a decrease in uncut chip thickness, as the primary cause in the increasing material strength. Dinesh et al. [DIN01] explained the increase in hardness of metallic materials with the decrease in deformation depth, which is as the consequence of the strong dependence of flow stress on strain gradient in the deformation zone. Based on their work, Joshi and Melkote [JOS04] has presented an analytical model for orthogonal cutting incorporating strain gradient (SG) effect in material constitutive law. They have shown that the length of primary deformation zone represents the fundamental length scale governing the size effect.

Recently, Asad et al. [ASA11] have made a systematic study about the influence of SG during macro to micro-scale milling, they incorporated the SG effect into traditional JC constitutive law by implementing a user routine VUMAT. Their research results show that the specific cutting energy values obtained by numerical simulations using strain gradient based plasticity model were quite close to the experimental ones, as shown in Fig. 1.10.

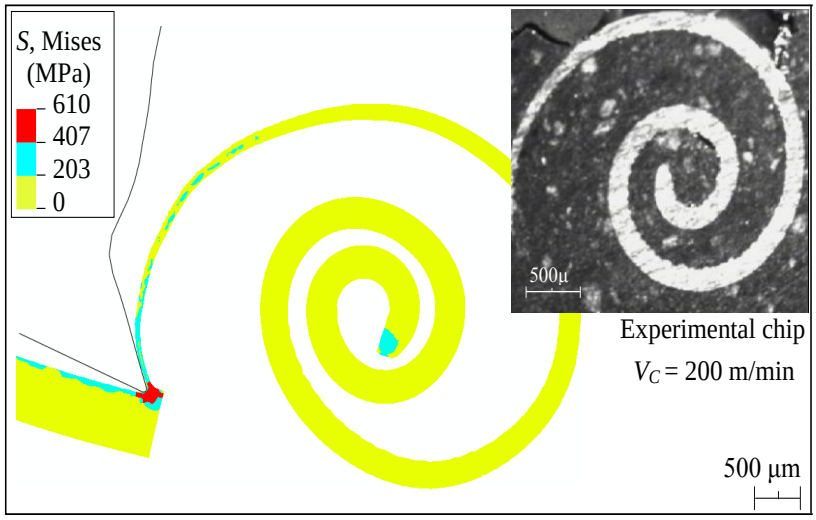

a)

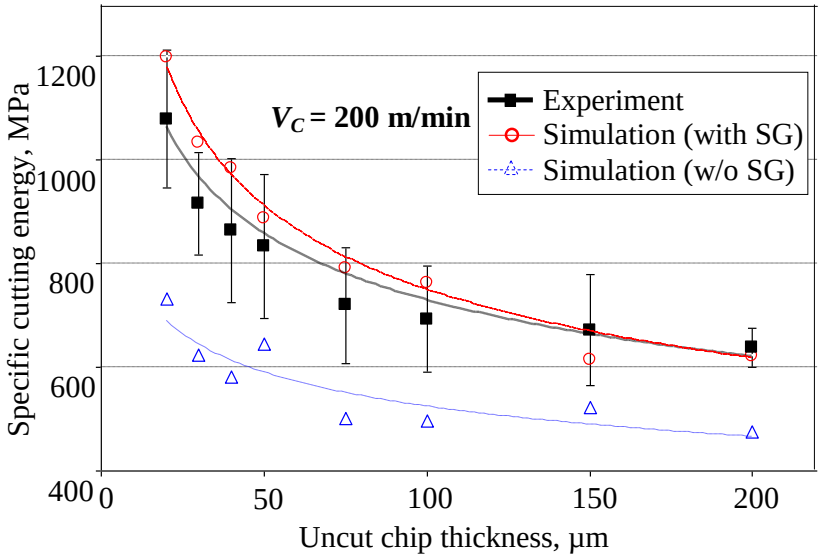

b)

Fig. 1.10 SG effect [ASA11]: a) Chip formation, b) specific cutting energy evolution

At the same time, researchers start to model the cutting process by considering the material microstructure. Chuzhoy [CHU02, CHU03A, CHU03B] developed the MML model of ductile iron machining and its constituents, and the validation is carried out through the experimental machining. Obikawa [OBI09] studied the microscopic phase-dependent residual stresses in the machined surface layer of two-phase alloy - iron and steel, and found that the microstructure of the workpiece has a great influence on the residual stress distribution. Simoneau et al. [SIM06a, SIM06b] defined microscale cutting as the point at which the uncut chip thickness was smaller than the average size of the smallest grain type in the UCT (Fig. 1.11).

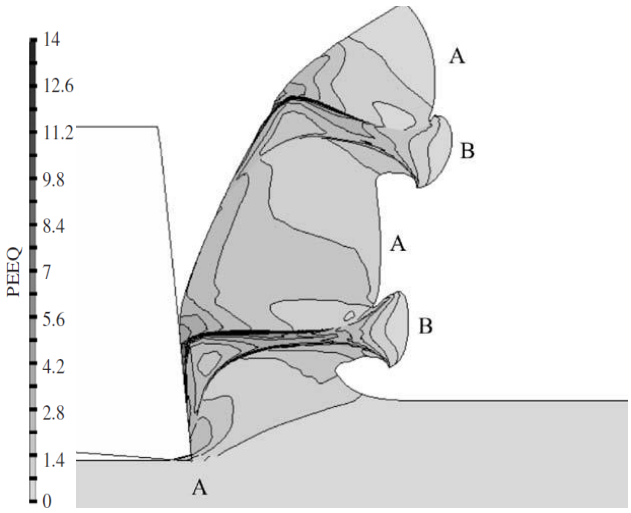

a)

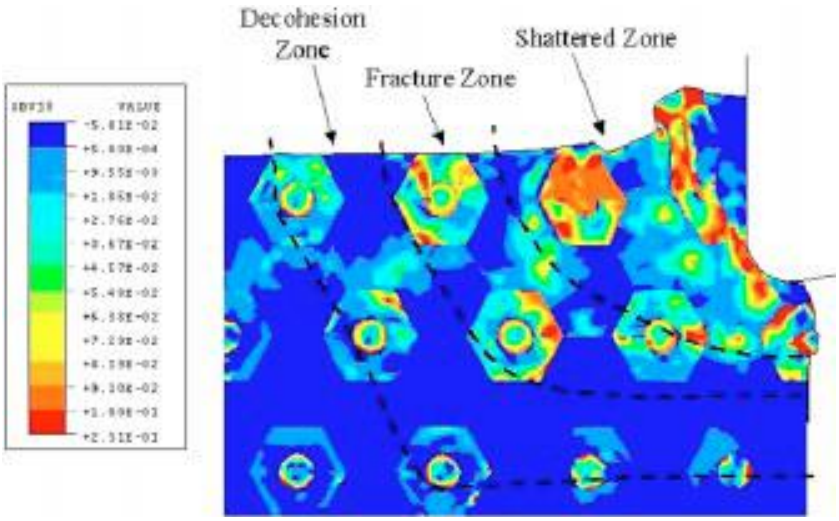

b)

Fig. 1.11 Cutting model considering material microstructure: a) Equivalent plastic strain [SIM06a, SIM06b], b) Material damage accumulation [CHU02]

1.6 Conclusions

Up to now, various numerical models have been proposed by researchers to get more physical comprehension of chip formation process, with the ultimate aim of improving the cutting process in term of working parameters optimisation. It's well considered that FE method is one of the most common numerical modeling techniques being used for this purpose. Thanks to the advance of high speed computers, robust large-strain/large displacement procedures, contact/fracture algorithms for inelastic problems and robust finite/discrete algorithms etc., cutting simulations have shown the cost effective reliable results.

However, another change is that how to exactly model the multi-physical phenomena: large elasto-plastic deformation, complicated contact/friction conditions, coupled thermo-mechanical effect, chip separation mechanisms, material microstructure influence, etc. On the contrary, once the robust numerical model is established, it will be a useful tool to the optimization of working parameters, tool design and wear etc. Consequently, a subsequent reduction in extensive and costly cutting experimentation can be achieved.

To improve the comprehension of multi-physics of chip formation process, the present study proposes a FE cutting model for Ti–6Al–4V from macro scale to material microstructure-level. For the macro model, the idea is to exploit a phenomenological material behaviour with an isotropic damage to simulate the cutting operation in orthogonal cutting. In this framework, some aspects concerning the limiting shear stress are improved with coupled temperature by contact mechanics theory.

For the material microstructure-level, the theory of the crystal plasticity is for describing the material dislocation effect, two kinds of damage models of intra-grain and inter-grain are also considered to model the failure process of the material. The improved parts are implemented with user subroutines in the modulus of ABAQUS/EXPLICIT. More detailed information of the model is presented in the following chapters.

2 Methodologies on orthogonal cutting modeling of Ti–6Al–4V

2.1 Introduction

After presenting the non-exhaustive literature review that can help the reader to get a global idea on FE modeling of machining operations, the present chapter proposes our methodology to build a FE model for dry machining of the Titanium alloy Ti–6Al–4V in case of orthogonal cutting. For this introductory section, a brief review of chip formation for this cut material grade is proposed.

Indeed, it is known that the Titanium alloy Ti–6Al–4V is widely used in industry [LUT03], and poses a serious challenge, due to its tendency to work harden during the machining process, high cutting temperatures, high cutting pressures, chatter, and its chemical reactivity with tool materials over 500°C [EZU97].

In order to increase productivity and tool-life in machining of Titanium alloys, it is necessary to study the mechanics of chip segmentation and the effects of the working parameter variation on material cutting performance. For that, it is more judicious to build a reliable FE-model allowing more physical comprehension in relationship with this type of material cutting. Nevertheless, the robustness of a given numerical model is strongly dependent on the material constitutive model, material fracture criterion, the work material contact nature at cutting tool-chip interface, and both tool and workpiece material thermal parameters [BON08, UMB08].

At high cutting speeds, it is known that many materials give rise to segmented chips. Nevertheless, the Titanium alloy Ti–6Al–4V is one of the materials often generating

characteristic segmented chips at very low cutting speeds, as it is mentioned by Komanduri and Hou [KOM02]. These authors predicted the critical cutting speed value corresponding to the onset of shear localization of Ti–6Al–4V to be approximately equals to 9 m/min whereas this value is, for example, near 130 m/min when cutting AISI4340 steel.

Two theories about saw-tool chip formation predominate, namely (I) the thermoplastic instability and (II) the initiation and propagation of cracks inside the primary shear zone of the workpiece material. Shaw et al. [SHA54] and Komanduri and Turkovitch [KOM81] explained that the Titanium alloy chip morphology is due to a plastic instability during the cutting process resulting from the competition between the thermal softening and the work hardening in the primary shear zone. Vyas and Shaw [VYA99] and Jiang and Shivpuri [JIA04] explained the Titanium alloy chip segmentation by a crack initiation followed by propagation inside the primary shear zone.

Owen and Vaz [OWE99] talked about a failure softening phenomenon which induces a decrease in stress with increasing strain. Generally, the failure of a material is consequence of accumulation of dislocations and subsequent microscopic damage. Vaz and Owen [VAZ01] also addressed ductile fracture by means of continuum damage mechanics, from which two new failure criteria based on coupled and uncoupled damage analysis are derived. Additional considerations on stress update algorithms and adaptive re-meshing for damaged materials are also presented. According to Giovanola [GIO88], the material failure in adiabatic shear bands happens in two separate phases. Initially a thermal softening appears followed by a nucleation and growth of micro-cavities. Saanouni et al. [SAA09] developed the fully coupled thermo - elasto - visco - plastic - damage constitutive equations based on the state variables under large plastic deformation for metal forming simulation. The model is implemented into Abaqus/Explicit using the Vumat user subroutine and used in connection with a 2D adaptive mesh facility.

As considering large strains, high strain rates and temperature dependent visco - plasticity, Johnson Cook (J-C) material constitutive model is widely used in FE cutting models. While the J-C law exhibits a flow stress which increases with increasing strain whatever the temperature, some authors [GUO06] affirmed that the J-C model can not predict the adiabatic phenomenon responsible for the saw-tooth chip formation. They explain that is due to the absence of strain softening consideration.

In order to achieve the adiabatic phenomenon, Calamaz et al. [CAL08] developed a new material constitutive law, which takes into account the influence of strain, strain rate and

temperature on the flow stress. Also, they have introduced a strain softening effect on equivalent stress evolution. Similar to Calamaz et al., Sima and Ozel et al. [SIM10] also improved the J-C model by considering the temperature-depend flow softening. (The flow softening phenomenon, strain hardening and thermal softening effects and their interactions are coupled). Other approaches are based on ductile failure model of J-C to achieve the degradation of material and get segmented chip morphology [MAB08].

Another parameter investigated in numerical simulations is the influence of the friction conditions at tool-chip interface. In most studies, the Coulomb friction model is commonly used [LI02, MAB06]. Guo et al. [GUO06] and Guo and Liu [GUO02] used a Coulomb friction law and Tresca stress limit to model the sticking and sliding conditions at the tool - chip interface. Since friction is not precisely known, some authors [BÄK05, BÄK06] neglected it in their numerical simulations. Childs [CHI06] studied the effect of both the Coulomb and Tresca friction laws in the case of continuous chip simulations and proposed a new model in which the friction coefficient depends on the plastic strain rate. An important analysis about the influence of the friction models on machining numerical simulation has been carried out by Özel [ÖZE06] through comparing experimental results with four group friction models, he concludes that predictions are more accurate when utilising friction models based on the measured normal and frictional stresses on the tool rake face and when implemented as variable friction models at tool-chip contact in the FE simulations.

In this chapter, the main objective deals with the presentation of a FE based numerical model for orthogonal cutting built with ABAQUS/EXPLICIT. Material fracture energy was put forward to reduce the mesh dependency and achieve material degradation during cutting process. Moreover, the mesh sensitivity was also analyzed in order to obtain the appropriate mesh size for all adopted simulations. In the present study, the limiting shear stress approach in the friction model was refined with the maximum shear stress at the tool-chip contact surface.

In the following, a brief introduction of ABAQUS software and its explicit dynamic approach, geometry model, material constitutive model, mesh optimization, and improved tool-workpiece friction contact model concerning orthogonal cutting are discussed.

2.2 ABAQUS® software and its explicit dynamic approach

Based on a great amount of published papers dealing with the machining simulation, the FE method seems to be somehow advanced and it provides a pertinent understanding of chip

formation mechanism, heat generation in the cutting zone tool-chip friction characteristic, and the integrity of machined surfaces.

Recently, there are many commercial FE codes that are capable of modeling the machining process (DEFORM 2D/3D, ABAQUS, ANSYS, LS -DYNA and Third Wave's Advantage, etc). The present contribution exploits the explicit capabilities of ABAQUS to simulate orthogonal cutting case of Ti-6Al-4V. This software seems to be practical with its graphic user interface (GUI) and is flexible to define user-defined subroutines. Simultaneously, it is possible to simulate diversified problems like stress/displacement, heat transfer, mass diffusion, coupled analysis, acoustics, soil mechanics, and piezoelectric analysis.

ABAQUS consists of two main analysis products: ABAQUS/STANDARD and ABAQUS/EXPLICIT. The first product solves a wide range of linear and nonlinear problems in the domain of elastic, dynamic, and thermal response of the component. The second one is suitable for modeling transient dynamic events, such as impact and blast problems, and is very efficient for highly nonlinear problems involving changing contact conditions, such as forming and machining simulation etc.

ABAQUS provides an interactive graphical environment (ABAQUS/CAE) to create 2D/3D models of the structures to be analysed. It allows defining material properties, boundary conditions, contact model and finally the mesh rules. The file generate in this environment is the "input file" which can be modified for specific purposes. The input file is then submitted to ABAQUS/EXPLICIT solver generating an "output file", containing the required results. Finally, these results could be viewed (graphically and numerically) in the postprocessor ABAQUS/Viewer. This whole procedure can be represented in a block form, as shown in Fig. 2.1.

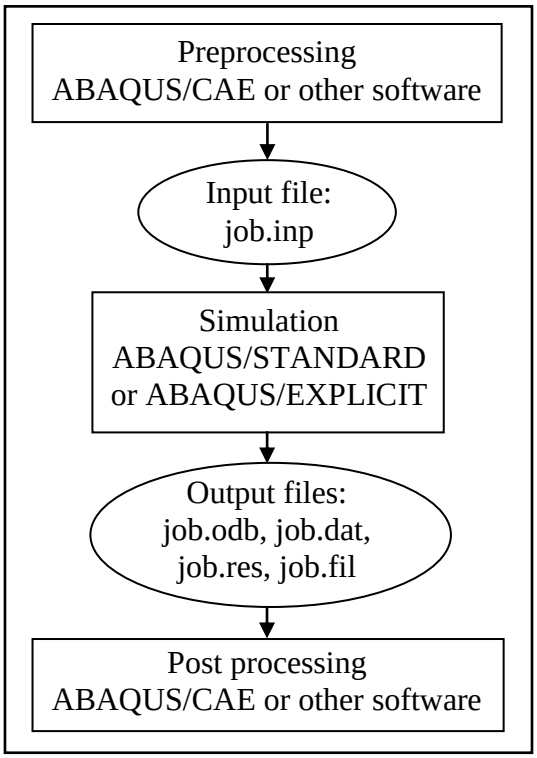

Fig. 2.1 ABAQUS® calculation methodology [ABA10]

The explicit dynamic methods usually concern the high-speed dynamic events, in which the time is discretized into a very small number of increments.

The explicit procedure was based on the implementation of an explicit integration rule along with the use of diagonal element mass matrices. The equation of motion for the body was integrated using an explicit central difference integration rule:

$$\left.\begin{aligned}\mathbf{u}^{(i+1)} &= \mathbf{u}^{(i)} + \Delta t^{(i+1)}\dot{\mathbf{u}}^{(i+1)} \\ \dot{\mathbf{u}}^{(i+1/2)} &= \dot{\mathbf{u}}^{(i-1/2)} + \frac{1}{2}\left(\Delta t^{(i+1)} + \Delta t^{(i)}\right)\ddot{\mathbf{u}}^{(i)}\end{aligned}\right\} \tag{2.1}$$

where $\dot{\mathbf{u}}$ is the velocity, $\ddot{\mathbf{u}}$ the acceleration, and i and i - 1/2, i + 1/2 refer to the increment number and middle-increment number. The acceleration corresponding to an increment, i, is given by:

$$\ddot{\mathbf{u}}^{(i)} = \mathbf{M}^{-1}.\left(\mathbf{F}^{i} - \mathbf{I}^{i}\right) \tag{2.2}$$

where **M** is the mass "Lumped" matrix, F the external applied load vector and I the internal force vector.

As mentioned above, the explicit integration operator is conditionally stable. So, the time increments must satisfy:

$$\Delta t \leq \frac{2}{\omega_{max}} \tag{2.3}$$

where $\omega_{\max}$ is the maximum natural frequency of the system based on a complex set of interacting factors. A conservative estimate of the stable time increment is given by the minimum value for all elements. The above stability limit can be written as:

$$\Delta t = min\left(\frac{L_e}{c_d}\right) \tag{2.4}$$

where L_e is the mesh characteristic element dimension and C_d the current effective, dilatational wave speed in the worked material defined by Eq. 2.5.

$$C_d = \sqrt{\frac{\lambda + \mu}{\rho}} \tag{2.5}$$

where ρ is the material density. λ and μ are Lamé's constants defined in terms of Young's modulus E, and Poisson's ratio ν.

In ABAQUS/EXPLICIT, modal mass, material and mesh size influence time increment. Artificial mass scaling can be assumed for small or poorly shaped elements, which are usually small in numbers. By increasing the mass of these elements, stability limit can be increased significantly, while the overall physics of the system remains the same.

The explicit dynamic procedure performs a large number of small time increments efficiently. The use of small increments (dictated by the stability limit) is advantageous because it allows the solution to proceed without iterations and without requiring tangent stiffness matrices to be formed. It also simplifies the treatment of contact.

2.3 Numerical approach

2.3.1 Modeling data and geometrical model

The commercial software Abaqus 6.8-2 with its explicit approach was employed to improve physical comprehension of segmented chip formation, and to highlight the effect of friction properties during Titanium alloy Ti–6Al–4V cutting. A 2D orthogonal cutting model was developed as shown in Fig. 2.2. Linear quadrilateral continuum plane strain element CPE4RT

with reduced integration was utilized for a coupled temperature–displacement analysis, and enhanced hourglass control was selected in this study for the entire set of elements.

Machining parameters were taken similar to those adopted by Jiang and Shivpuri [JIA04] and Umbrello [UMB08]. For the workpiece, the UCT was equal to 0.127 mm with a cutting depth a_p = 2.54 mm. The WC ISO-P20 cutting tool considered was with normal rake and flank angles of 15 deg. and 6 deg., respectively. The tool entering and inclination edge angles were 90 deg. and 0 deg., respectively. The tool-cutting edge radius was of 30 μm. The tool-workpiece interaction was considered under dry machining conditions.

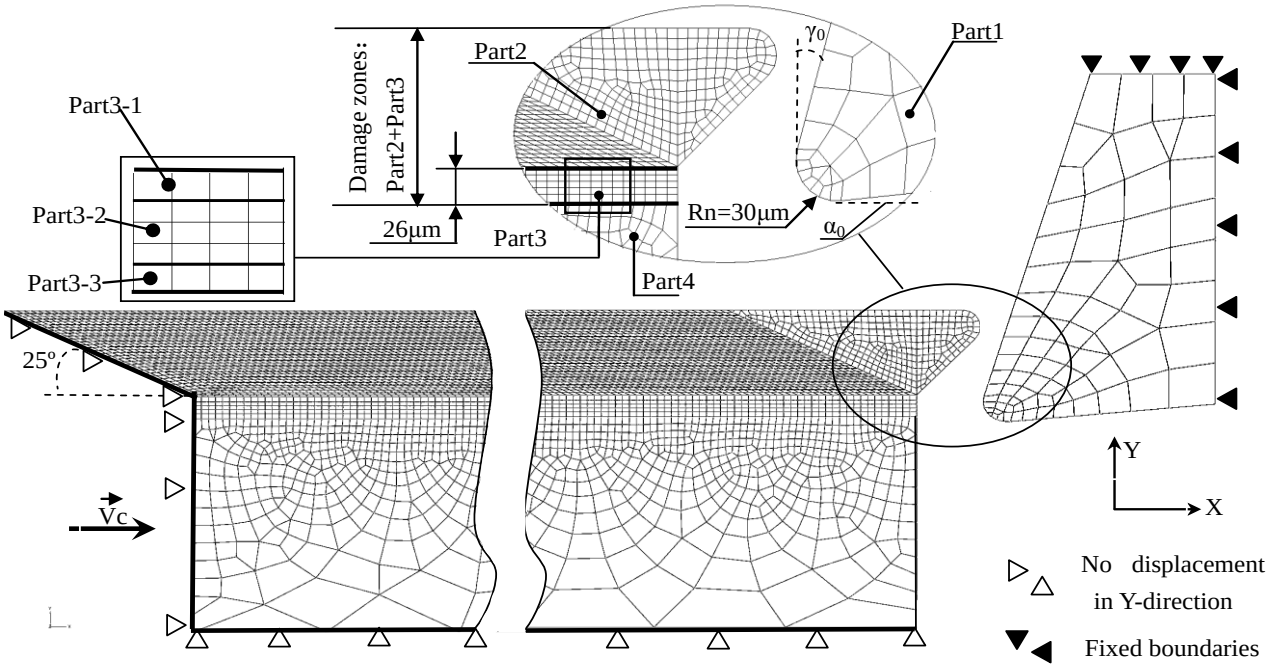

Fig. 2.2 Model mesh and boundary conditions

To optimize the contact management during simulation, a multi-part model (Fig. 2.2) was typically developed with four geometrical parts: (1) Part1 - the insert active part, (2) Part2 - the uncut chip thickness, (3) Part3 - the tool-tip passage zone, and (4) Part4 - the workpiece support.

It should be noticed that the thickness of tool-tip passage zone (Part3), which is the sacrificial layer, was usually recommended larger than that of the cutting edge radius [SUB08] to avoid mesh distortion problem. In the proposed model, the critical layer size above which the element can climb up rake face without mesh distortion was found equal to 0.026 mm. The sacrificial zone was meshed with five elements to study the contact effect around the cutting

edge. Also, the passage zone (Part3) was divided into three small parts: Part3-1, Part3-2, and Part3-3. It should be also mentioned that the elements in the damage zone will be removed when they are completely damaged, while the parts which are not completed damaged will become part of the chip during its formation. Moreover, the vertical mesh size in the damageable zone was kept as a constant value and always meshed with elements in the following simulation test.

For boundary conditions used in the present model, the cutting tool was assumed to be fixed on its top and right sides, and the workpiece was allowed to move horizontally from the left to the right while restrained vertically.

2.3.2 Material behaviour and chip formation criterion

2.3.2.1 Material constitutive model

The material constitutive model of Ti–6Al–4V follows the J-C model [JOH85a]. It provides a satisfactory description of the behaviour of metals and alloys since it considers large strains, high strain rates and temperature dependent visco-plasticity. This model is defined by the following expression of the equivalent stress.

$$\bar{\sigma}_{JC} = \left[A + B \times \left(\bar{\varepsilon}^{p} \right)^{n} \right] \times \left[1 + C \times ln\left(\dot{\bar{\varepsilon}}^{p} / \dot{\bar{\varepsilon}}_{0}^{p} \right) \right] \times \left[1 - \left(\frac{\theta_w - \theta_0}{\theta_m - \theta_0} \right)^{m} \right] \tag{2.6}$$

The J-C material parameters of the workpiece adopted for Ti–6Al–4V can be found in Table 2.1, whereas the physical parameters of both the workpiece and the tool-insert are given in Table 2.2.

Workpiece	*A (MPa)*	*B (MPa)*	*n*	*C*	*m*	D_1	D_2	D_3	D_4	D_5
Ti-6Al-4V	1098	1092	0.93	0.014	1.1	-0.09	0.25	-0.5	0.014	3.87

Table 2.1 Johnson-Cook Material Model [LES00]

Parameters			
Materials	Properties	Workpiece (Ti–6Al–4V)	Tool (P20)
	Density, ρ (kg/m^3)	4430	15700
	Elastic modulus, E (GPa)	110	705
	Poisson's ratio, ν	0.33	0.23
	Specific heat, C_p (J/kg°C)	670	178
	Thermal conductivity, λ (W/m°C)	6.6	24.0
	Expansion coef., α_d (μm/m/°C)	9	5
	Tmelt (°C)	1630	×
	Troom (°C)	25	25
	Inelastic heat fraction (β)	0.9	
Contact	Heat transfer coefficient (W/m^2 K)	4 x 10^4	
	Heat partition coefficient	0.5	
	Friction coefficient	0.7	
	Friction energy transferred into heat	100 %	

Table 2.2 Physical parameters of workpiece and cutting tool [MAT08]

2.3.2.2 Chip formation criterion

In order to simulate chip formation, a failure damage model has been exploited. This model can be illustrated via a typical uniaxial stress–strain in the case of a ductile metal, see Fig. 2.3. Indeed, the response of the latter is initially linear elastic (O–A) followed by plastic yielding with strain hardening (A–B), wherein the curve ABC is the undamaged stress-strain response. The effect of the damage on the behaviour becomes sensitive at point B, leading to a progressive decrease in the tangent modulus (or hardening modulus). The point D corresponding to the maximum stress is given by the fact that the hardening modulus reaches zero value for a significant value of the ductile damage ($0.3< D <0.7$ depending on the material type). The point E corresponds to the observed fracture while the point F indicates the theoretical final fracture. Clearly the Young's modulus progressive decrease starts just after the point B as indicated in the figure given below. The deformation during B-F is localized in a neck region of the specimen. Point B identifies the material state at the onset of damage, which is referred to as the damage initiation criterion. Beyond this point, the stress strain response (B-F) is governed by the evolution of stiffness degradation in the region of strain localization. The chip formation, by ductile failure phenomenon, occurs in two steps. The first step concerns the damage initiation whereas the second one concerns damage evolution based on the fracture energy approach.

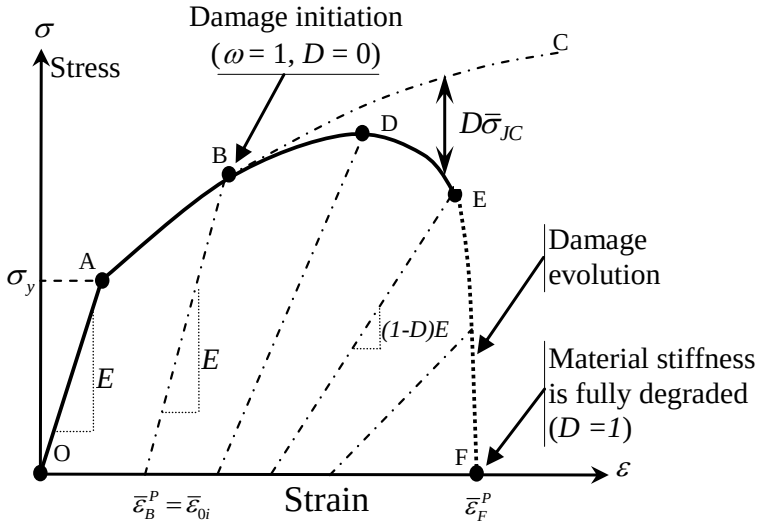

Fig. 2.3 Typical uniaxial stress-strain response of a metal specimen

Damage initiation

The J-C shear failure model was used as a damage initiation criterion. It contains five failure parameters, which must be specified (D_1...D_5). The parameter values of Ti–6Al–4V are given in Table 1 [LES00].

$$\bar{\varepsilon}_{0i} = \left[D_1 + D_2 \exp(D_3 \frac{P}{\bar{\sigma}_{JC}}) \right] \times \left[1 + D_4 \operatorname{Ln}\left(\frac{\dot{\bar{\varepsilon}}}{\dot{\bar{\varepsilon}}_0} \right) \right] \left[1 + D_5 \left(\frac{\theta_w - \theta_0}{\theta_m - \theta_0} \right) \right] \tag{2.7}$$

The damage in a given finite element is initiated when a scalar damage parameter ω exceeds 1. This parameter is based on a cumulative law defined as:

$$\omega = \sum_{i=1}^{n} \left(\frac{\Delta \bar{\varepsilon}^{p}}{\bar{\varepsilon}_{0i}} \right)_i \tag{2.8}$$

Where $\Delta \bar{\varepsilon}^{p}$ is the increment of equivalent plastic strain during an increment of loading, *i*, for each integration point.

Damage evolution

The Hillerborg's fracture energy [HIL76] was introduced to model damage evolution. There are mainly two reasons for introducing the Hillerborg's fracture energy:

- To control the material degradation after the damage initiates, this makes the failure process more stable.
- To capture high strain localization during chip segmentation even for relatively large size element.

When material damage occurs, the stress-strain relationship does no-longer accurately represent the material's behaviour. Continuing to use the stress-strain relation introduces a strong mesh dependency based on strain location, such that the energy dissipated as the mesh is refined. The mesh size in the Calamaz's [CAL08] model is around 2 μm near the cutting edge and along the primary shear zone. The Hillerborg's fracture energy, G_f, is adopted to reduce the mesh dependency by creating a stress-displacement response after damage initiation.

$$G_f = \int_{\bar{\varepsilon}_B^p}^{\bar{\varepsilon}_F^p} L\bar{\sigma} d\bar{\varepsilon}^p = \int_0^{\bar{u}_F^p} \bar{\sigma} d\bar{u}^p \tag{2.9}$$

Where, the characteristic length L is the square root of the integration point element area based on a plane strain element CPE4RT. And $\bar{\varepsilon}_B^p$ and $\bar{\varepsilon}_F^p$ are the equivalent plastic strain at point B and F correspondingly to Fig. 2.3, and $\bar{u}^p$ and $\bar{\sigma}$ are the equivalent plastic displacement and stress.

The scalar stiffness degradation for the linear damage process used for part 3 (sacrificial zone) is given by:

$$D = \frac{\int_{\bar{\varepsilon}_B^p}^{\bar{\varepsilon}^p} \bar{\sigma} L d\bar{\varepsilon}^p}{G_f} = \frac{\int_0^{\bar{u}^p} \bar{\sigma} d\bar{u}^p}{G_f} \tag{2.10}$$

Whereas an exponential damage parameter used for part 2 (chip zone), evolves according to:

$$D = 1 - \exp\left(-\int_0^{\bar{u}^p} \frac{\bar{\sigma}}{G_f} d\bar{u}^p \right) \tag{2.11}$$

The formulation of the model ensures that the energy dissipated during the damage evolution process is equal to G_f, and the scalar stiffness degradation approaches to one asymptotically at an infinite equivalent plastic displacement. In the case of plane strain condition, G_f can be obtained by $G_f = K_C^2(1-\nu^2)/E$ where K_C is the fracture toughness [MAT08].

Numerical integration scheme for Damage material

The adopted algorithm for the numerical integration of the elastic-plastic damage constitutive equations is based on the operator split concept. It results from the standard return mapping

algorithm with elastic predictor/plastic corrector format, widely used in computational plasticity [SIM98]. Let's consider what happens to a typical Gauss point of the finite element mesh within a (pseudo-) time interval $[t_i, t_{i+1}]$.

The incremental strain is given as following:

$$\Delta\boldsymbol{\varepsilon} = \boldsymbol{\varepsilon}_{i+1} - \boldsymbol{\varepsilon}_i \tag{2.12}$$

In order to have a consistency with the constitutive equations of the model, the values of stresses $\boldsymbol{\sigma}_i$, plastic strain $\boldsymbol{\varepsilon}_i^p$, equivalent plastic strain $\bar{\varepsilon}_i^p$, and damage D_i at the increment t_i are updated at the end of the time increment. The elastic predictor/plastic corrector return mapping algorithm for the elastic-plastic-damage model can be summarised as following:

(i) Step 1. Elastic predictor: at a given time t_i, the incremental strain, $\Delta\boldsymbol{\varepsilon}$, and the state variables permit to compute elastic trial stresses:

$$\left.\begin{aligned} \boldsymbol{\varepsilon}_{i+1}^{etrial} &= \boldsymbol{\varepsilon}_i^e + \Delta\boldsymbol{\varepsilon}, \\ \bar{\boldsymbol{\varepsilon}}_{i+1}^{ptrial} &= \bar{\boldsymbol{\varepsilon}}_i^p \\ \boldsymbol{s}^{trial} &= \boldsymbol{s}_i + 2G\Delta\boldsymbol{e}, \\ \boldsymbol{p}^{trial} &= \boldsymbol{p}_i + K\Delta\upsilon \\ D_{i+1}^{trial} &= D_{i.} \end{aligned}\right\} \tag{2.13}$$

In the above equations G, K, e, υ, and S are the shear and bulk moduli, the strain deviator, the volumetric strain and the deviatoric stresses, respectively. ($G = \frac{E}{2(1+\nu)}, K = \frac{E}{3(1-2\nu)}$)

(ii) Step 2. Plastic consistency check:

$$\Phi^{trial} = \frac{\sqrt{\frac{3}{2}}\left\|\boldsymbol{s}^{trial}\right\|}{(1-D_i)} - \left[\bar{\sigma}_{JC}\right] \tag{2.14}$$

IF $\Phi^{trial} \leq 0$, Then (Elastic state)

Update $(.)_{n+1} = (.)^{trial}$ return to step 1

ELSE (go to step 3: Compute plastic state)

(iii) Step 3. Find the equivalent plastic strain increment:

$$\Delta\bar{\varepsilon}^{p}=\frac{\Phi^{\text{trial}}\left(1-D_i\right)}{K+d\bar{\sigma}_{JC}/d\bar{\varepsilon}^{p}} \tag{2.15}$$

(iv) Step 4. Update the variables:

$$\left.\begin{aligned}
&\boldsymbol{s}_{i+1}=\left(1-\sqrt{\frac{3}{2}}\frac{2G\Delta\bar{\varepsilon}^{p}\left(1-D_i\right)}{\left\|\boldsymbol{s}^{\text{trial}}\right\|}\right)\boldsymbol{s}^{\text{trial}}\\
&p_{i+1}=p^{\text{trial}}\\
&\boldsymbol{\sigma}_{i+1}=\boldsymbol{s}_{i+1}+p_{i+1}\boldsymbol{I}\\
&\bar{\varepsilon}_{i+1}^{\text{p}}=\bar{\varepsilon}_{i}^{\text{p}}+\Delta\bar{\varepsilon}^{p}\\
&\boldsymbol{\varepsilon}_{i+1}^{e}=\frac{1}{2G}\boldsymbol{s}_{i+1}+\frac{1}{3K}p_{i+1}\boldsymbol{I}
\end{aligned}\right\} \tag{2.16}$$

Damage parameter D_{i+1} calculation:

IF $\omega\geq 1$ then Damage initiates

IF Linear degradation

$$D_{i+1}=\frac{\int_0^{\bar{\varepsilon}_{i+1}^{p}}\bar{\sigma}Ld\bar{\varepsilon}^{p}}{G_f}=\frac{\int_0^{\bar{u}_{i+1}^{p}}\bar{\sigma}d\bar{u}^{p}}{G_f} \tag{2.17}$$

where *n* is an integration increment.

ELSE IF Exponential degradation

$$D_{i+1}=1-\exp\left(-\int_0^{\bar{u}_{i+1}^{p}}\frac{\bar{\sigma}}{G_f}d\bar{u}^{p}\right) \tag{2.18}$$

END IF

ELSE

$$D_{i+1}=D_{i+1}^{trial}$$

ENDIF

ENDIF

RETURN

Mesh sensitivity

During machining process, large deformation is a common phenomenon, especially for the segmented chip. According to Eq. 2.9, to get this large deformation with constant element characteristic length L, the value of plastic strain must be very high, which also depends greatly on the local mesh. The characteristic length L could also be increased to reduce the mesh dependency. Consequently, the question that can be asked in the present formulation is: which size is appropriate for the characteristic length L?

Two constraints can be retained for the evaluation of L: First, the size should be relative large (to save computing time), second the result should be similar or close to experimental values (in terms of cutting force and chip morphology). For that, four mean values of mesh were discussed with characteristic lengths of 4, 6, 8, and 10 μm. The corresponding simulated cutting forces were compared with the experimental ones.

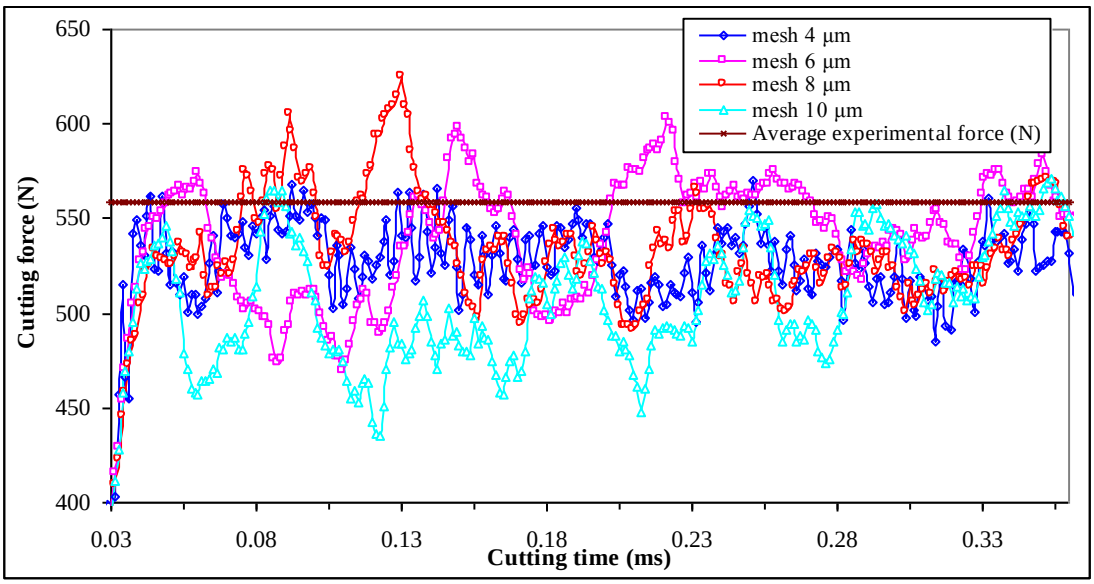

Fig. 2.4 Cutting force sensitivity versus cutting time with different mesh sizes

Fig. 2.4 presents the cutting force sensitivity for different mesh sizes. It should be mentioned that the direction of the cutting force extracted is the same as that of the cutting speed V_C (X direction), and the direction is also kept the same for the following research work. It can be seen that the cutting force, in all the four mesh groups, vary around the average experimental value [UMB08, JIA04], especially when the cutting time is larger than 0.3 *ms*. The chip formation shows that mesh 8 μm, mesh 6 μm and 4 μm can well capture the shear localization. To make a compromise between both computing cost and accuracy, the mesh size 8 μm was

chosen for the parametric study, and this mesh size is kept as a constant value in chip (Part 2) for all the following simulation tests.

2.4 Limiting shear stress from the aspect of contact mechanics

The Zorev's temperature independent stick-slip friction model [ZOR63], see Eq. 2.19, was widely adopted by many authors [SUB08, LIU00] to define the friction properties at the tool - chip interface. Zorev advocated the existence of two distinct tool-chip contact regions: In the stick zone near the tool tip the shear stress τ_f is assumed to be equal to the yield shear stress of the material being machined, τ_Y, whereas, in the sliding region, the frictional stress is lower than the yield shear stress. Note that a constant Coulomb coefficient of friction (CoF) is assumed here.

$$\begin{cases} if \quad \tau_f < \tau_Y \quad \& \quad \tau_f = \mu\sigma_n \quad \longrightarrow \quad Sliding\ region \\ if \quad \tau_f = \tau_Y \quad \& \quad \tau_f \le \mu\sigma_n \quad \longrightarrow \quad Stick\ region \end{cases} \tag{2.19}$$

The yield shear stress τ_Y, in Eq. 2.19 is usually related to the conventional yield stress σ_Y of the workpiece material adjacent to the surface [SHI02, HAG08]. A reasonable upper bound estimation [ABA10] of the yield shear stress can be calculated by the von Mises criterion:

$$\frac{1}{6}\{(\sigma_1-\sigma_2)^2+(\sigma_2-\sigma_3)^2+(\sigma_3-\sigma_1)^2\} \le \tau_Y^2 = \sigma_Y^2/3 \tag{2.20}$$

In which σ_1, σ_2 and σ_3 are the principal stresses, and τ_Y and σ_Y denote the yield stress values of the material in both simple shear stress and tension, respectively.

However, when the CoF is relatively small, the maximum shear stress is found beneath the contact surface. If this maximum value is adopted to define the limiting shear stress, the material beneath the contact surface will yield before the surface material reaches the critical value. So, it is necessary to redefine the critical limiting shear stress. The latter is introduced in detail from the point of view of contact mechanics by considering the relationship between the CoF and temperature.

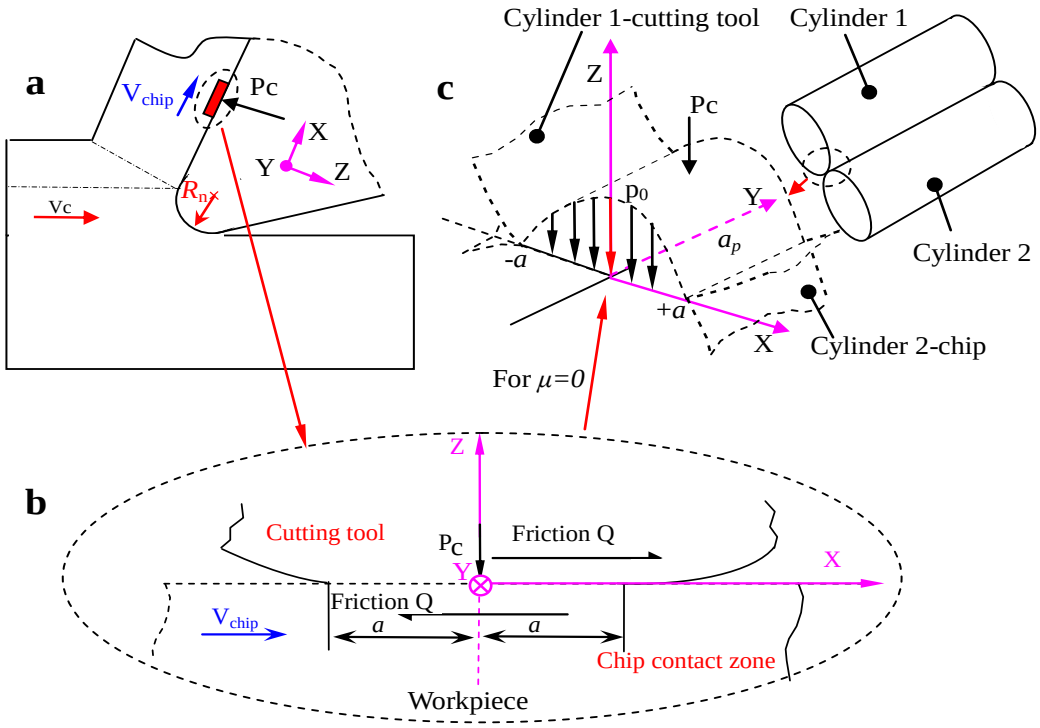

Fig. 2.5 Simplified contact model at the tool-chip interface.

Fig. 2.5 schematizes the tool and chip contact. The tool is fixed and the workpiece moves at the cutting speed *Vc* from left to right. To analyze the contact condition, a small region at the interface was considered with a sliding rate V_{chip} and a normal force Pc per length unit. More precisely the contact model was simplified according to Fig. 2.5(b) which consists of a flat surface slider moving from left to right over a curved profile and with a steady velocity $V_{chip.}$ For frictionless elastic contact and when the contact dimensions are small compared to the size of the contacting bodies (Hertz assumptions), the solution is well described by the Hertz theory [JOH85b]. The plane strain problem is equivalent to the contact between two cylinders, see Fig. 2.5(c), where *a* is a distance representing the half contact width and p_0 is the maximum pressure at the contact centre. It is important to note that the contact pressure is distributed with a semi-elliptical shape between [-*a*, *a*] along the x-axis. The load at which material yield begins is related to the yield threshold of the softer material (here the workpiece) in a simple tension or shear test through an appropriate yield criterion [JOH85b].

2.4.1 Frictionless contact between two cylinders

According to Johnson [JOH85b], under a normal force Pc (per length), the stress field distribution in the chip (here schematized by cylinder2) is given by Eq. 2.21 below:

$$\begin{cases} (\sigma_x)_p = -\dfrac{p_0}{a}\left\{ m_1\left(1+\dfrac{z^2+n_1^2}{m_1^2+n_1^2}\right)-2z \right\} \\ (\sigma_z)_p = -\dfrac{p_0}{a} m_1\left(1-\dfrac{z^2+n_1^2}{m_1^2+n_1^2}\right) \\ (\sigma_y)_p = \nu((\sigma_x)_p+(\sigma_z)_p) \\ (\tau_{xz})_p = -\dfrac{p_0}{a} n_1\left(\dfrac{m_1^2-z^2}{m_1^2+n_1^2}\right) \\ (m_1^2)_p = \dfrac{1}{2}\left[\{(a^2-x^2+z^2)+4x^2z^2\}^{0.5}+(a^2-x^2+z^2)\right] \\ (n_1^2)_p = \dfrac{1}{2}\left[\{(a^2-x^2+z^2)+4x^2z^2\}^{0.5}-(a^2-x^2+z^2)\right] \end{cases} \quad (2.21)$$

In the case of plane strain, the principal stresses can be calculated by Eq. 2. 22.

$$\begin{cases} \sigma_{1,2} = \dfrac{(\sigma_x)_p+(\sigma_z)_p}{2} \pm \sqrt{\left(\dfrac{(\sigma_x)_p+(\sigma_z)_p}{2}\right)^2+(\tau_{xz})_p} \\ \sigma_3 = (\sigma_y)_p = \nu((\sigma_x)_p+(\sigma_z)_p) \end{cases} \quad (2.22)$$

The shear stress distribution in the (X, Z) plane is shown in Fig. 2.6 for various friction coefficients. For frictionless contact the maximum shear stress reaches 0.31574 p_0 at a depth $z=-0.72\,a$. Note that for frictionless contact, the maximum shear stress is found at a location far from the surface whereas it reaches the surface when the CoF is equal or higher than 0.48. Consequently, for frictionless contact or when the CoF is lower than 0.48, it is necessary to consider the shear stress at the contact surface as the limiting shear stress, not the maximum one which is located at the hertzian depth.

2.4.2 Frictional contact between two cylinders

In presence of friction the contribution of the tangential force *Q*, acting on each contact surface along the direction opposed to the motion (see Fig. 2.6 (b)) should be also considered:

$$\begin{cases} (\sigma_x)_q = \dfrac{q_0}{a}\left\{ n_1\left(2 - \dfrac{z^2 - m_1^2}{m_1^2 + n_1^2}\right) - 2x \right\} \\ (\sigma_z)_q = \dfrac{q_0}{p_0}(\tau_{xz})_p \\ (\sigma_y)_q = \nu((\sigma_x)_q + (\sigma_z)_q) \\ (\tau_{xz})_q = \dfrac{q_0}{p_0}(\sigma_x)_p \end{cases} \tag{2.23}$$

Where $q_0 = \mu p_0$ is the tangential traction at $x = 0$, and the suffixes p and q refer to the stress components due to normal pressure and tangential traction, respectively. Also, it is assumed that the tangential traction has no effect upon the normal pressure distribution. When superimposed to the effect of the contact pressure (normal effect) it yields:

$$\begin{cases} \bar{\sigma}_x = (\sigma_x)_q + (\sigma_x)_p \\ \bar{\sigma}_y = (\sigma_y)_q + (\sigma_y)_p \\ \bar{\sigma}_z = (\sigma_z)_q + (\sigma_z)_p \\ \bar{\tau}_{xz} = (\tau_{xz})_q + (\tau_{xz})_p \end{cases} \tag{2.24}$$

Fig. 2.6(b) presents the counter plots of the shear stress in the contact zone between the chip and the tool for a relatively low CoF, here 0.2. It is noticed that the maximum shear stress is still below the contact interface. This maximum shear stress moves towards the interface when increasing the CoF as shown in Fig. 2.6 (c) and (d). It reaches the surface when $\mu \geq 0.48$. Whereas only one point is concerned when $\mu = 0.48$ (see Fig. 2.6 (d)).

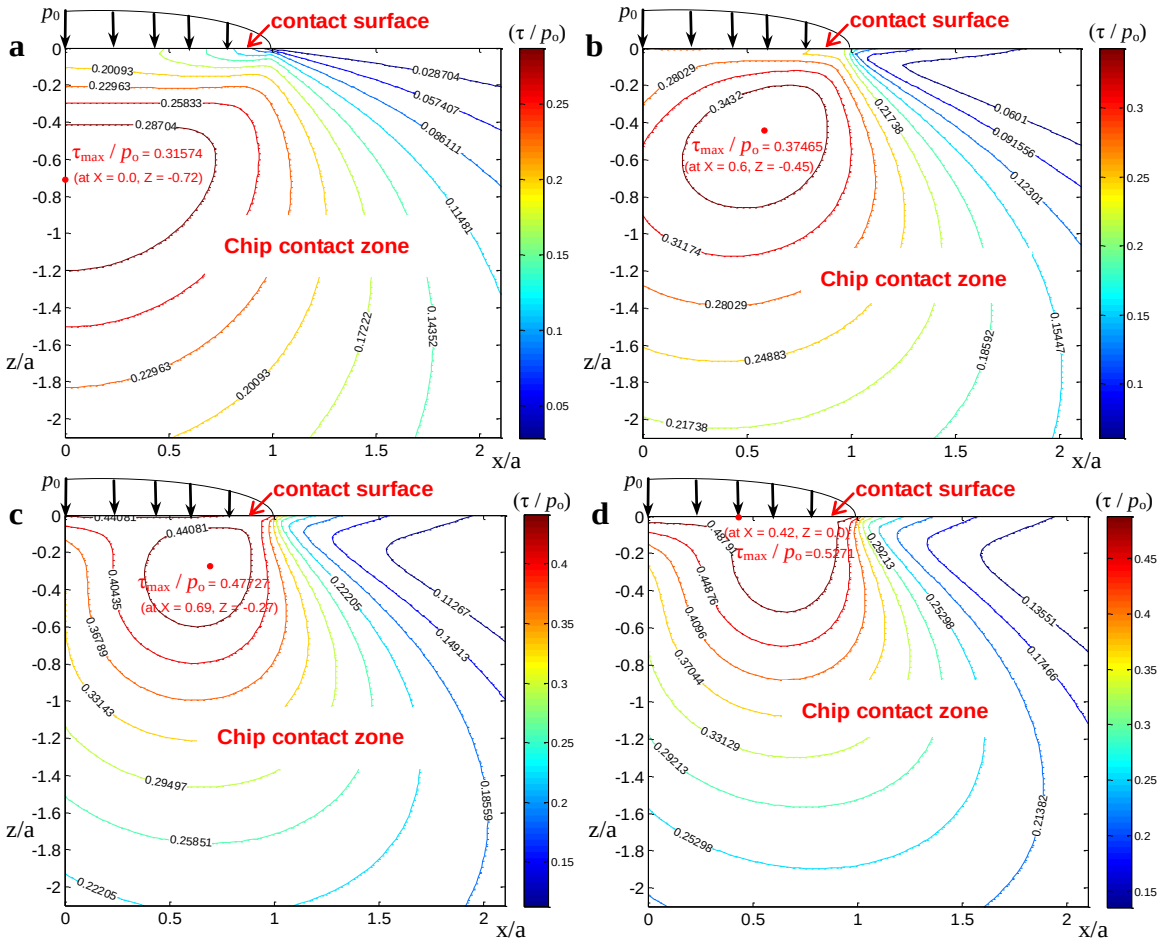

Fig. 2.6 Contour plot of shear stress in chip contact zone for different CoFs:

a) μ = 0.0, b) μ = 0.2, c) μ = 0.4 d) μ = 0.48

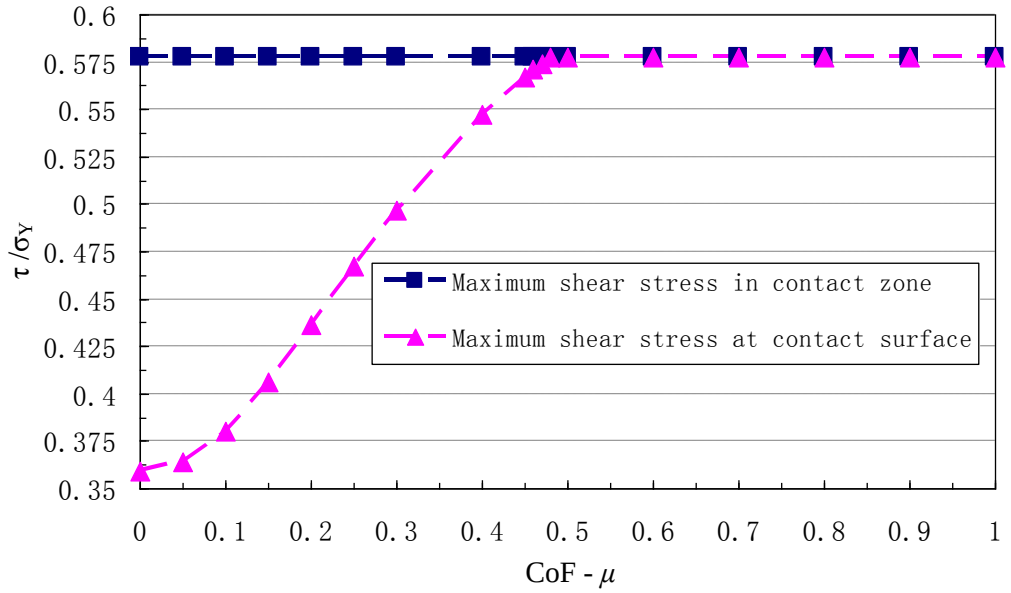

Fig. 2.7 Ratio of the limiting shear stress and σ_Y versus CoF at a given temperature

Fig. 2.7 presents the maximum shear stress conditions at the surface and below the contact versus the CoF. Results are normalized by the material yield stress σ_Y. It can be seen that the maximum shear stresses are totally different when the CoF is less than 0.48. When the CoF is higher than 0.48, the maximum shear stress is located at the contact interface and is equal to $1/\sqrt{3}\,\sigma_Y$.

In practical condition, the yield stress σ_Y is updated according to variations with temperature, strain rate, etc. So, it is necessary to identify the accurate limiting shear stress at the contact interface. According to Komanduri and Hou [KOM02], the yield stress of Ti–6Al–4V evolving with temperature, by taking into account the results given in Fig. 2.7, it is possible to draw the limiting shear stresses versus temperature for different CoFs as shown in Fig. 2.8. It can be noticed that the higher the CoF, the higher the limiting shear stress, whereas the latter decreases monotonously when the temperature increases. Therefore, both CoF and temperature influence the limiting shear stress. The assumption of constant threshold shear stresses regardless the frictional properties and temperature is no more valid.

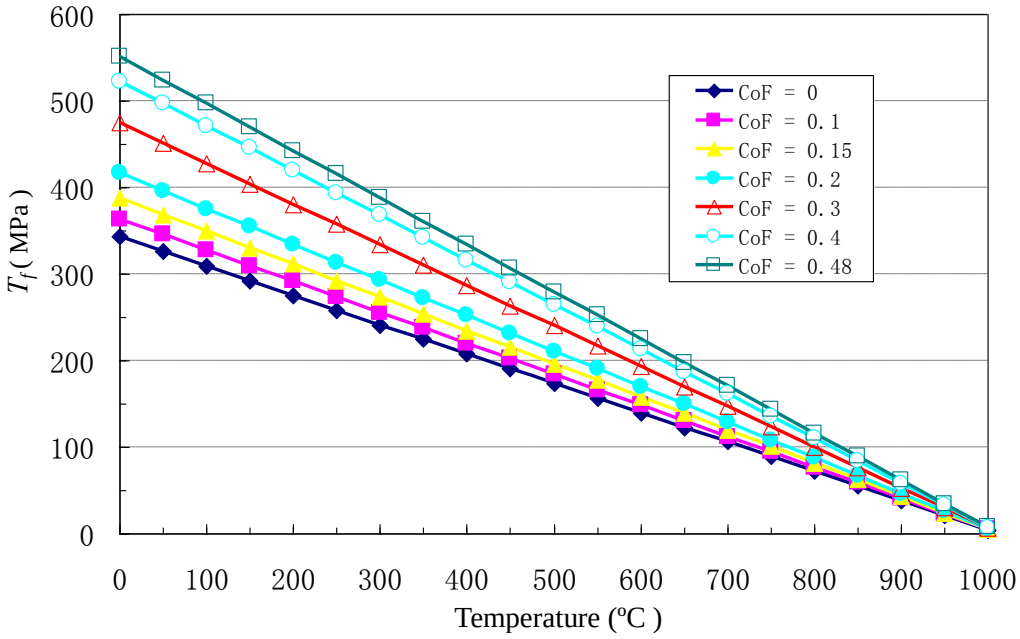

Fig. 2.8 Limiting shear stress versus temperature for different CoFs

It is important to underline that this figure is drawn only for CoFs varying between 0 and 0.48. Indeed, for CoF higher than 0.48, the limiting shear is found at the surface and is equal to $1/\sqrt{3}\,\sigma_Y$ (see Fig. 2.7), and the limiting shear stress is applied in the cutting model by user subroutine VFRIC.

2.5 Concluding remarks

The present work is based on an energetic concept and a refined limiting shear stress to build a multi-part cutting model under Abaqus\Explicit:

- To achieve material degradation process and reduce the mesh dependence, the fracture energy is introduced for the material damage. Wherein the numerical integration scheme applied for damage material was presented.

- In order to obtain the appropriate model mesh size, a mesh sensitivity analysis was performed.

- The limiting shear stress at the tool-chip contact surface was adopted as a friction model from the aspect of contact mechanics. It was first shown that the surface shear stress is controlled by the contact pressure and the CoF. A relationship between the CoF and the limiting shear stress has been given. The effect of the temperature on the limiting shear stress has been also considered.

- This improved friction contact model will be applied to the cutting model, the simulation and validation test will be performed in the next chapter.

3 Bulk material level cutting model validation and application

To validate the methodology adopted for the elaboration of the cutting model presented in chapter 2, experimental machining test was carried out. The simulation results, in terms of chip morphology and cutting forces, were performed in order to be compared to experiments from our machining tests and those from literatures. In the following, parametric study of the influence of cutting speed and feed rate on chip formation was proposed. Moreover, residual stress prediction model was also developed and validated with experiments.

3.1 Experimental studies

In order to have detailed idea about cutting of the Titanium alloy Ti–6Al–4V, some experiments were carried out at the machining platform of ENISE de St Etienne. The orthogonal cutting is retained for more simplicity and the correspondent experimental set-up is shown in Fig. 3.1. The cut material geometry is a disk fixed on the clamping apparatus, the cutting movement is limited to radial direction. Also, a quick stop technology is carried out by stopping the spindle rotation and withdrawing the tool holder at the same time.

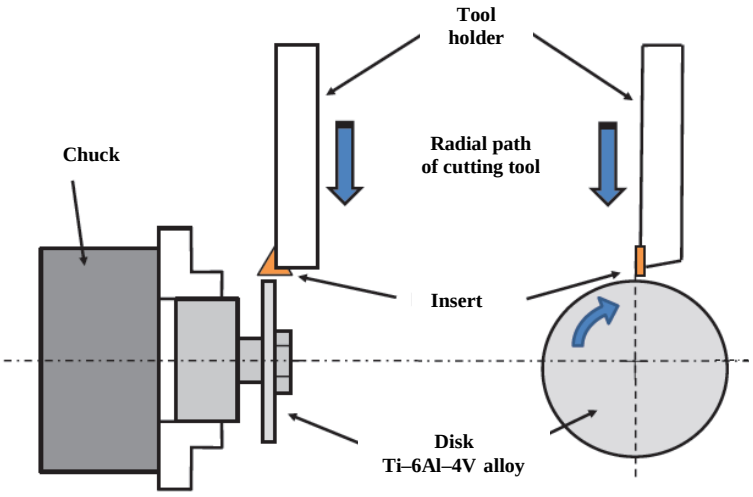

Fig. 3.1 Schematic illustration of the adopted orthogonal machining operation.

Wherein the geometry and type of the uncoated carbon insert is illustrated in Fig. 3.2 and Table 3.1. Due to the design of the tool holder, the rake angle is limited to 0° in all the cutting tests.

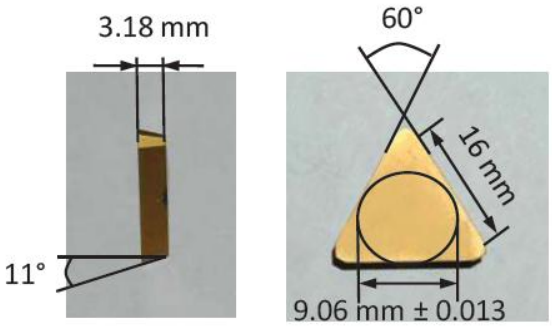

Fig. 3.2 Details of insert geometry.

T	P	K	N	16	03	PP	R
Triangular insert	Flank angle 11°	Tolerance of 0.013 mm of the height	No chip breaker	Edge length 16mm	Thickness 3.18mm	2 bevels 90 °	Round edge

Table 3.1 Geometrical characteristics of the Insert TPKN 1603 PPR

With above machining system, the final state of the disk and its chip after the quick stop is shown in Fig. 3.3. It can be observed that the chip is not yet removed from the workpiece, this makes sure on the one side that the removed feed rate is the real input one at the last rotation (which will greatly influence the measured surface integrity), on the other side all the collected chips are under the same cutting condition.

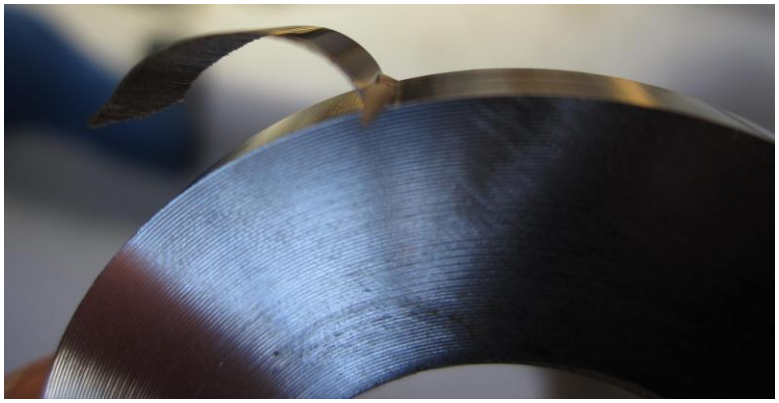

Fig. 3.3 Final state of the machined disk

In order to investigate the effect of cutting conditions on chip formation and the machined surface integrity, the planned experimental cutting parameters are presented in Table 3.2.

Feed rate, f (mm)	0.1, 0.15, 0.2
Cutting speed, V_c (m/min)	30, 60, 90, 120
CoF, μ	0.7
Rake angle, γ_0 (deg)	0
Clearance angle, α_0 (deg)	11
Cutting width a_p (mm)	3
Cutting edge radius R_n (μm)	30

Table 3.2 Simulation parameters used in the experimental study

3.1.1 Definition of the scale

In order to well evaluate the characteristics of machining process and simulation model, the scale definition is noticed before performing the following works. According to Schmauder's works [SCH02], three scale levels are defined as Fig. 3.4:

- **The macroscopic scale**: represents scale larger than the Representative Volume Element (REV) when considering the grain level, which includes the microstructure model and bulk material model, mainly for engineering application, with the size larger than 300 μm.
- **The mesoscopic scale**: represents the study in material microstructure grain scale level with the size from 0.6 μm to 300 μm.

- **The microscopic scale**: focus on the study of crystallographic level, with the size less than 0.6 μm.

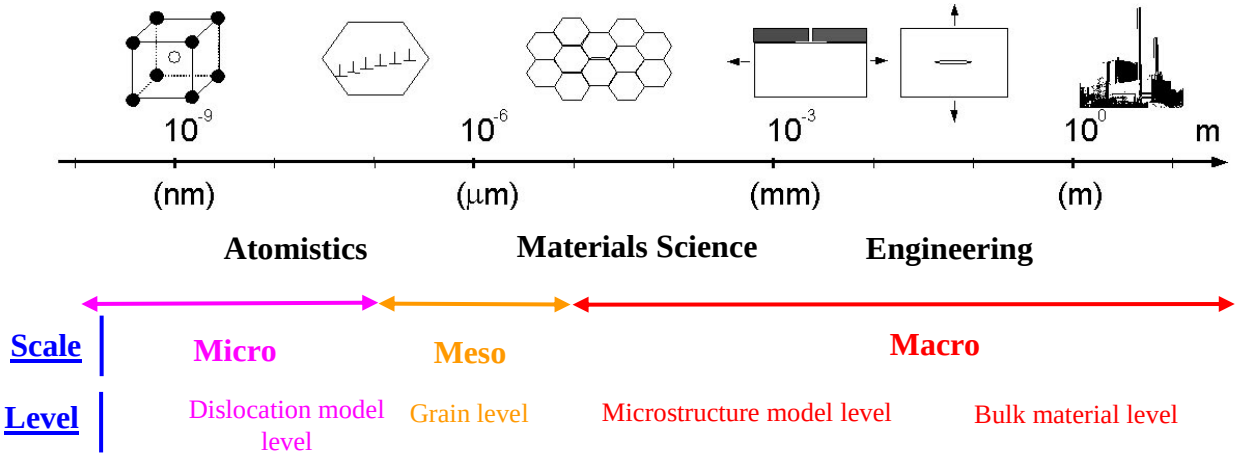

Fig. 3.4 Numerical methods referring to different length scales [SCH02]

The numerical cutting model developed in this thesis focuses on the macroscopic scale which contains microstructure model level and bulk material level, and the validation and parametric study for bulk level model is firstly performed.

3.1.2 Chip formation at macroscopic scale

As shown in Fig. 3.5, the chip formation from macroscopic aspect is presented to give the general idea of its morphology evolution during cutting for different working parameters. It can be obviously seen that the chip curve radius will increase and chip becomes less continuous with the cutting speed and feed rate increase. The chip becomes broken (fragmentation phenomenon) when cutting speed larger than 90 m/min (with constant feed rate 0.1 mm/rev) and feed rate bigger than 0.2 mm/rev (with constant cutting speed 60 m/min).

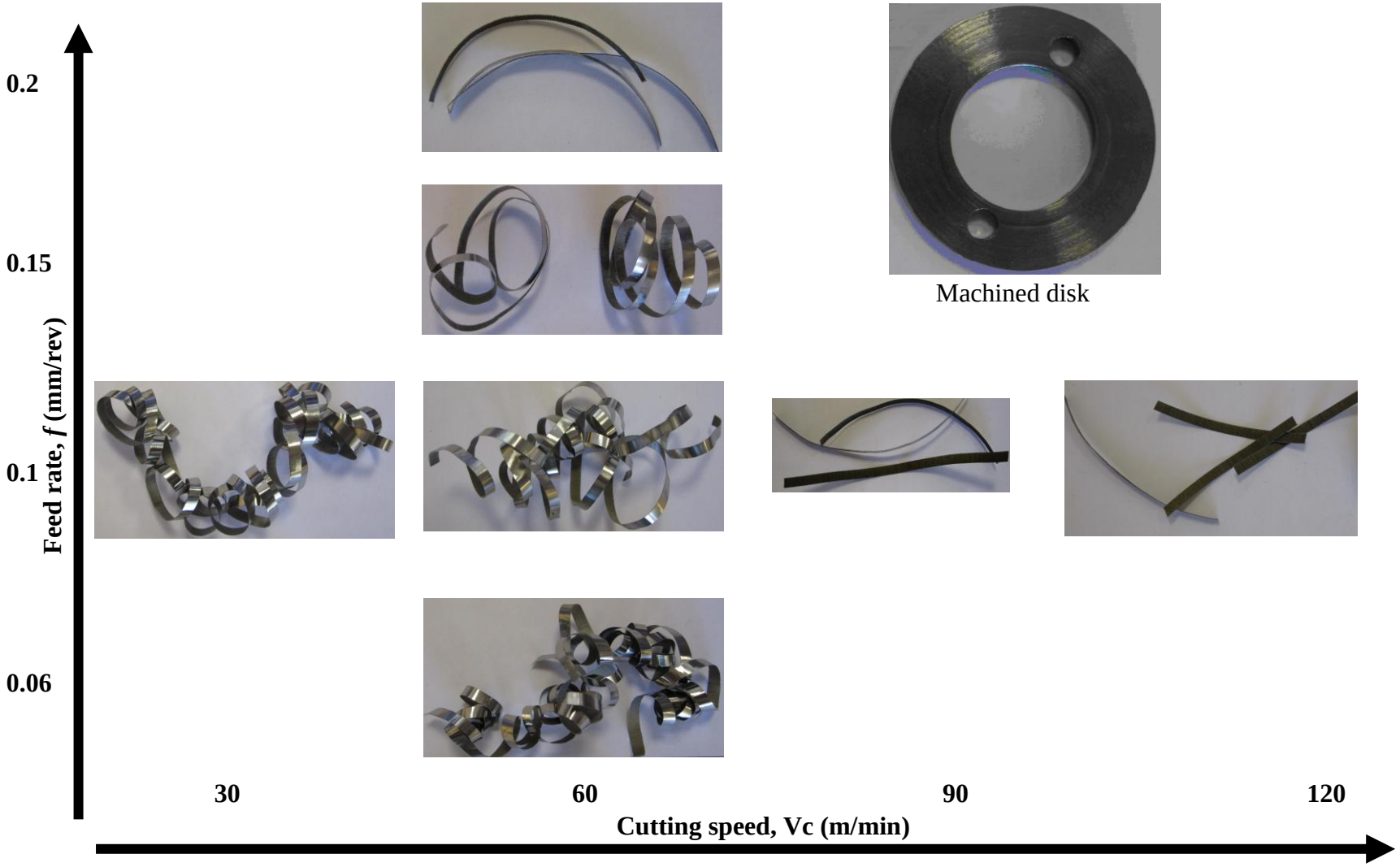

Fig. 3.5 Macroscopic shape of the collected chip (Ti–6Al–4V)

3.1.3 Chip formation with microstructure

However, the macro chip formation study is not enough when the surface integrity has to be analyzed, especially the microstructure level model is introduced in present work. Finally, the local explicit metal phase in the transversal section of the chip is obtained after polishing and chemical erosion, the microstructure of the chip with seven conditions is given in Fig. 3.6 below. Note that on these photos, the cut surfaces of the chip is situated below, while the free surface dominated in a segmented form is located in the upper.

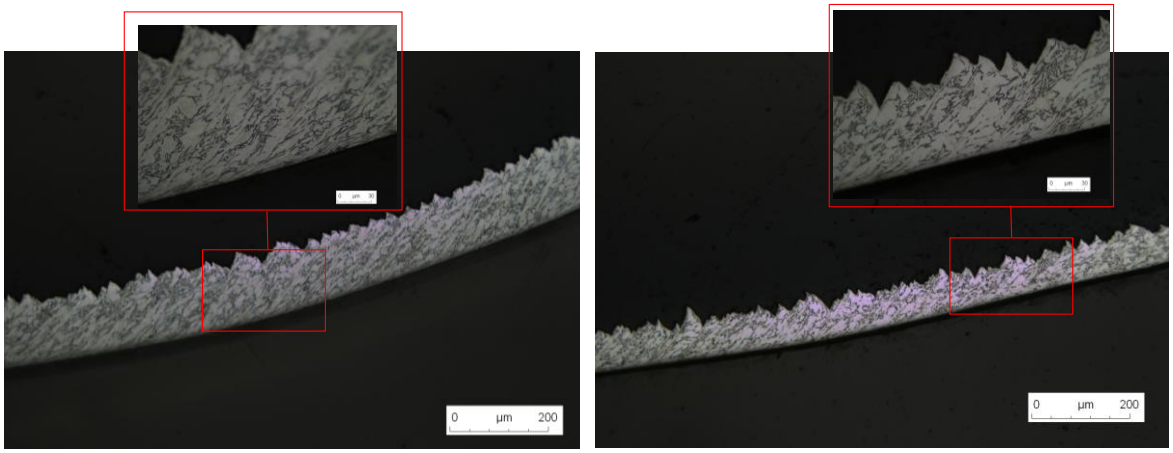

a) V_c = 30 m/min, f = 0.1 mm/rev, a_p = 3 mm *b)* V_c = 60 m/min, f = 0.06 mm/rev, a_p = 3 mm

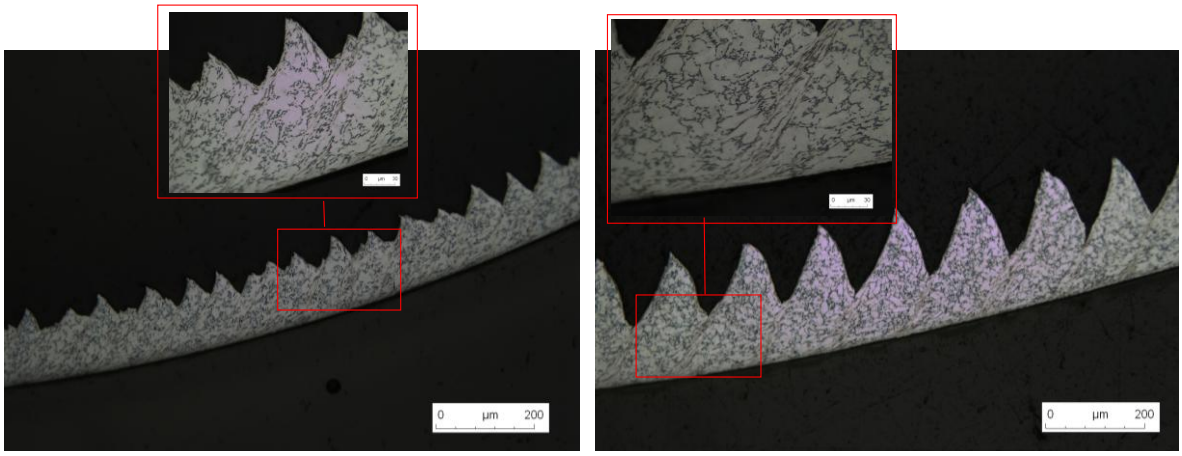

c) V_c = 60 m/min, f = 0.1 mm/rev, a_p = 3 mm *d)* V_c = 60 m/min, f = 0.15 mm/rev, a_p = 3 mm

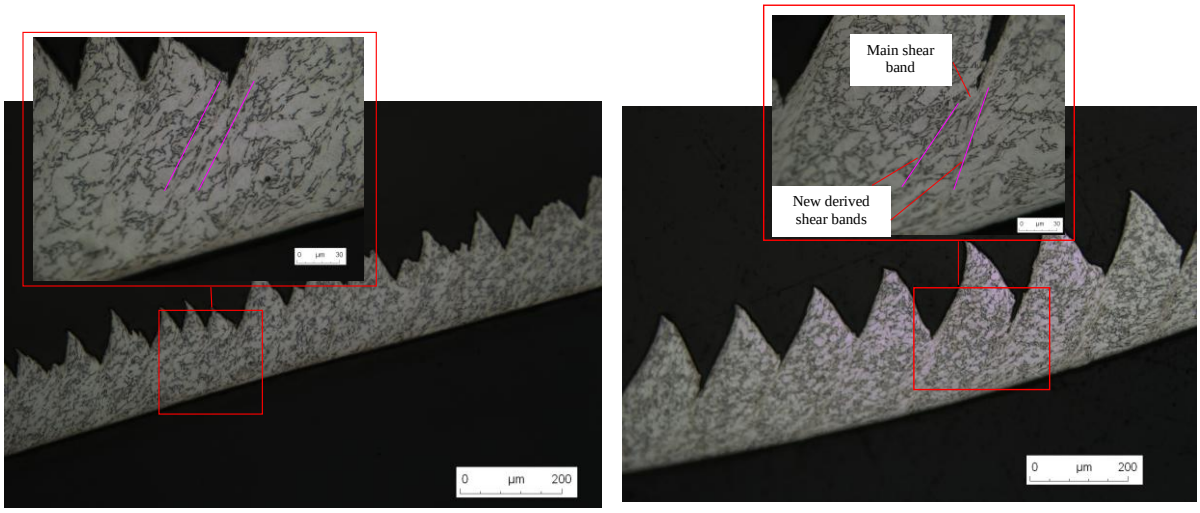

e) V_c = 90 m/min, f = 0.1 mm/rev, a_p = 3 mm *f)* V_c = 60 m/min, f = 0.2 mm/rev, a_p = 3 mm

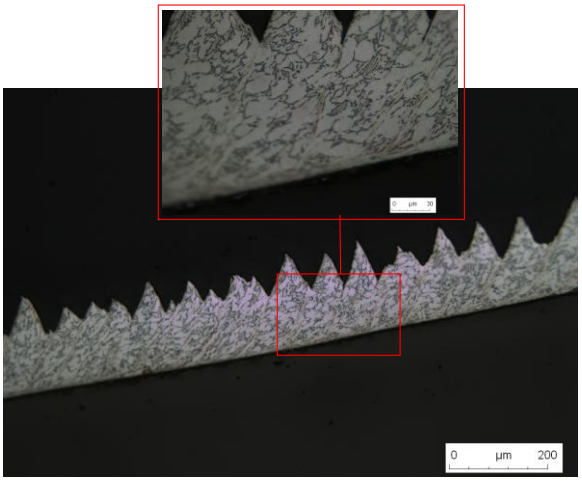

g) V_c = 120 m/min, f = 0.1 mm/rev, a_p = 3 mm

Fig. 3.6 Morphologies of the machined chip with microstructure

Generally speaking, the chip is more segmented when increasing cutting speed and feed rate, and it should be noted that there are no periodic segmentation when feed rate is lower than 0.15 mm/rev, the chip formation process is mainly influenced by the heterogeneity of grain distribution. While periodic segmentation appears with higher feed rate for the average effect of the increased grain number which tends to homogeneous distribution for the chip. So, the influence of feed rate is more obvious compared with cutting speed.

Moreover, the shear bands are clearly shown in Fig. 3.6, and the cracks are usually at the end of the shear bands between grain interfaces (Take Fig. 3.6 *e*) and *f*) for example). Another phenomenon is that two shear bands are derived from the path of the main shear band because of relative hard phase prevent the propagation of the previous shear band (Fig. 3.6 *f*)).

3.2 Numerical cutting model validation

In order to validate the model developed in the present work, the numerical results presented are compared with experimental data mainly gathered from present experiments and literatures [UMB08, JIA04, CAL08].

In the present model, the failure of material is based on the work of Pirondi and Bonora [PIR03], where, as described in experiment and simulation, crack starts to take place when the scalar stiffness degradation (SDEG) is larger than 0.74. This value can be taken as the critical value for determining the material failure occurrence.

3.2.1 Model calibration with positive tool rake angle

The simulation carried-out following Jiang and Shivpuri's [JIA04] data gives the result shown in Fig. 3.7 (a). It can be seen that the periodic cracks initiate at the free surface of the cutting material ahead of the tool and are propagating towards the tool tip. This result agrees with the works of Vyas and Shaw [VYA99]. The chip valley is measured from the boundary of failure zone (SDEG = 0.74) to the new formed free surface for considering crack. It should be noted that the original chip collected from the turning test was a curled chip. The collected chip was then straightened and mounted. After etching and polishing the chip morphology, shown in Fig. 3.7 (b) was obtained from the mounted chip as presented in [JIA04]. The adopted CoF is 0.7 in the model from the work of Umbrello [UMB08]. The limiting shear stress at the tool/workpiece interface is presented in Fig. 2.7. For CoF higher than 0.48, the limiting shear stress is located at the contact surface of the workpiece and is equal to $1/\sqrt{3}\,\sigma_Y$. For calculation, the limiting shear stress evolution is programmed in the cutting model via a user subroutine VFRIC implemented in Abaqus/explicit.

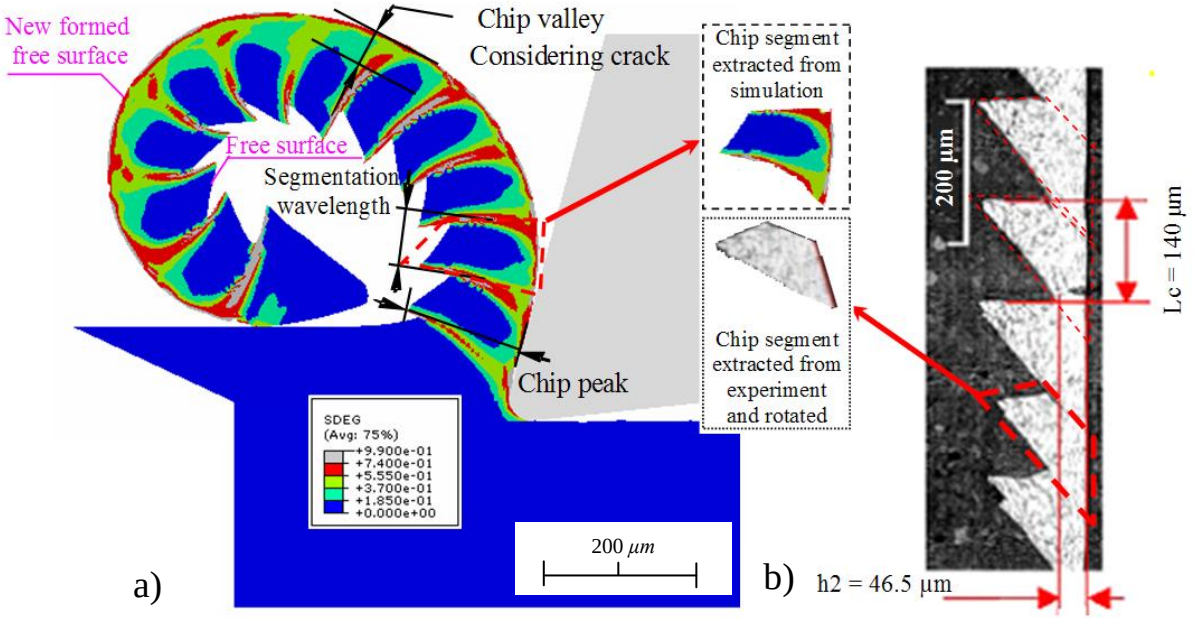

Fig. 3.7 Chip morphology obtained at V_c = 120 m/min, f = 0.127 mm/rev with rake angle and flank angle of 15°and 6°: a) computation considering the scalar stiffness degradation (SDEG = 0.74), b) Experimental comparison with [JIA04]

Due to many uncertain factors in the experiment and chip post-treatment (etching, hand manipulation, etc), the shape of simulated chip segment is not exactly the same compared to that of experimental one. Nevertheless, its global morphology (Fig. 3.7) is fairly similar that given by experimental tests [JIA04]. Moreover, it can be underlined that, the shape of the chip segment obtained by simulation in the case of Fig. 3.7 has great similarities to that given in the interesting numerical and experimental works carried out by Baker [BAK06] and Semiatin [SEM83], respectively, even though the cutting conditions were different.

In addition, a comparison between the concerned numerical results and those obtained experimentally is given in Table 3.3. An acceptable agreement is observed.

V_c = 120 (m/min)	L_c (μm)	Peak (μm)	Valley (μm)	Fc [UMB08] (N)
Experiment [JIA04]	140	165	46.5	559
Simulation	133 ± 8	162 ± 7	48 ± 19	541.3
Error (%)	-5	-2	4.35	-3.17

Table 3.3 Comparison between experimental and numerical results for positive rake angle

3.2.2 Model calibration with zero tool rake angle

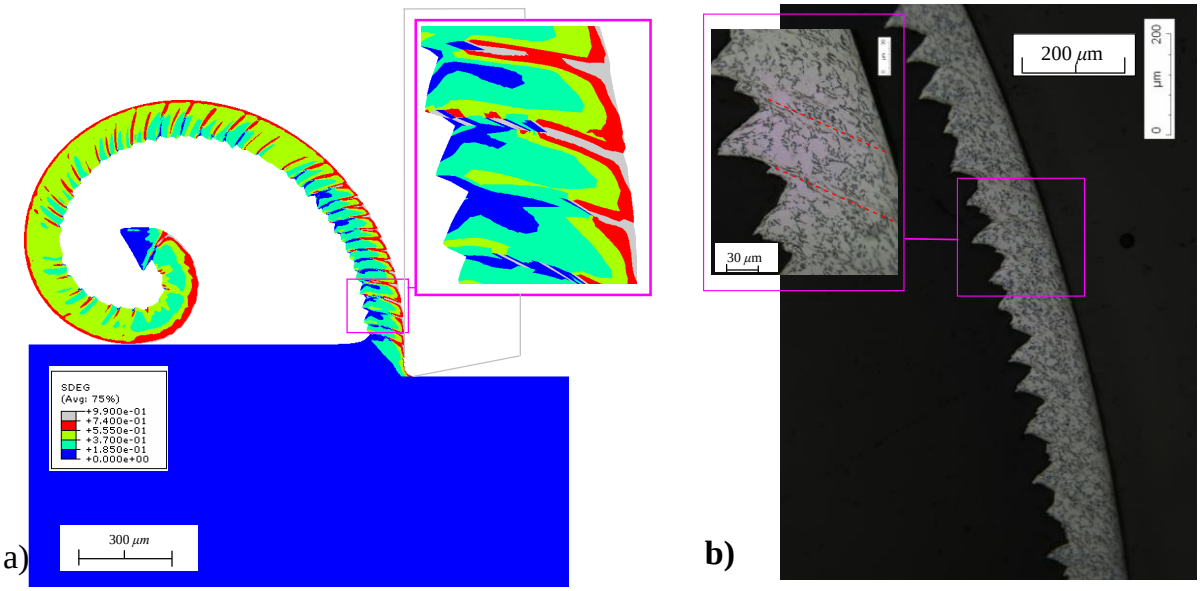

Fig. 3.8 Chip morphologies for f = 0.1 mm/rev, V_c = 60 m/min with rake angle and flank angle of 0° and 11°: a) Simulation result, b) Experimental one

To well calibrate the FE model, cutting parameter of f = 0.1 mm/rev, V_c = 60 m/min with zero tool rake angle in present experiment is adopted. Compared the simulation chip to experimental one, a similar chip segmentation is found. The damage initiation locates at the new formed free surface (Fig. 3.8 a)) which opposites the situation with positive tool rake angle (Fig. 3.7 a)), where the damage initiation starts from the free surface. Moreover, experimental result show that the chip segmentation is less periodic, which is mainly caused by the heterogeneity of the grain distribution, especially for the small feed rate. The average chip information and cutting force are listed in Table 3.4.

V_c = 60 (m/min)	L_c (μm)	Peak (μm)	Valley (μm)	F_c (N)
Experiment	64±17	143±6	94±7	613±47
Simulation	58 ± 8	125 ±10	100 ± 5	628±60
Error (%)	-9	-12	4.25	2.4

Table 3.4 Comparison between experimental and numerical results for zero rake angle

From the compared results presented in Table 3.4, the simulation model shows quite well predicted cutting force with slight error of 2.4%. Besides the similar chip shape illustrated in Fig. 3.8, the maximum error of the average values of chip geometrical characteristic lengths is within 15%.

3.2.3 Model calibration with negative tool rake angle

Another comparison was made with Calamaz's [CAL08] experiment (Fig. 3.9). In the case of a cutting speed of 60 m/min, the chip segment is the result of periodic cracks. Crack initiation takes place both at tool tip and the free surface ahead of the tool tip. The failure zone at tool tip is presented in the form of a secondary shear zone [REC04] (Fig. 3.9 a)), while the propagation of the failure zone at the free surface only reached the half of chip thickness arising from the lower shear strain rates in the upper region of the primary shear zone.

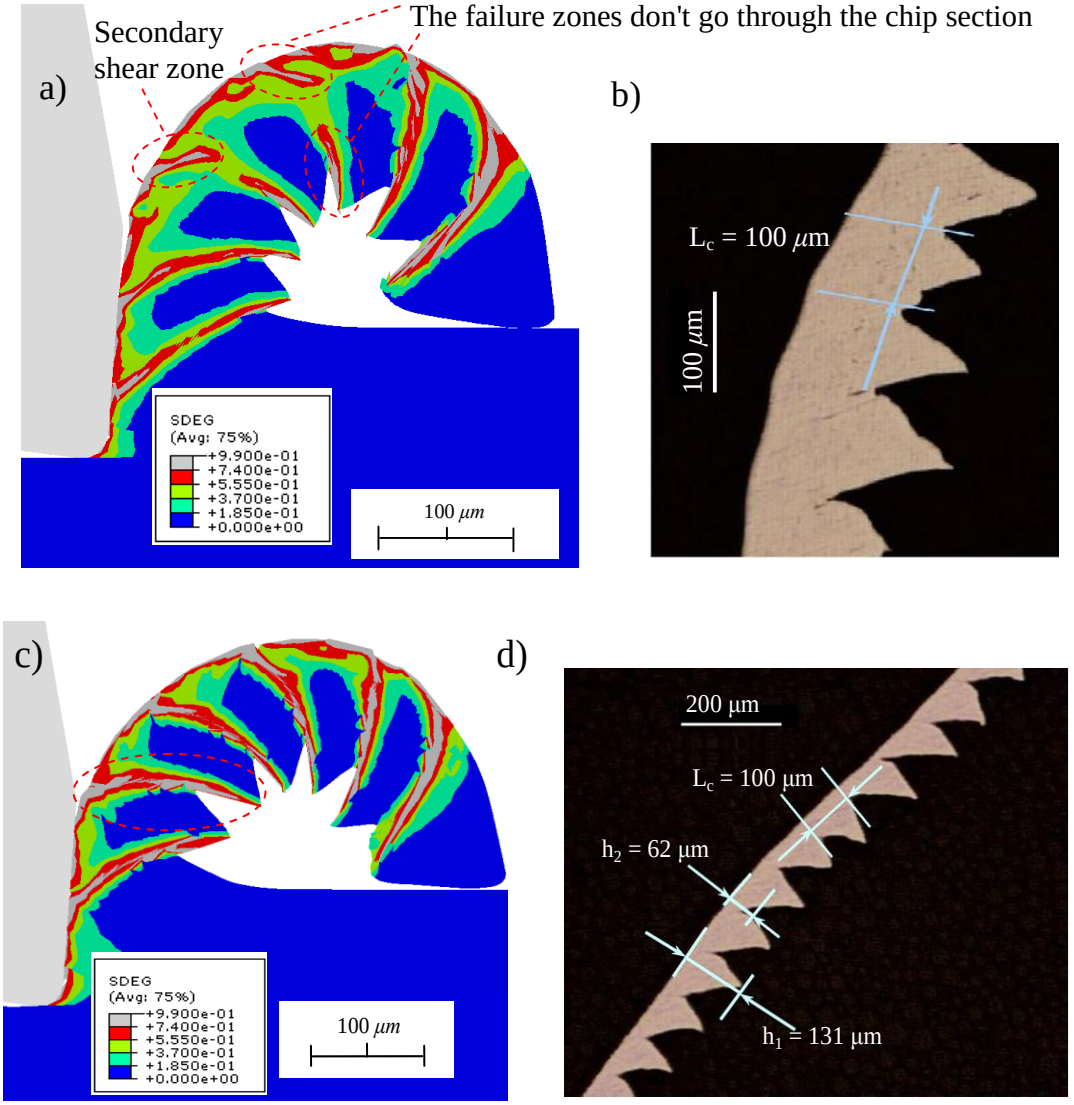

Fig. 3.9 Chip morphologies of f = 0.1 mm/rev with rake angle and flank angle of -4° and 7° : a) Simulation of V_c = 60 m/min,
b) Experiment of V_c = 60 m/min, c) Simulation of V_c = 180 m/min, d) Experiment of V_c = 180 m/min [CAL08]

When the cutting speed increases up to 180 m/min, the failure zone (with the stiffness degradation larger than 0.74) goes through the primary shear zone from two sides in and out,

as shown in Fig. 3.9 c), which is different form Luttervelt [LUT77], who discovered the occurrence of a crack at the tool tip and its propagation towards the free surface, which is also different from Vyas and Shaw [VYA99] as it was mentioned above when the rake angle is positive.

V_c (m/min)	Methods	L_c (μm)	Peak h_1 (μm)	Valley h_2 (μm)	F_c (N)
60	Experimentation [CAL08]	100	N/A	N/A	557
	Simulation	96 ± 10	136 ± 2	94 ± 4	600
	Error (%)	-4			7.7
180	Experimentation [CAL08]	100	131	62	548
	Simulation	96 ± 8	132 ± 5	77 ± 9	580
	Error (%)	-4	0.8	24	5.8

Table 3.5 Comparison between experimental and numerical results for negative rake angle

When the cutting speed increases, the stiffness degradation in the primary shear zone accelerates chip deformation in further steps: the chip valley becomes smaller (Table 3.5), while the chip wavelength and peak are hardly affected. The cutting forces in these two conditions are larger than the experimental value for the negative rake angle, while the errors are less than 10 % for the chip valley. As the damage zone goes through the whole chip section for the cutting speed of 180 m/min, the simulated value of chip valley without considering damage is adopted. For that, the error reaches at 24 % compared to experimental one. However, the cracks in the experimental chip sample have the tendency to go through the whole chip section, as presented in Fig. 3.9 d).

In summary, it can be said that simulation results of the model proposed show good agreements with Shivpuri's and Calamaz's experiments, and the experiments carried out by the author. It permits to predict the chip morphology and the cutting force with a good approximation. Moreover, it seems that the appropriate values of the limiting shear stress are well forecasted.

It is also found that the chip morphology is different with positive and negative rake angle cutting tool. Indeed, for positive rake angle tool, the periodic cracks initiate at the free surface of the machined material ahead of the tool and propagate partway toward the tool tip. For zero rake angle tool, the periodic cracks initiate at the new formed surface. While for negative rake angle tool, the periodic cracks initiate at two free faces in and out, go through the primary shear zone, and join in together forming the shear band zone at high cutting speed.

3.3 Parametric study of Ti–6Al–4V cutting

With the new proposed model, a numerical parametric study concerning chip morphology in the orthogonal cutting of Ti–6Al–4V was performed. The process simulation parameters are listed in Table 3.6.

Feed rate, f (mm)	0.06, 0.1, 0.127
Cutting speed, V_c (m/min)	60, 120, 180
CoF, μ	0.3, 0.7, 1
Rake angle, γ_0 (deg)	15, -6, -4
Cutting width a_p (mm)	2.54
Clearance angle, α_0 (deg)	6, 12
Cutting edge radius R_n (μm)	30

Table 3.6 Simulation parameters used in the study

3.3.1 Cutting speed effect on chip morphology

The SDEG distribution in the shear zone is shown in Fig. 3.10 with increasing cutting speed, hereinto the value above 0.74 directly indicates the crack possibility, as mentioned in previous section, which is also one reason for segmented chip generation, as described in [LI02], among other phenomena. When the cutting speed is equal to 60 m/min, the chip presents a continuous part and a segmented one. Nonetheless, the region with the value of SDEG above 0.74 is just a small zone beneath the free surface of the cutting material ahead of the tool tip. When the cutting speed increases to 120 m/min, the segmentation takes place on the entire chip, and part of the region with the value of SDEG above 0.74 passes through half of the chip. When the cutting speed increases to 180 m/min, the regions with the value of SDEG above 0.74 nearly arrive at the free surface around the tool tip for all segmentations. So, the higher cutting speed, the higher chip segmentation is.

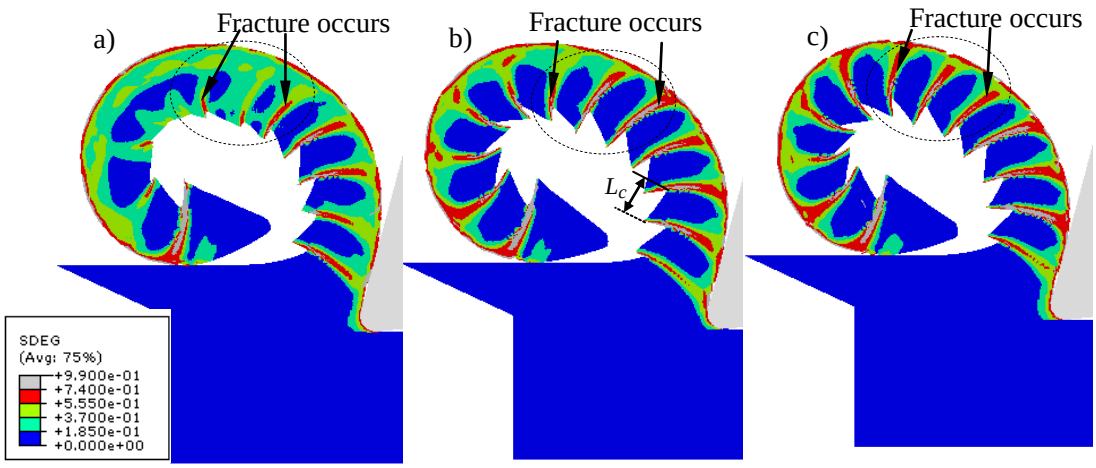

Fig. 3.10 SDEG distribution in chip according to V_c variation for μ = 0.7 and f = 0.127 mm/rev: a) V_c = 60 m/min, b) V_c = 120 m/min, c) V_c = 180 m/min.

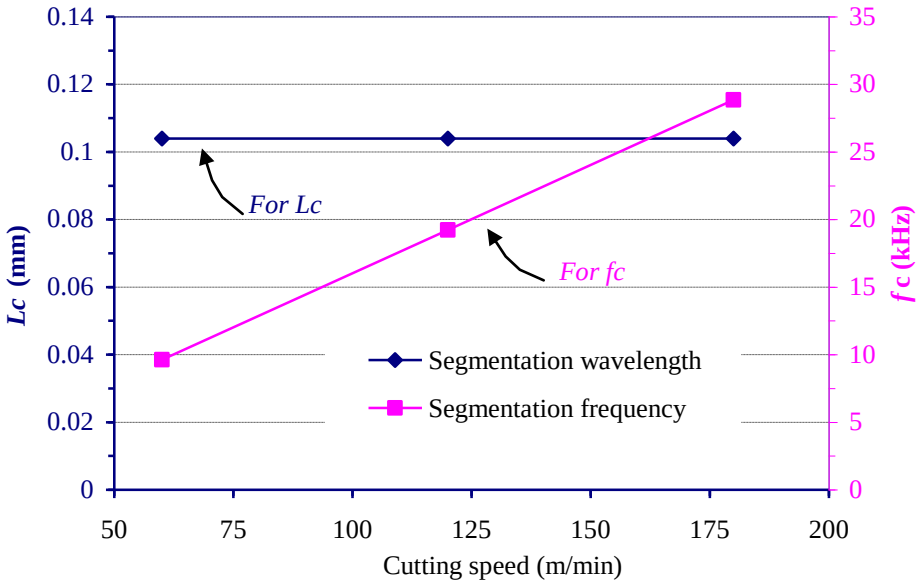

Fig. 3.11 Effect of V_c on Lc and f_c for f = 0.127mm, and μ = 0.7.

The segmentation frequency f_c can be approximated by the ratio V_c / L_c, where L_c is the chip segmentation wavelength as indicated in Fig. 3.7 (b) [SUN09a, BAR01].

$$f_c = \frac{V_c}{L_c} \tag{3.23}$$

The computed chip segmentation wavelengths, for cutting speeds of 60, 120, and 180 m/min (as shown in Fig. 3.11) are constant, whereas the segmentation frequency is directly proportional to the cutting speed according to Eq. 3.23. This result agrees well with the experimental study carried out by Sun [SUN09a].

3.3.2 CoF effect on chip morphology

To study the influence of the CoF for the cutting of Ti–6Al–4V, friction values were taken equal to 0.3, 0.7 and 1 at the tool-chip interfaces. The CoF for the sacrificial passage zone (see Fig. 2.2, Part 3) is taken constant. As shown in Fig. 3.12, the temperature distribution on chip and tool is greatly influenced by the CoF variation. It is remarked that the insert-zone where the temperature ranges from 581 to 720ºC migrates from the tool-tip to the rake face-chip contact end, when CoF varies from 0.3 to 1.

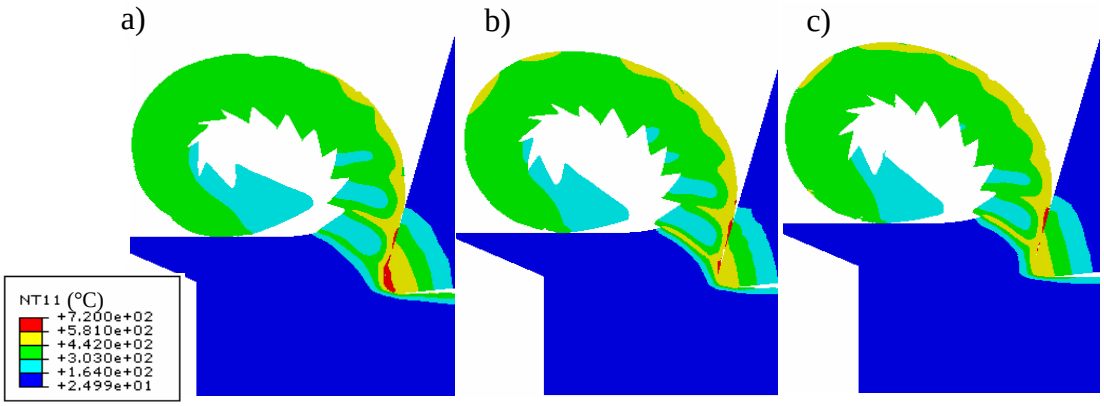

Fig. 3.12 Temperature distribution (°C) with increasing μ for f = 0.127mm/rev, V_c = 120 m/min: a) μ = 0.3, b) μ = 0.7 c) μ = 1

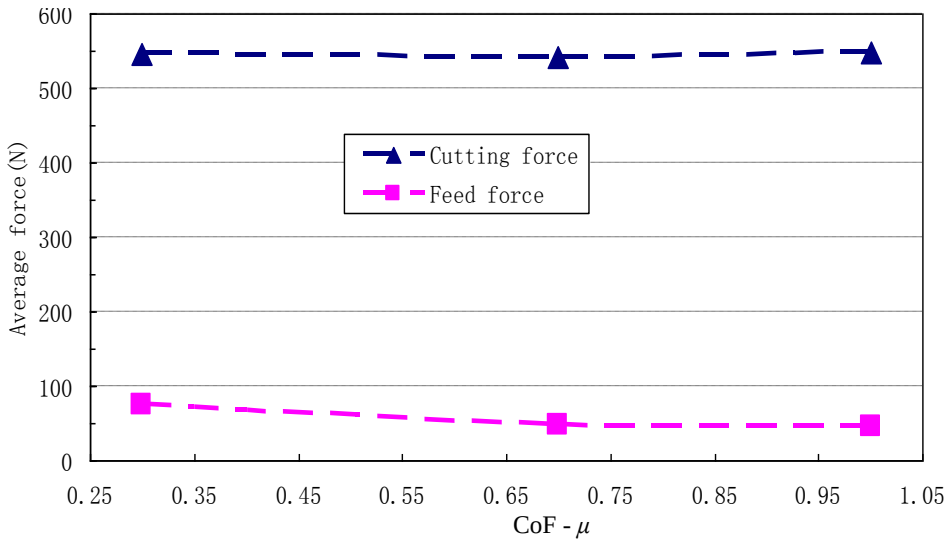

Fig. 3.13 Evolution of the average cutting and feed forces versus CoF for f = 0.127 mm/rev, and V_c = 120m/min

Moreover, it is noted the little influence of the CoF on cutting force which has an average value around 540 N, as illustrated in Fig. 3.13. This result can be expected because the global chip morphology remains almost the same whatever the CoF is. The main reason is that more energy will be converted into heat when increasing the friction coefficient, as illustrated in

Fig. 3.12. This will induce a thermal softening in both sides of the machined material (at tool-chip and tool-machined surfaces). The limiting shear stress decreases with temperature as shown in Fig. 2.8 producing shear bands that coincide with zones where high temperatures are found. It also explains why the cutting force tends to decrease when increasing the friction coefficient. For the same reason, the feed force decreases when CoF increases from 0.3 to 1. Similar trends have been observed by Filice et al. [FIL07] and Calamaz et al. [CAL07].

3.3.3 Rake angle effect on chip morphology

Two feed rates of 0.06 and 0.1 mm/rev were checked to study the effect of the rake angle effect on the chip morphology. According to Fig. 3.14, it can be concluded that when passing from positive to negative angle the chip segmentation phenomenon becomes more pronounced.

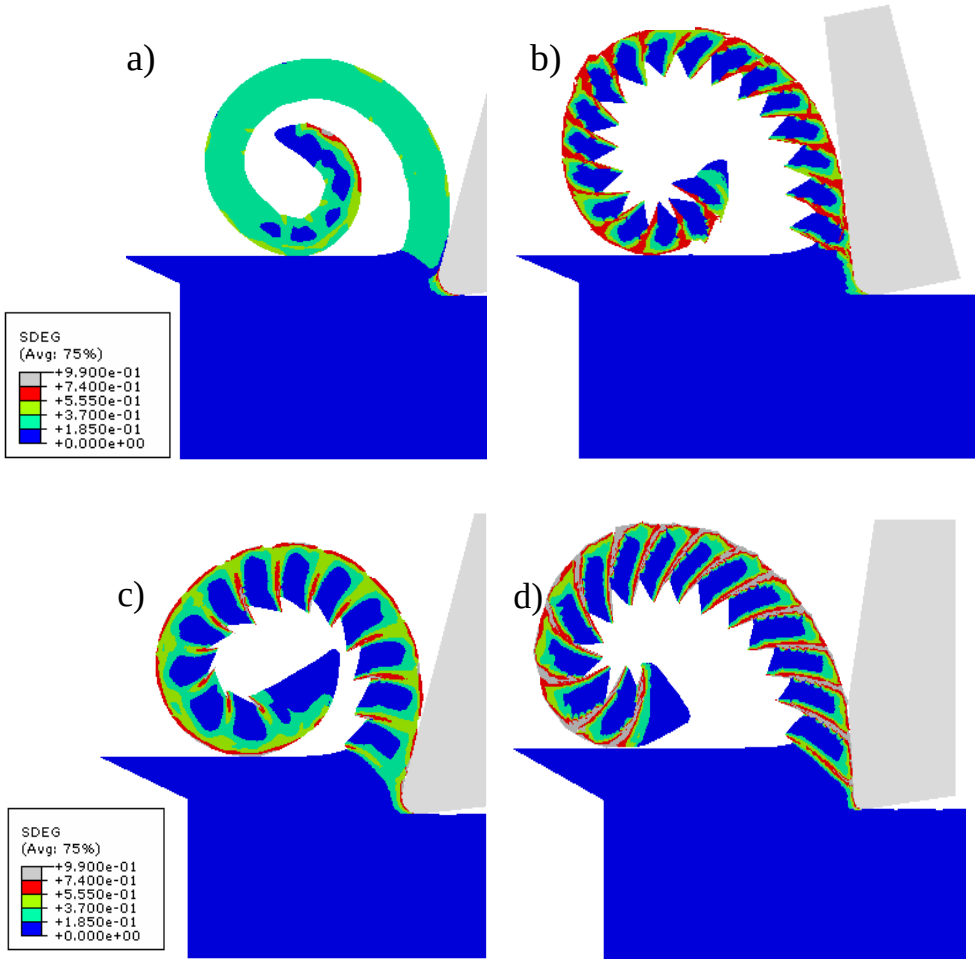

Fig. 3.14 Chip SDEG distribution at V_c = 120 m/min and μ = 0.7: a) γ_0 = 15°, f = 0.06 mm/rev b) γ_0 = -6°, f = 0.06 mm/rev c) γ_0 = 15°, f = 0.1 mm/rev d) γ_0 = -4°, f = 0.1 mm/rev

For the same tool-rake angle, the increase of the feed rate from 0.06 to 0.1 mm/rev implies more chip segmentation. This can be observed when comparing Fig. 3.14 (a) and Fig. 3.14 (c). So, the higher the feed rate, the higher the material SDEG as it is also shown in Fig. 3.14 (b) and (d) (see the propagation of SDEG between 0.74 and 1), which maybe due to heat conduction effect among others: with larger feed rate, the heat conditions in the chip tend to be more adiabatic, then more heat will be limited in the localized shear bands. This will accelerate the material stiffness degradation process and lead to more segmented chip. It can be also underlined that the more is the negative rake angle, the higher is the tool-workpiece contact pressure and so the chip segmentation.

3.3.4 Residual stress (RS) distribution based on macro model

Surface integrity refers to studies of surface topography and geometry, and subsurface physical and chemical characteristics such as composition, microstructure, phases, residual stresses (RS), hardness, cracking, and embitterment among other effects due to machining or another surface operation [MUR04].

For the cutting operation, the quality of the cut surface is controlled by finishing operation leading to the generation of surface that contain geometric deviation (deviation from ideal geometric) and metallurgical damage which differs from the bulk material. The geometrical deviation refer to various forms of deviation such as roughness, straightness etc. Types of metallurgical surface damage that produced during machining include micro-crack, micro-pits, tearing, plastic deformation of the feed marks, re-deposited materials etc. Its therefore, control of the machining process to produce components of acceptable integrity is essential. [EZU03]. So, the surface integrity is the result of the entire environment accompanying cutting [FIE73].

When critical and expensive structural components in aerospace industry are machined with the objective to reach high reliability levels, surface integrity is one of the most relevant parameters used for evaluating the quality of machined surface.

To evaluate surface integrity, many techniques can be used as it mentioned in the reviews published by Field et al. [FIE72], and Brinksmeier [BRI89]. These authors have described some of the experimental approaches to evaluate surface integrity such as optical and electronic microscopy, x- ray in both diffraction and the fluorescent mode, ultrasound used in scanning acoustic microscopy to give information on the physical or even chemical nature of superficial layers, Raman spectroscopy for studying superficial structures, chemical composition and stresses in crystalline and amorphous materials, instrumented micro

indentation for evaluating mechanical material properties like hardness and Young's modulus, and photo thermal microscopy for the non-destructive testing of the local thermal properties of materials among others.

As the RS is one among the most important factors to determine the surface integrity, it is considered as the highlighted part in the present section study corresponding to the machining of the Titanium alloy Ti–6Al–4V. As it is known, the final surface obtained after finishing was the subject of successive cutting sequence. Consequently, the RS distribution can be affected. From numerical point of view, the physical state from the first cut is saved and used as initial condition for the second one. Other cutting conditions of the second cut are the same as those of the first cut. As concerned ABAQUS procedure, the cutting operation is calculated in the ABAQUS Explicit module, and the subsequent external load relaxation process is performed in ABAQUS Implicit module. Wherein, three unloading steps were implemented at the end of each cut in this study: (1) Release the cutting forces, (2) release the clamping forces, and (3) release the workpiece to room temperature. The detailed description of the pre-cited procedure employed to simulate RS is resumed in Fig. 3.15.

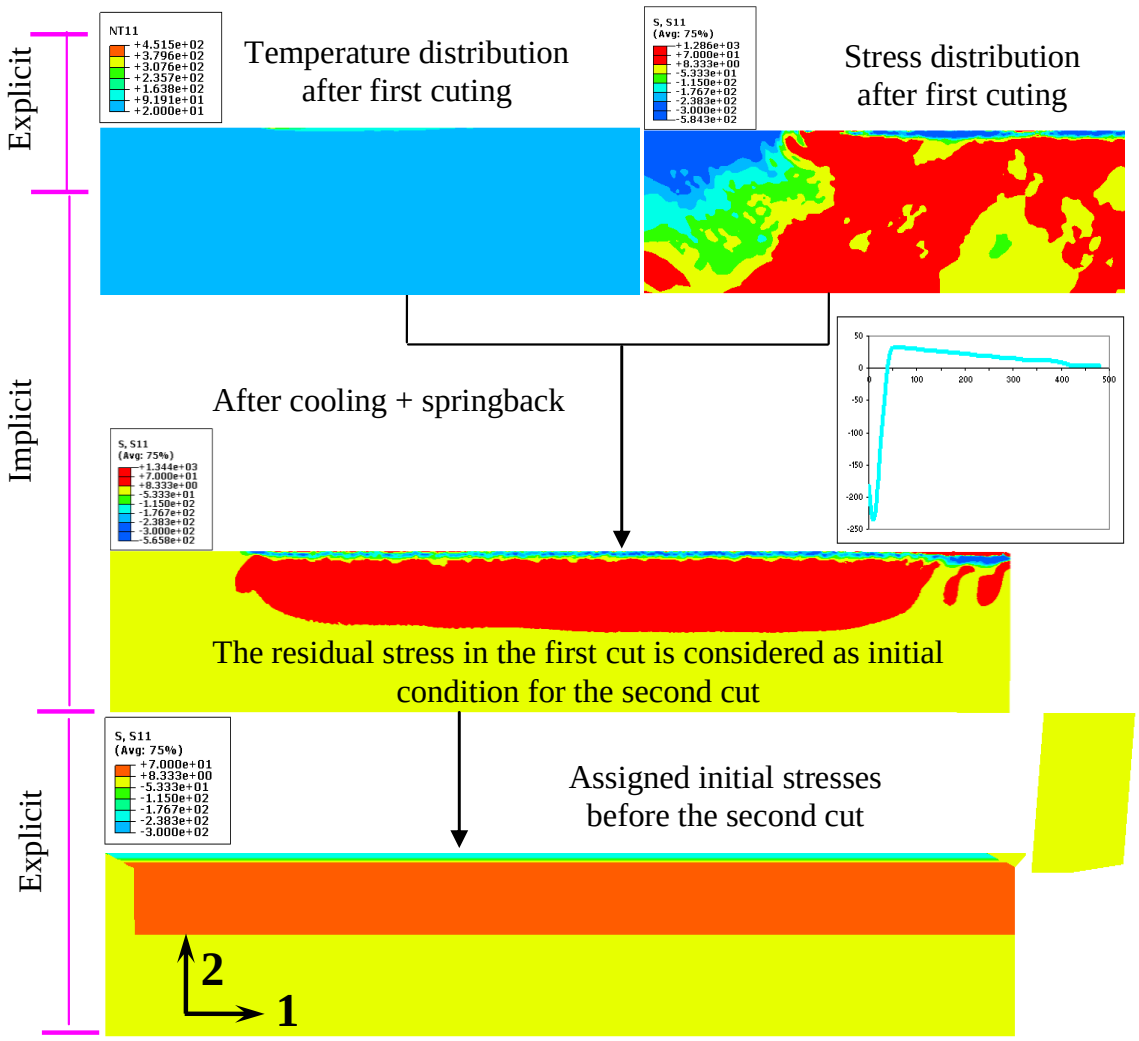

Fig. 3.15 External load relaxation process

After external force release and cooling down to room temperature, the final RS distribution on the workpiece is shown in Fig. 3.16. The stresses in Region II are selected to evaluate the RS, and the predicted RS are extracted from element integration point. Consequently, the stress on the machined surface is located at the centre of the first layer element (4 μm below the machined surface) Fig. 3.16, and the stresses are averaged along 2-3 mm in the circumferential direction (X-axis) after their calculation in element integration points.

Moreover, it is remarked that the oscillated RS caused by the segmented chip are observed on the machined surface (the magnified zone in Fig. 3.16), which shows the same oscillation frequency as that of chip segmentation. So, it is very important to study the chip formation process which can directly determine the RS distribution and especially the local one.

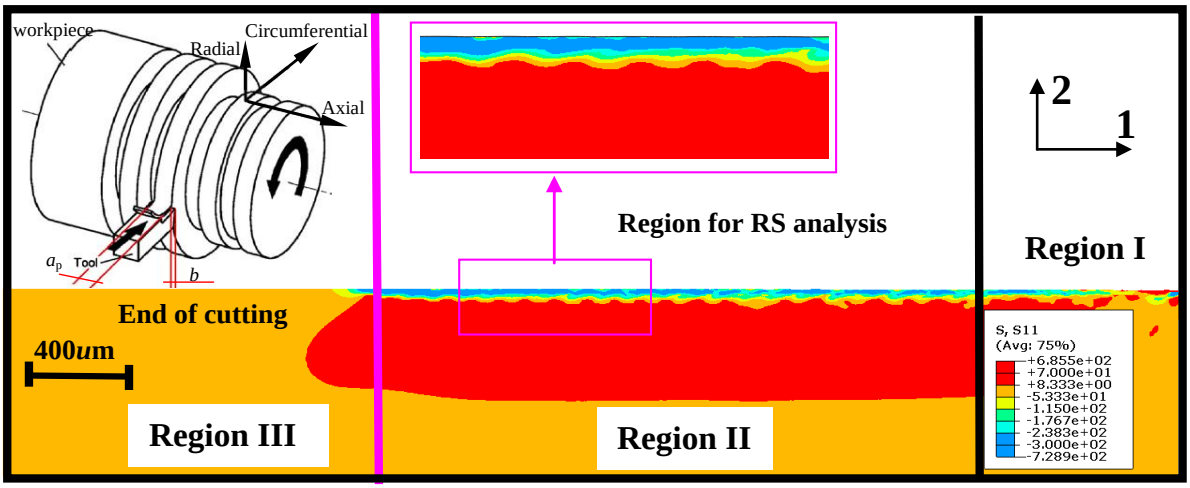

Fig. 3.16 RS distribution on the workpiece

In order to evaluate the pertinence degree level of our model we have ask Professor Hamdi from ENISE de St Etienne for carrying out the measurements of RS but unfortunately the measurements were very different from the technical point of view. This is related to the presence of two phases α and β. For that, we have followed the one group experiment carried out by Chen et al. [CHE04] who have studied the influence of tool flank wear on the RS distributions. Besides, this simulation results are compared with these performed with DEFORM from the research group of Professor Umbrello [ZHA11]. The cutting parameters adopted are listed in Table 3.7.

Cutting parameters	Chen et al. [CHE04]	
	I	II
Cutting speed (*Vc*), m/min	320	320
Uncut chip thickness, mm	0.1	0.1
Depth of cut, mm	1	1
Cutting edge radius, µm	sharp	sharp
Rake angle, deg	5	5
Clearance angle, deg	8	8
Flank wear, mm	0.03	0.2

Table 3.7 Process parameters employed in the study

To analyze the influence of tool wear on RS distribution beneath the machined surface the flank wear size of cutting tool were considered as an initial state and kept constant during the cutting simulation. The tools' geometry shapes with flank wear are illustrated in Fig. 3.17.

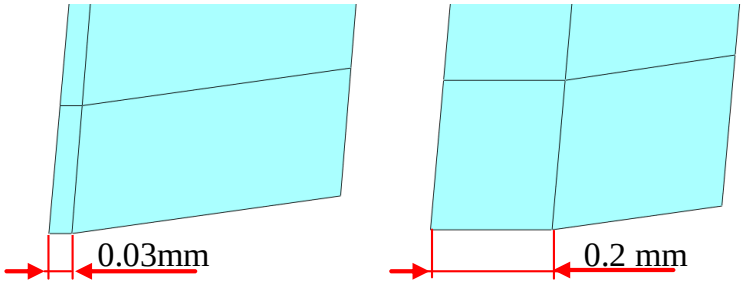

Fig. 3.17 Tool shapes with flank wear.

Fig. 3.18 shows the effect of flank wear length on residual stress distribution beneath the newly machined surface, the acquired experimental ones are also detailed from literature (Liu and Guo, [LIU00]). As general trends, both the software highlight that when the flank wear was increased from 0.03 mm to 0.2 mm, the surface residual stress towards the tensile region. This is due to the higher magnitude of temperature generated along flank face/workpiece interface.

Moreover, both DEFORM and ABAQUS show that the maximum compressive residual stress as well as the beneficial depth decreases with increasing of flank wear. In addition, the distance where maximum compressive residual stress is located seems to be not affected by flank wear. However, both the software show some gap between experiments and simulations when considering the influence of first cut. The reason of such discrepancy should be related to firstly the material flow stresses used in both ABAQUS and DEFORM which are not suitable to describe pertinently material states. Secondly, It is worth to point out that in both computations, the residual stresses due to phase transformation were neglected and, especially in the case of DEFORM (temperature near to phase transformation effect), such assumption is not properly corrected.

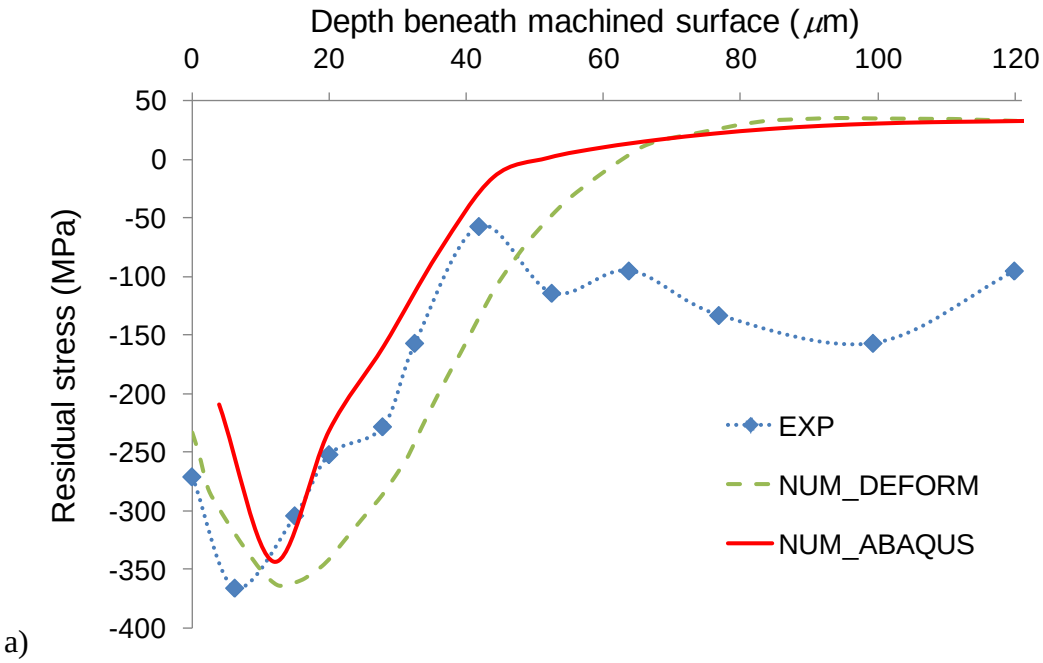

a)

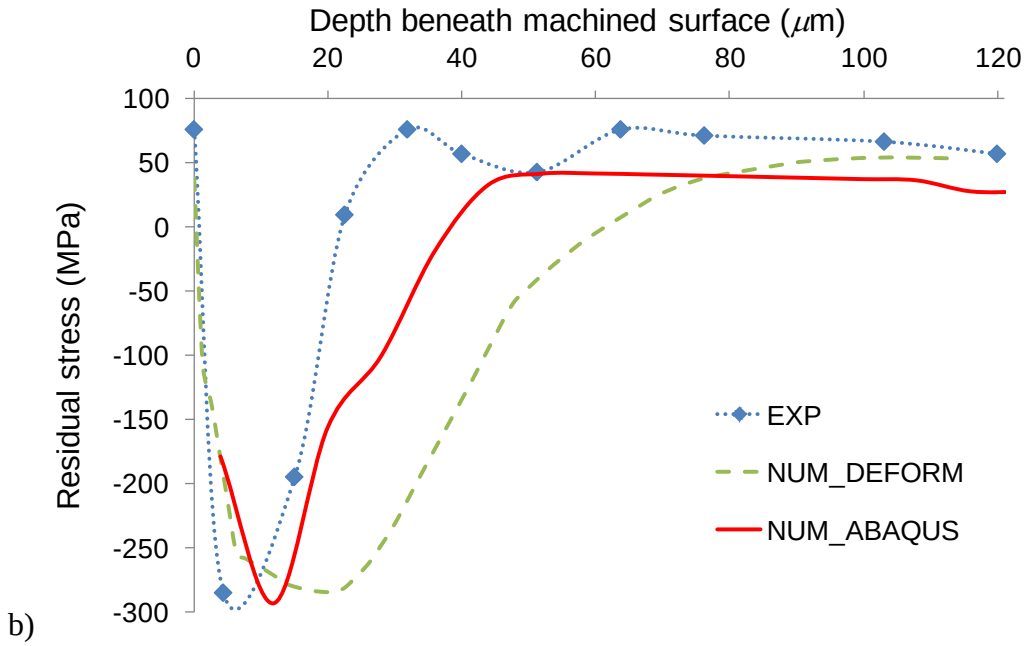

b)

Fig. 3.18 Effect of the flank wear lengths on circumferential residual stress profile with Vc = 320 m/min: a) VB = 0.03 mm; b) VB = 0.2 mm.

In addition, the distance where maximum compressive residual stress is located seems to be not affected by flank wear, and the compressive stress depths are less than 50 μm for both simulation and experimental results, these values are just approximate two or three layer grains.

3.4 Concluding remarks

With the new cutting model developed, a parametric study was carried out and compared with experimental results to qualify the pertinence degree of such model. It is shown an interesting agreement between our numerical results and both our experimental tests and those from literatures. This allowed bringing some physical insights accompanying the chip formation according to the variation of the cutting speed, the CoF, and the rake angle. The simulation results show that the higher is the cutting speed, the more marked is the chip segmentation phenomenon.

- A refined measure of the computed chip segmentation wavelengths shows that they are constant regarding to cutting speed variation, whereas chip segmentation frequency is directly proportional to it. Moreover, the chip segmentation is also more pronounced when the insert geometry passes from positive to negative rake angle.

- Generally speaking, the chip will be more segmented with increased cutting speed and feed rate, and it should be marked that the influence of feed rate is more obvious compared with cutting speed.

- When the CoF increases from 0.3 to 1, the highest temperature located in the insert zone migrates from the tool-tip to the rake face-chip contact end. This temperature migration leads to a decrease of the feed force whereas it does not affect the oscillation (amplitude) of the cutting force.

- Also, a numerical approach for the cut surface residual stress distribution was demonstrated and compared to experimental values from literature. We think that approach is interesting and has to be improved in future.

Now, if one ask us if the proposed numerical cutting model is robust and pertinent for the prediction of chip formation and surface integrity in the case of lower feed rate values (less than 0.1 mm/rev) or in the case of micromachining, for example, the response will be of course negative. This is due to mainly the fact that the J-C material behavior model is macroscopic phenomenological one. Meanwhile, it can be also found that the compressive residual stress is limited to the size of 50 μm below the machined surface. So, the traditional cutting model is not enough to study the more detailed information for machining.

For that, in the next chapter, attention is focused to response the pre-cited question by adopting the crystal plasticity theory in order to consider the microstructure of the treated

material during cutting operation. It is question to show the capacities of this theory to capture micro-scale effects and to precise more detailed information of chip formation and machined surface integrities.

4 Towards a material microstructure–level (MML) cutting model

4.1 Introduction

The present chapter focuses on modeling of material microstructure-level cutting model (MML cutting model). The objective is to establish a physical based model that is suitable to simulate MML chip formation process and can efficiently capture microstructure effect during the simulation of the chip formation and the prediction of the surface integrity.

To understand more accurately what happens locally at the tool-workpiece interface, various micro-scale models have been proposed in the literatures [LIU06, SIM06A]. Wherein, Liu et. al [LIU06] studied the material strengthening mechanism accompanying micro-cutting and its influence on the size effect and specific cutting energy evolution. Moreover, ASAD [ASA11] made a systematic study about the influence of the strain gradient during macro to micro-scale milling case. These authors have incorporated the strain gradient into the traditional J-C constitutive law via the elaboration of an user subroutine VUMAT. The specific cutting energy values obtained by numerical simulations using strain gradient based plasticity model were found quite close to the experimental ones through all the cutting speed.

For the cutting simulation considering the microstructure, Chuzhoy [CHU02, CHU03A] have developed a MML cutting model for ductile iron machining and its constituents. These authors have validated their model by carrying out experimental machining tests. Obikawa [OBI09] studied the MML phase-dependent residual stresses in the machined surface layer of two-phase alloys - iron and steel. They found that the microstructure of the workpiece has a great influence on the residual stress distribution. Simoneau et al. [SIM06A, SIM06B] defined micro-scale cutting as the point at which the uncut chip thickness (UCT) was smaller than the

average size of the smallest grain type in the material microstructure, this definition is also used in this thesis.

Nevertheless, the traditional macro plastic models are usually adopted for the microstructure, which limits the capability to observe the material behavior in the microstructure. Recently, the crystal plasticity model is widely used to predict the fretting problems by Goh et al. [GOH06] and Dick and Cailletaud [DIC06], which is typically described by small strain accumulation. While concerning the cutting operation, the crystal plastic model (crystallographic slip scale) for presenting large strain and bonding relationship between grains are not considered.

In this framework, the present contribution focuses on the presentation of an original research work in the aim to bring more comprehension of cutting process at the level of the cut material microstructure. This contribution is based on the exploitation of both crystal plasticity and bonding relationship between grains via the consideration of cohesive elements. For that, a FE modeling approach which explicitly simulates the behavior of heterogeneous crystal plasticity material by considering a grain level model is proposed. The use of this model is demonstrated during the cutting of a Titanium alloys Ti–6Al–4V with a primary α phase.

In the following work, a literature review showing the complexity of the crystal microstructure and mechanical properties of Ti–6Al–4V is presented. After that, the theory of crystal plasticity and some aspects related to cohesive element are discussed. Then, the material cutting model calibration is carried out to identify the model parameters. The numerical model is confronted to experimental data in term of chip morphology. Finally, a numerical example of orthogonal machining of Ti–6Al–4V is discussed, and the parametric studies for chip formation with different orientation angle, cutting speed and feed rate are also shown.

4.2 Elaboration of the material microstructure level cutting model

The numerical model presented here simulates the machining of heterogeneous materials at a microstructure - level. Although the model is applied for the simulation of ductile Titanium alloy Ti–6Al–4V, the proposed algorithm is general enough to be used for many other crystal structure materials. Following the works of Chuzhoy et al. [CHU02], the model consists of three main procedures that are integrated into the elaborated FE cutting model.

- The generation of the geometrical model considering the material microstructure (Presence of specific grain shape).

- The adoption of a polycrystal strategy model.

- The consideration of material flow law as intra-granular and inter-granular coupled their damage models.

More detailed on the specified pre-cited details are described in the following section.

4.2.1 Aspects on the cut material microstructure

The Titanium alloy Ti–6Al–4V alloy has a duplex microstructure, 60% primary alpha nodules α_P phase and 40% lamellar colonies of second alpha and beta phases, $\alpha_S + \beta$ phase [MAL04]. According to [CAS07], the nodules and lamellar colonies have the same size. Lamellar colonies consist of secondary alpha plates α_S with an average thickness of about 500 nm separated by thin β plates (Fig. 4.1). The β plates between two α_S plates are sometimes discontinuous (Fig. 4.1, details A and B) and are a few tens of nanometres thick. Small β grains (about 100 *n*m size) are sometimes present at the grain boundaries between the nodules and lamellar colonies.

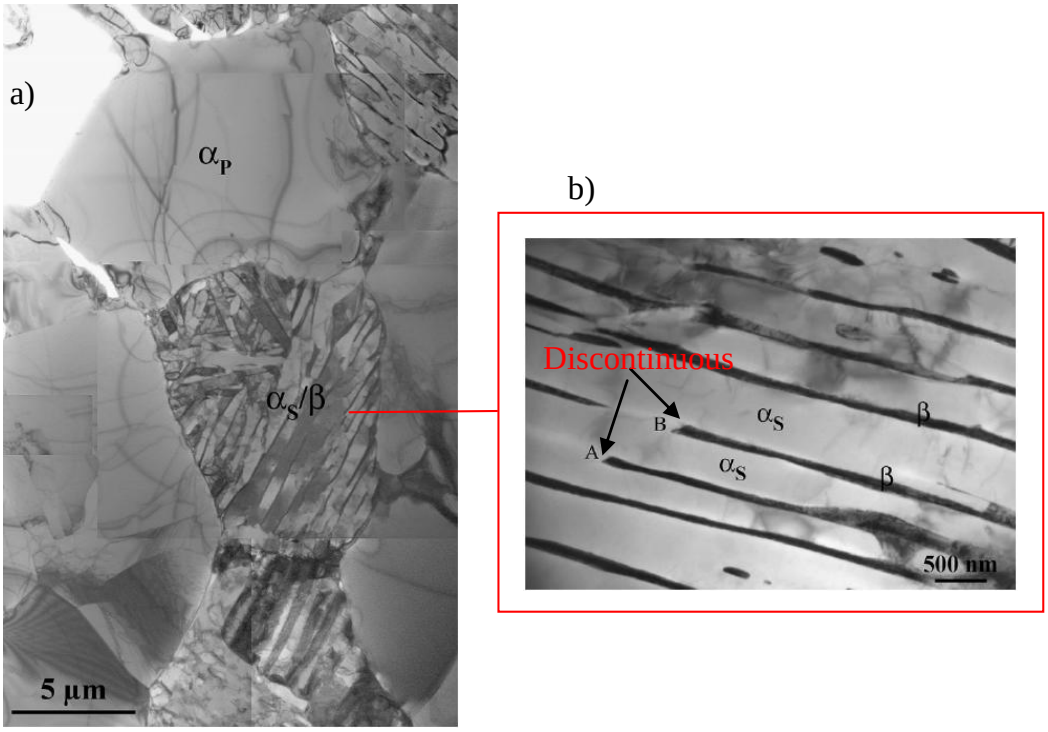

Fig. 4.1 Microstructure of the investigated alloy with primary alpha nodules α_p and lamellar colonies α_s-β. [CAS07]

4.2.1.1 Slip system in primary α phase

For the primary α phase, four different crystallographic slip families (A family consists of the slip systems in the same slip plane with different slip directions) can be mentioned, as it is illustrated in Fig. 4.2, and there are 24 active crystallographic slip systems (CSS) (A system contains a slip plane and a slip direction) included in the model:

a) 3 $<11\bar{2}0>$ {0001} basal CSS

b) 3 $<11\bar{2}0>$ $\{10\bar{1}0\}$ prismatic CSS

c) 6 <**a**> first order pyramidal CSS $<11\bar{2}0>$ $\{10\bar{1}1\}$

d) and 12 <**c+a**> first order pyramidal CSS $<11\bar{2}3>$ $\{10\bar{1}1\}$.

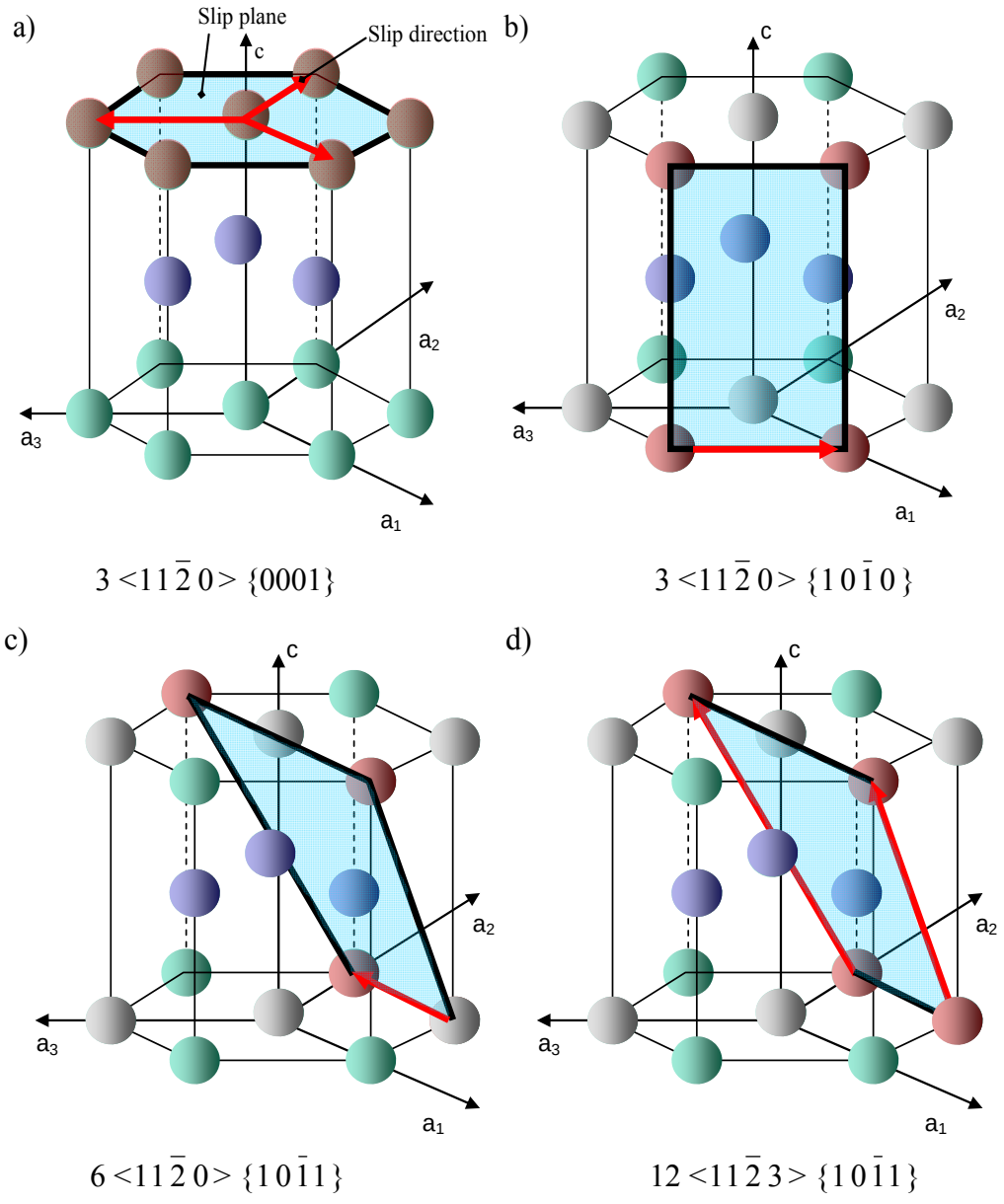

Fig. 4.2 Slip geometries for the primary *α* phase

The dominant slip systems of the primary α_P phase are the basal and prismatic CSS due to their relatively low critical resolved shear stress (CRSS). The slip resistances of the first order pyramidal slip systems are about twice those of the basal and prismatic slip ones. The <**c+a**> first order pyramidal systems have the highest CRSS of all slip systems, which is ignored and therefore not activated in the proposed cutting model.

4.2.1.2 Slip system in secondary α_s + β lamellar phase

While the α_s-β colony contains secondary α and β phases arranged in lamellar structure. The thicknesses of the secondary α and β phase range from hundreds of nanometers to several microns. It is extremely difficult to explicitly model such small structures using a finite element mesh that must include a large number of grains. Thus, the α_s-β lamellar colony is homogenized by considering the crystallographic relationships between the secondary α and β laths given by $(0001)_\alpha \,||\, \{110\}_\beta$ and $\langle 11\bar{2}0\rangle_\alpha \,||\, \langle 111\rangle_\beta$ [ANK80, BRO03], as shown in Fig. 4.3.

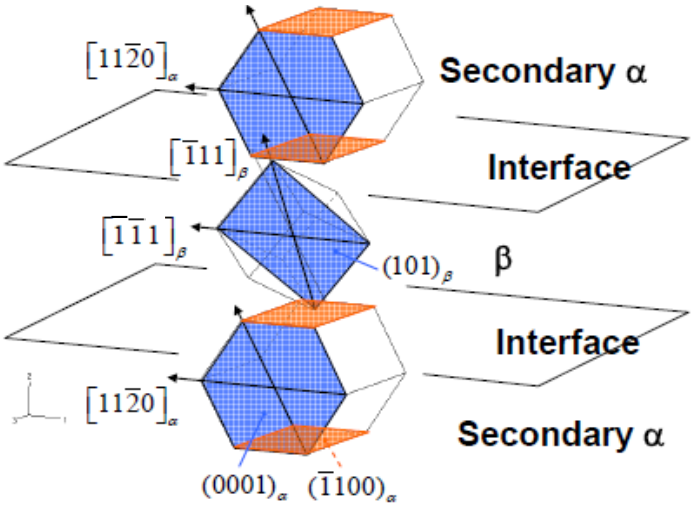

Fig. 4.3 Lamellar Burgers orientation relationships (BOR) [ZHA08]

Follow the method of Mayeur [MAY07], who proposed a model for the α_s-β colonies by homogenizing the lamellar structure with 24 possible slip systems: (a) 3 $<11\bar{2}0>$ {0001} basal CSS (b) 3 $<11\bar{2}0>$ $\{10\bar{1}0\}$ prismatic CSS (c) 6 <a> first order pyramidal CSS $<11\bar{2}0>\{10\bar{1}1\}$, and 12 <111> {110} BCC CSS, as illustrated in Fig. 4.4.

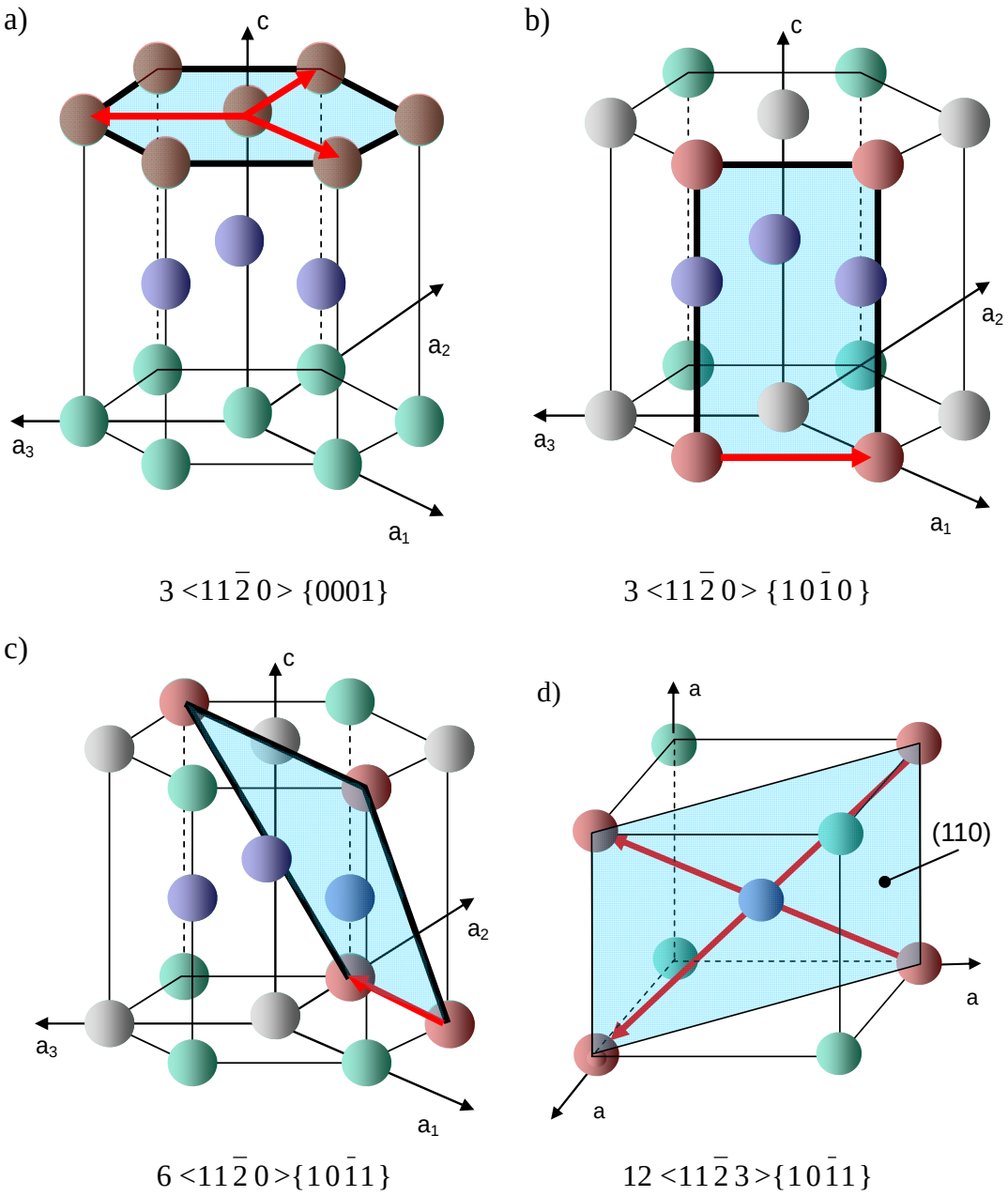

Fig. 4.4 slip geometry for equivalent representation of HCP α_s and BCC β phase.

Prior to assigning grain orientation, the bcc slip systems are transformed into the hexagonal coordinate system according to the Burgers orientation relation (BOR). The slip systems that either glide parallel to the α_s-β interface or have parallel slip planes in both the α and β phases are considered as the soft deformation modes. The set of soft deformation modes consists of 3 basal, 1 prismatic, and 2 <111> {110} BCC slip systems.

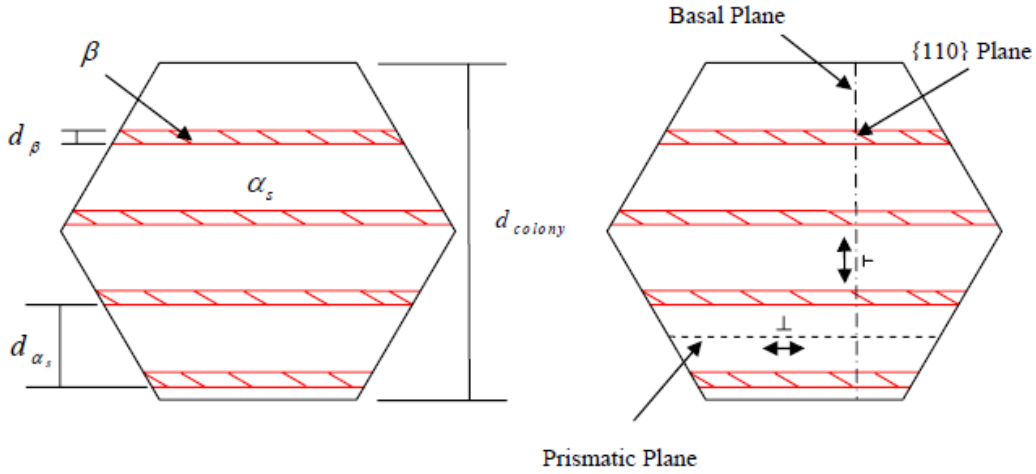

Fig. 4.5 Lamellar colony length scales (left) and soft deformation modes (right) [MAY07]

Within the set of soft deformation modes assumed in this model, dislocations on the prismatic system glide parallel to the α_s-β interface, whereas the basal and close packed BCC planes are parallel and dislocations sliding in these planes are effectively able to transmit and traverse the length of the lamellar colony, as shown in Fig. 4.5. The hard modes of deformation correspond to the slip systems for which dislocations cannot transmit through the interface, therefore leading to high CRSS for these systems due to net residual dislocation density at the α_s-β interfaces.

The detailed slip systems are given in Table 4.1 for primary α phase, but they are presented by the Miller-Bravais indices by four axes, which need to be transferred to orthogonal Cartesian coordinate system.

For the lamellar colonies α_s-β, the slip systems for secondary α phase, which is the same as the condition of primary α phase, are not revisited again, while for the slip systems of β phase, which need to be transferred to grain local Cartesian coordinate first with Euler angle transformation before texture operation, are given in Table 4.2.

		Slip systems for primary α- phase					
Basal (3)	Slip system	{0001} <11$\bar{2}$0>					
	Plane	(0001)					
	Direction	[2$\bar{1}\bar{1}$0] (1)	[$\bar{1}$2$\bar{1}$0] (2)	[$\bar{1}\bar{1}$20] (3)			
Prismatic (3)	Slip system	{10$\bar{1}$0} <11$\bar{2}$0>					
	Plane	(0$\bar{1}$1 0)(1)	(10$\bar{1}$ 0)(2)	($\bar{1}$100)(3)			
	Direction	[2$\bar{1}\bar{1}$0]	[$\bar{1}$2$\bar{1}$0]	[$\bar{1}\bar{1}$20]			
First order pyramidal (6)	Slip system	<a> {10$\bar{1}$1} <11$\bar{2}$0>					
	Slip Plane	(0$\bar{1}$1 1)	(1$\bar{1}$0 1)	(10$\bar{1}$1)	(01$\bar{1}$1)	($\bar{1}$101)	($\bar{1}$011)
	Slip Direction	[2$\bar{1}\bar{1}$0]	[11$\bar{2}$0]	[$\bar{1}$2$\bar{1}$0]	[$\bar{2}$110]	[$\bar{1}\bar{1}$20]	[1$\bar{2}$10]
First order pyramidal (12)	Slip system	<c+a> {10$\bar{1}$1} <11$\bar{2}$3>					
	Slip Plane	(0$\bar{1}$11)	(0$\bar{1}$11)	(1$\bar{1}$0 1)	(1$\bar{1}$0 1)	(10$\bar{1}$1)	(10$\bar{1}$1)
	Slip Direction	[11$\bar{2}$3]	[$\bar{1}$2$\bar{1}$3]	[$\bar{1}$2$\bar{1}$3]	[$\bar{2}$113]	[$\bar{1}\bar{1}$23]	[$\bar{2}$113]
	Slip Plane	(01$\bar{1}$1)	(01$\bar{1}$1)	($\bar{1}$101)	($\bar{1}$101)	($\bar{1}$011)	($\bar{1}$011)
	Slip Direction	[1$\bar{2}$13]	[$\bar{1}\bar{1}$23]	[2$\bar{1}\bar{1}$3]	[1$\bar{2}$13]	[2$\bar{1}\bar{1}$3]	[11$\bar{2}$3]

Table 4.1 Possible slip systems in HCP primary *α* phase

From Fig. 4.3, it can be seen that slip systems in BCC crystal should be transferred into HCP crystal with below Euler angles:

$\phi = 45^{\circ}; \varphi_1 = \pi + \arcsin(\sqrt{2/3}), \sin(\varphi_1) = -\sqrt{2/3}, \cos\varphi_1 = -\sqrt{1/3}; \varphi_2 = \pi/2$

Slip systems	In BCC coordinate	For Cartesian coordinate in HCP crystal
$\langle 111\rangle\{110\}$	$[\bar{1}11]$ (101)	$\left[\frac{\bar{1}}{3}\ \frac{2\sqrt{2}}{3}\ 0\right]$ (001)
	$[\bar{1}\bar{1}1]$ (101)	$[\bar{1}00]$ (001)
	$[111]$ (10$\bar{1}$)	$\left[\frac{1}{3}\ \frac{\sqrt{2}}{3}\ \frac{\sqrt{6}}{3}\right]$ $(\frac{\sqrt{6}}{3}\ \frac{\overline{\sqrt{12}}}{6}\ 0)$
	$[1\bar{1}1]$ (10$\bar{1}$)	$\left[\frac{\bar{1}}{3}\ \frac{\overline{\sqrt{2}}}{3}\ \frac{\sqrt{6}}{3}\right]$ $(\frac{\sqrt{6}}{3}\ \frac{\overline{\sqrt{12}}}{6}\ 0)$
	$[\bar{1}11]$ (110)	$\left[\frac{\bar{1}}{3}\ \frac{2\sqrt{2}}{3}\ 0\right]$ $(\frac{\sqrt{6}}{3}\ \frac{\sqrt{3}}{6}\ \frac{1}{2})$
	$[\bar{1}1\bar{1}]$ (110)	$\left[\frac{1}{3}\ \frac{\sqrt{2}}{3}\ \frac{\overline{\sqrt{6}}}{3}\right]$ $(\frac{\sqrt{6}}{3}\ \frac{\sqrt{3}}{6}\ \frac{1}{2})$
	$[\bar{1}\bar{1}1]$ ($\bar{1}$10)	$[\bar{1}00]$ $(0\ \frac{\sqrt{3}}{2}\ \frac{\bar{1}}{2})$
	$[\bar{1}\bar{1}\bar{1}]$ ($\bar{1}$10)	$\left[\frac{\bar{1}}{3}\ \frac{\overline{\sqrt{2}}}{3}\ \frac{\overline{\sqrt{6}}}{3}\right]$ $(0\ \frac{\sqrt{3}}{2}\ \frac{\bar{1}}{2})$
	$[\bar{1}\bar{1}1]$ (011)	$[\bar{1}00]$ $(0\ \frac{\sqrt{3}}{2}\ \frac{1}{2})$
	$[\bar{1}1\bar{1}]$ (011)	$\left[\frac{1}{3}\ \frac{\sqrt{2}}{3}\ \frac{\overline{\sqrt{6}}}{3}\right]$ $(0\ \frac{\sqrt{3}}{2}\ \frac{1}{2})$
	$[\bar{1}11]$ (01$\bar{1}$)	$\left[\frac{\bar{1}}{3}\ \frac{2\sqrt{2}}{3}\ 0\right]$ $(\frac{\sqrt{6}}{3}\ \frac{\sqrt{3}}{6}\ \frac{\bar{1}}{2})$
	$[\bar{1}\bar{1}\bar{1}]$ (01$\bar{1}$)	$\left[\frac{\bar{1}}{3}\ \frac{\overline{\sqrt{2}}}{3}\ \frac{\overline{\sqrt{6}}}{3}\right]$ $(\frac{\sqrt{6}}{3}\ \frac{\sqrt{3}}{6}\ \frac{\bar{1}}{2})$

Table 4.2 Possible slip systems in BCC crystal

Parameter	Length(μm)
$d^{\alpha p}$	30
$d^{\alpha s}$	1.5
d^{β}	0.5
D^{colony}	30

Table 4.3 Characteristic length scales used to define slip system threshold stresses.

4.2.2 Polycrystal strategy based cutting model

For the present metallic material Ti–6Al–4V, the Representative Volume Element (REV), in the continuum sense, is highly heterogeneous aggregate of differently orientated grains. Each grain, taken as a single crystal, contains some CSS, potentially activated under the effect of the loading path applied to the overall aggregate at macroscopic level. This CSS activation under the effect of the dislocation movement defines the origin of the plastic deformation as it was mentioned by the pioneering book by Mura [MUR87].

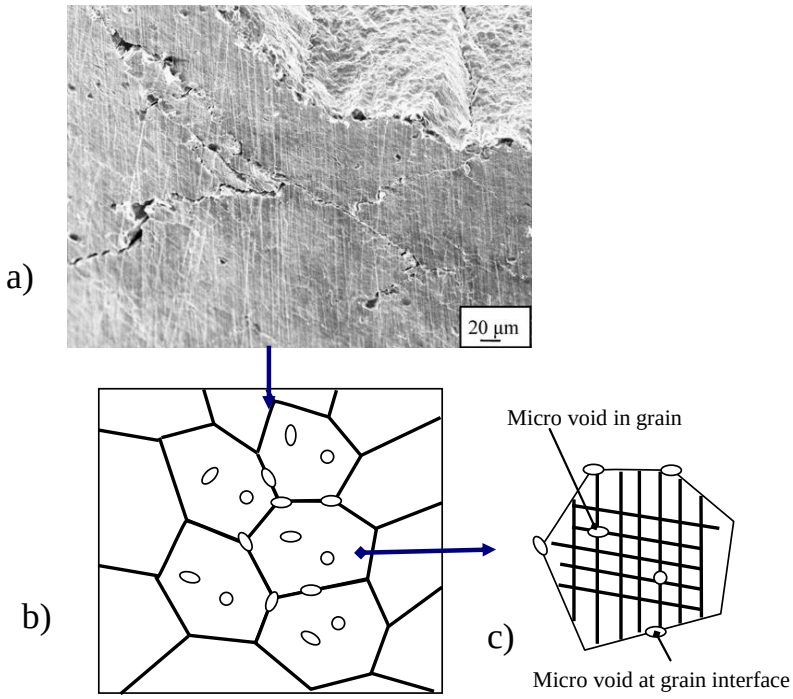

Fig. 4.6 Schematic representation of the microstructure and failure mechanisms

Similar to the work of Boudifa [BOU09], the schematic description of the main ductile damage micro mechanisms adopted in this work is presented in Fig. 4.6. The ductile fracture surface of the Titanium alloy Ti–6Al–4V is represented in Fig. 4.6 a) [PRA11]. Fig. 4.6 b) defines schematically the representation of some grains of the aggregate containing some

micro voids distributed inside the grains (intra-granular inclusions) as well as along the grain boundaries (inter-granular in defects). Fig. 4.6 c) represents an isolated grain with its overall inter-granular and intra-granular defects where some favourably oriented CSS are activated.

The simplified model to deal with above two damage behaviors with a polycrystal strategy is detailed introduced in the following two sub-sections.

4.2.2.1 Intra-granular characteristics

It is important to underline that an arrangement structure of the lamellar colonies α_s-β is relative complex, and consequently it is difficult to model α_s and β phases. For that, only primary α phase is considered to simplify the model of microstructure. The model for a HCP single crystal, (Fig. 4.7 a)) is described within a crystal configuration denoted by the individual grain orientation. It is specified, for a given grain, via three Euler angles (Fig. 4.7 b)), which give the relationship between the local crystal coordinate system (the orthogonal system [100]-[010]-[001], X', Y', Z') of each grain with respect to a fixed specimen coordinate system (e.g. FE model in global coordinate system, X, Y, Z). A polycrystal aggregate is constructed by implementing the different Euler angles for each grain through the user routine (VUMAT) within the explicit FE code ABAQUS.

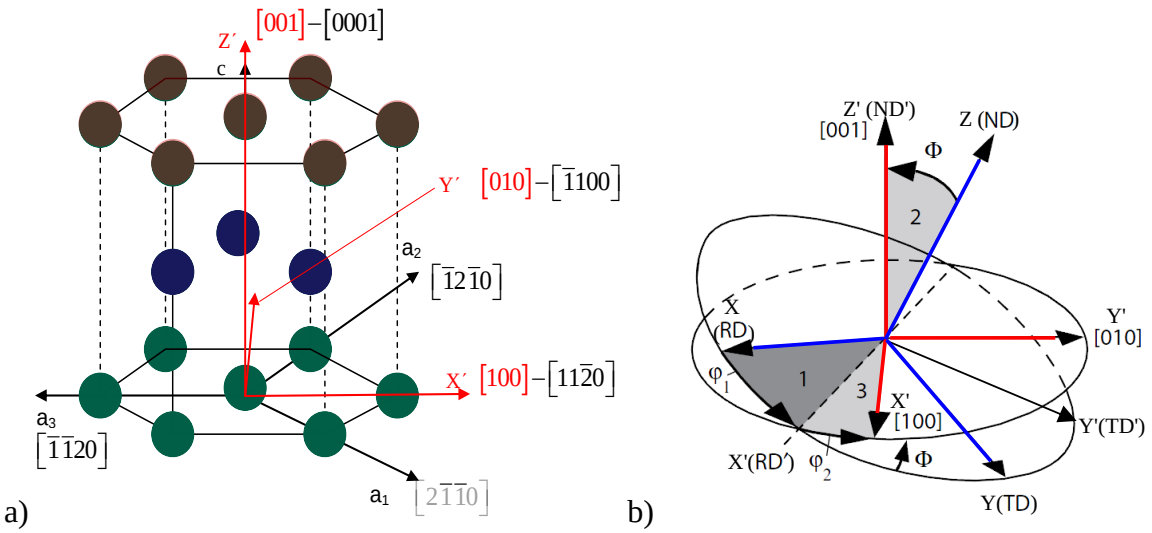

Fig. 4.7. a) Coordinate relationship between the Cartesian system and the Miller-Bravais system [MAY07], b) Rotation through the Euler angles φ_1, Φ, φ_2, in order 1, 2, 3 [RAN09].

The set of Euler angles for each grain in the polycrystal comprises the orientation distribution function (ODF or texture) and can be quantitatively represented by basal plane pole figures,

i.e., (0001) pole figures. The angle definition as given by Randle and Engler [RAN09] is listed below. It is noted that in this convention, the specimen coordinate system is transformed to the local one (Fig. 4.7 b)):

- φ_1 about the normal direction ND (Z-axis), transforming the transverse direction TD (Y-axis) into TD' (Y') and the rolling direction RD(X-axis) into RD' (X').
- Φ about the axis RD' (in its new orientation).
- φ_2 about ND' (in its new orientation).

The rotation through φ_1 about the ND brings RD into the crystal XY-plane. Then by rotating through Φ about RD', the RD becomes coincident with the crystal Z-axis. In order to complete the transformation, it is necessary to accomplish the final rotation through φ_2 about ND' in the aim to align RD' with the crystal X-axis. These three successive rotations can then be easily combined to give the total transformation matrix relating the specimen coordinate system to the crystal coordinate system. The relationship between the two coordinate systems can be written in the form adopted by Randle and Engler [RAN09]:

$$\mathbf{C}_c = \mathbf{g}.\mathbf{C}_s \tag{4.1}$$

Where $\mathbf{C}_c$ is the matrix of the base vectors representing the crystal coordinate system, $\mathbf{C}_s$ is the matrix of the base vectors representing the specimen coordinate system, and $\mathbf{g}$ is the transformation matrix relating the two coordinate systems. The transformation matrix $\mathbf{g}$ is then given as the product of the three successive rotations as

$$\mathbf{g} = \mathbf{g}_{\varphi_2}.\mathbf{g}_{\Phi}\mathbf{g}_{\varphi_1} \tag{4.2}$$

Where

$$\left[\mathbf{g}_{\varphi_2}\right] = \begin{bmatrix} \cos\varphi_2 & \sin\varphi_2 & 0 \\ -\sin\varphi_2 & \cos\varphi_2 & 0 \\ 0 & 0 & 1 \end{bmatrix}, \left[\mathbf{g}_{\Phi}\right] = \begin{bmatrix} 1 & 0 & 0 \\ 0 & \cos\Phi & \sin\Phi \\ 0 & -\sin\Phi & \cos\Phi \end{bmatrix}$$

$$\left[\mathbf{g}_{\varphi_1}\right] = \begin{bmatrix} \cos\varphi_1 & \sin\varphi_1 & 0 \\ -\sin\varphi_1 & \cos\varphi_1 & 0 \\ 0 & 0 & 1 \end{bmatrix}$$

And the subscripts of the transformation matrix $\mathbf{g}$ mean that the matrix is related to the corresponding Euler angles. To obtain the transformation matrix for an individual grain from the local to specimen coordinate system, Eq. 4.1 can be inverted, ie.,

$$\mathbf{C}_s = \mathbf{g}^T.\mathbf{C}_c \tag{4.3}$$

For proper orthogonal transformation is defined as: $\mathbf{g}^T = \mathbf{g}^{-1}$. It should also be noted that by restricting the range of certain combinations of the Euler angle, it is possible to create a specific texture. Note that the texture can significantly affect the deformation behaviour of the cut material due to the anisotropy of the CRSS, and the most important orientation angle of Φ is adopted to determine the influence of various textures on polycrystal mechanical properties. Its influence on the material response will be investigated in the proposed cutting parametric studies.

4.2.2.2 Inter-granular characteristics

The behavior of the grain boundaries is captured using cohesive zone elements. These elements are characterised by a zero initial thickness which can describe adequately the behavior of an interface through a constitutive relationship taking into account the relative opening displacement fo the interface, δ. Based on the early researches of Dugdale [DUG60] and Barenblatt [BAR62], many different types of traction-separation laws have been developed [CHA02] to feed the elaboration of cohesive zone elements. Later, this kind of element has been used to model grain boundaries [ESP03, LUT09].

In this study, the grain boundaries which constitute also grain interfaces are modelled using four nodes cohesive zone elements (the grains are modelled by hexagonal shapes following the work of Mayeur [MAY04]). According to the research works of Xu and Needleman [XU94], the geometrical representative arrangement of the elaborated FE model (triangle and quadrilateral elements) are presented in Fig. 4.8, a) and b). The connection nodes at the level of grain interfaces are shown in Fig. 4.8 c). The initial coordinates of each grain interface nodes are identical. Also, it is important to underline that the interpenetration is not allowed due to the strong stiffening response of the normal cohesive traction in compression. Finally, the zero thickness cohesive zones are achieved with a program built under MATLAB and exported to the ABAQUS as input file.

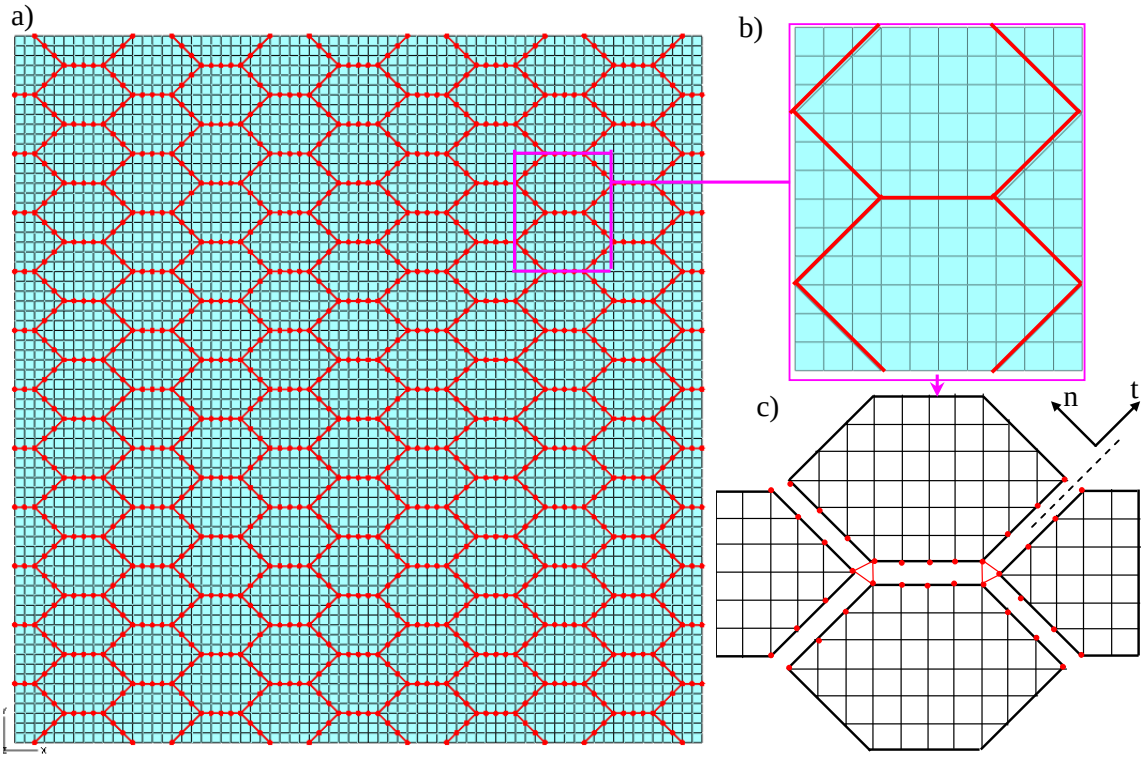

Fig. 4.8 Element arrangements and node connections in the finite element discretization. a) Boundaries of hexagonal geometry are cohesive elements, b) Arrangement of triangle and quadrilateral elements in each hexagonal grain, c) Node connections at grain interfaces.

4.2.3 Material constitutive models

4.2.3.1 Crystal plasticity theory coupled with damage for modeling intra-granular behavior

The crystal plasticity model elaborated to model the intra-granular behaviour is implemented with the user subroutine VUMAT. As the co-rotational coordinate system (in which the basis system rotates with material, and all the VUMAT variables are updated based on the basis system) is used in this mode-ABAQUS /Explicit model [ABA10], the small strain assumption with additive decomposition of the strain rate into an elastic and a plastic part is used in this work. The resolved shear stress obtained with Schmid law Eq. 4.4 is used to describe inelastic material flow.

In order to avoid problems related with the determination of the active slip systems, a viscoplastic framework Eq. 4.5 is chosen following the works of Dick and Cailletaud [DIK06]. A threshold of the resolved shear stress τ^{α} (isotropic hardening and kinematic hardening function) is introduced both along the positive and the negative direction for each slip system. Here the exponent alpha denotes the symbol of the slip plane.

Two hardening variables are defined for each slip system. The isotropic hardening r^{α} describes an expansion while the kinematic one x^{α} depicts the hardening with a translation of the elastic domain. A slip system will be active when the resolved shear stress τ^{α} is found greater than $(x^{\alpha} + r^{\alpha})$ or less than $(x^{\alpha} - r^{\alpha})$. The state variables used to describe the evolution of r^{α} and x^{α} are the accumulated slip γ_{cum}^{α} for both isotropic hardening r^{α} and for kinematic hardening x^{α}. Knowing the stress tensor $\underline{\underline{\sigma}}^{g}$ applied to the grain, the derived shear stress can be classically written according to Eq. 4.4.

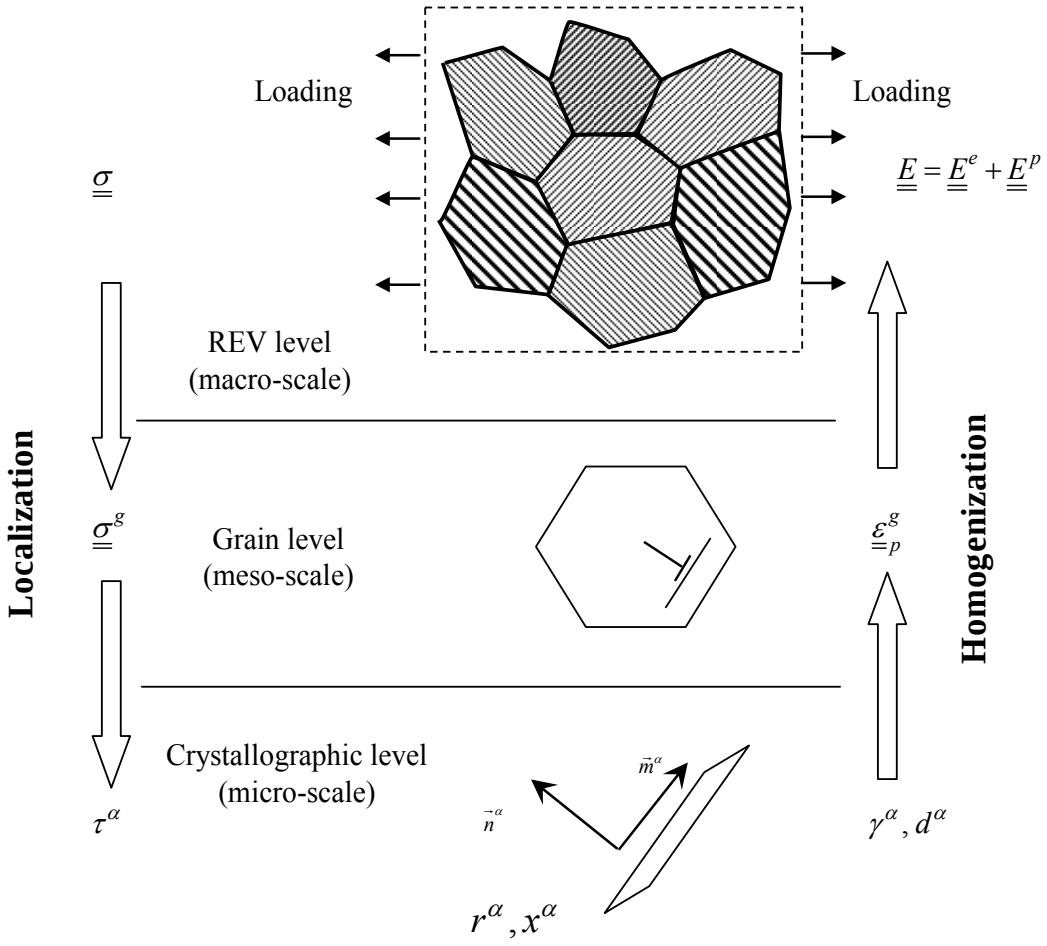

Fig. 4.9 Schematic representation of slip plane and slip direction

In order to elaborate the cutting model based on the cut material microstructure, three levels of formalism have to be treated correspondingly the scale definition in Fig. 3.4. The first one concerns the consideration of material behavior at the crystallographic level (micro - scale). The second level concerns the consideration of the averaged material behavior of the grain (meso - scale). The third level relies on the consideration of the bulk material behavior (macro - scale).

→ *Micro - scale: crystallographic level*

$$\tau^{\alpha} = \underline{\underline{\sigma}}^{g} : \underline{\underline{\mu}}^{\alpha} = \frac{1}{2}\underline{\underline{\sigma}}^{g} : (\vec{n}^{\alpha} \otimes \vec{m}^{\alpha} + \vec{m}^{\alpha} \otimes \vec{n}^{\alpha}) \tag{4.4}$$

where $\underline{\underline{\mu}}^{\alpha}$ is the Schmid factor, $\vec{n}^{\alpha}$ and $\vec{m}^{\alpha}$ being respectively the normal to the slip plane and the slip direction of the slip system (as presented in Fig. 4.9).

$$\begin{cases} \dot{\gamma}^{\alpha} = \dot{\gamma}^{\alpha}_{cum} sign(\tau^{\alpha} - x^{\alpha});\ \dot{\gamma}^{\alpha}_{p} = \dot{\gamma}^{\alpha} \\ \dot{\gamma}^{\alpha}_{cum} = \left\langle \dfrac{\left|\tau^{\alpha} - x^{\alpha}\right| - r^{\alpha}}{K} \right\rangle^{n} ;\ with \left\langle x \right\rangle = Max(x,0)\ and\ \gamma^{\alpha}_{cum}(t=0) = 0 \end{cases} \tag{4.5}$$

The hardening variables can then be expressed as function of γ^{α}_{cum} (accumulated plastic strain in the slip system) and x^{α} (slip system back stress) following Eq. 4.6, used to compute the viscoplastic slip rate $\dot{\gamma}^{\alpha}$ (which is equal to the plastic slip rate $\dot{\gamma}^{\alpha}_{p}$ when damage is not considered).

$$\begin{cases} \dot{x}^{\alpha} = c\dot{\gamma}^{\alpha} - dx^{\alpha}\dot{\gamma}^{\alpha}_{cum} \quad with\ x^{\alpha}(t=0) = 0 \\ r^{\alpha} = R_0 + Q\sum_{r} \mathbf{h}_{r\alpha} \left\{1 - e^{-b\gamma^{r}_{cum}}\right\} \left\{1 - \left(\dfrac{T - T_0}{T_{melt} - T_0}\right)^{m}\right\} \end{cases} \tag{4.6}$$

where c, d, R_0, Q, b, n ,m, T_0, *and* T_{melt} are the input material parameters. The matrix $\mathbf{h}_{r\alpha}$ is used to describe the interactions between different slip systems. In this study, the interaction matrix $\mathbf{h}_{r\alpha}$ is set to one in the diagonal and zero elsewhere, so only self hardening and no cross hardening is present. The temperature softening contribution is presented by Eq. 4.6 with an initial room temperature T_0 and a melt temperature T_{melt}.

To describe the material degradation progress through its the initiation and evolution steps, the internal damage variable d^{α} at the CSS level of the HCF grain is introduced based on the viscoplastic damage model of Lemaitre and Chaboche [LEM02]. The main steps of the algorithm are briefly presented below. The accumulated plastic strain in the slip system is first calculated:

$$\dot{\gamma}_{cum}^{\alpha} = \left\langle \frac{\left| \frac{\tau^{\alpha}}{1-d^{\alpha}} - x^{\alpha} \right| - r^{\alpha}}{K} \right\rangle^{n} \tag{4.7}$$

then the plastic strain rate is derived:

$$\dot{\gamma}_{p}{}^{\alpha} = \frac{\dot{\gamma}_{cum}^{\alpha}}{\left(1-d^{\alpha}\right)} \operatorname{sgn}\left(\frac{\tau^{\alpha}}{1-d^{\alpha}} - x^{\alpha}\right) \tag{4.8}$$

and the damage increment in the slip system is expressed by:

$$\Delta d_{NC}^{\alpha} = \frac{d_{C}{}^{\alpha}}{\left|\gamma_{p}^{c} - \gamma_{p}^{s}\right|^{\alpha}} \frac{\triangle \gamma_{cum}^{\alpha}}{\left(1-d^{\alpha}\right)} \tag{4.9}$$

Wherein, $d_{C}{}^{\alpha}$ is the critical value of the damage, γ_{p}^{s} is the minimum plastic strain to initiate damage, γ_{p}^{c} is the plastic strain for complete damage, and Δd_{NC}^{α} is damage increment without correction.

To prevent the mesh dependency problem, the delayed damage model is introduced in this part. This idea was from the the work proposed by a team of the "Laboratoire de Mécanique et de Technologie de Cachan" within the framework of the studies on the fracture of composite laminates [ALL97, ALL99], and it was developed by Suffis et al. [SUF03] later. In the delayed damage model, two parameters are introduced. One is the characteristic time τ_c representing the inverse of the maximum damage rate. The equation of the damage rate evolution is expressed by:

$$\begin{cases} \dot{d}^{\alpha} = \dfrac{1}{\tau^{c}}\left(1-\exp\left[-a_{D}\left\langle d_{NC}^{\alpha} - d^{\alpha}\right\rangle\right]\right) & \text{if } d^{\alpha} \le d_{c}^{\alpha} \\ d^{\alpha} = d_{c}^{\alpha} \end{cases} \tag{4.10}$$

The second parameter of the model is the coefficient a_D. The classical definition of damage without delay correction is defined by d_{NC}^{α}. The damage rate is the function of the different between this classical damage without delay and the damage d^{α} with delay effect. With this method, a rapid variation of the damage energy release rate will not lead to an immediate evolution of the damage, and then the damage will evolve with a certain delay dominated by the characteristic time independent of the mesh.

→ *Meso-scale: Grain averaged stress and deformation definitions*

The Köroner model is adopted [KOR61] for the plastic deformation of polycrystals. This author has applied the Eshelby solution for the problem of an ellipsoidal inclusion in an infinite medium.

Granular stress tensor:

$$\underline{\underline{\sigma}}^{g} = \underline{\underline{\sigma}} + \alpha_T \underline{\underline{\underline{\underline{\Lambda}}}} \left(\underline{\underline{E}}^{\mathrm{p}} - \underline{\underline{\varepsilon}}_p^{g} \right), \text{with}, \ \underline{\underline{\underline{\underline{\Lambda}}}} = \frac{\nu E \left(\underline{\underline{\mathrm{I}}} \otimes \underline{\underline{\mathrm{I}}} \right)}{(1+\nu)(1-2\nu)} + \frac{E \underline{\underline{\underline{\underline{\mathrm{I}}}}}}{(1+\nu)} \tag{4.11}$$

Where $\underline{\underline{\sigma}}$ and $\underline{\underline{E}}^{\mathrm{p}}$ are the average stress and plastic strain tensors, and $\underline{\underline{\sigma}}^{g}$ and $\underline{\underline{\varepsilon}}^{\mathrm{pg}}$ are the stress and plastic strain tensors of a grain. α_T (Taylor model related coefficient, phenomenological parameter characterizing the inter-granular hardening which plays an important role on plastic accommodation inside the aggregate) is equal to 1. $\underline{\underline{\underline{\underline{\Lambda}}}}$ is the fourth order elastic properties tensor for isotropic material with E and ν being the Young's modulus and the Poisson's ratio. From a physical point of view, it means that grains with higher plastic strain than the average plastic strain have a relatively lower stress than the average stress.

Granular inelastic strain tensor:

$$\dot{\underline{\underline{\varepsilon}}}_p^{g} = \sum_{\alpha} \dot{\gamma}_p{}^{\alpha} \underline{\underline{\mu}}^{\alpha} \tag{4.12}$$

→ *Macro - scale: Bulk material average stress and deformation definitions*

Here the macroscopic strain rate tensor is defined as:

$$\dot{\underline{\underline{E}}} = \dot{\underline{\underline{E}}}^{e} + \dot{\underline{\underline{E}}}^{p} \tag{4.13}$$

where the macroscopic stress tensor is given by:

$$\underline{\underline{\sigma}} = (1-D) \underline{\underline{\underline{\underline{\Lambda}}}} : \left(\underline{\underline{E}} - \underline{\underline{E}}^{p} \right) \ \text{with} \ \underline{\underline{E}}^{p} = \sum_{g} f^{g} \underline{\underline{\varepsilon}}_p^{g} \tag{4.14}$$

The total damage is given as following:

$$\dot{D} = \sum_{g} f^{g} \sum_{\alpha} \dot{d}^{\alpha} \tag{4.15}$$

Where $\underline{\underline{E}}$ is the total strain tensor of Green-Lagrange, f^g is the relative volume fraction of grains having the same orientation (as all orientation angles are assumed to be the same for all the elements in one grain, f^g is taken as equal to one here).

4.2.3.2 Inter-granular flow law for cohesive zone

The cohesive zone model presented below is implemented in the commercial FE package, ABAQUS with the user subroutine VUMAT. In particular, cohesive elements are defined along the potential paths of crack growth. The constitutive properties of the cohesive elements are specified in terms of the traction-separation laws. In this study, the bilinear traction-separation law (Fig. 4.10) is adopted to allow inelastic sliding to occur at the grain boundaries.

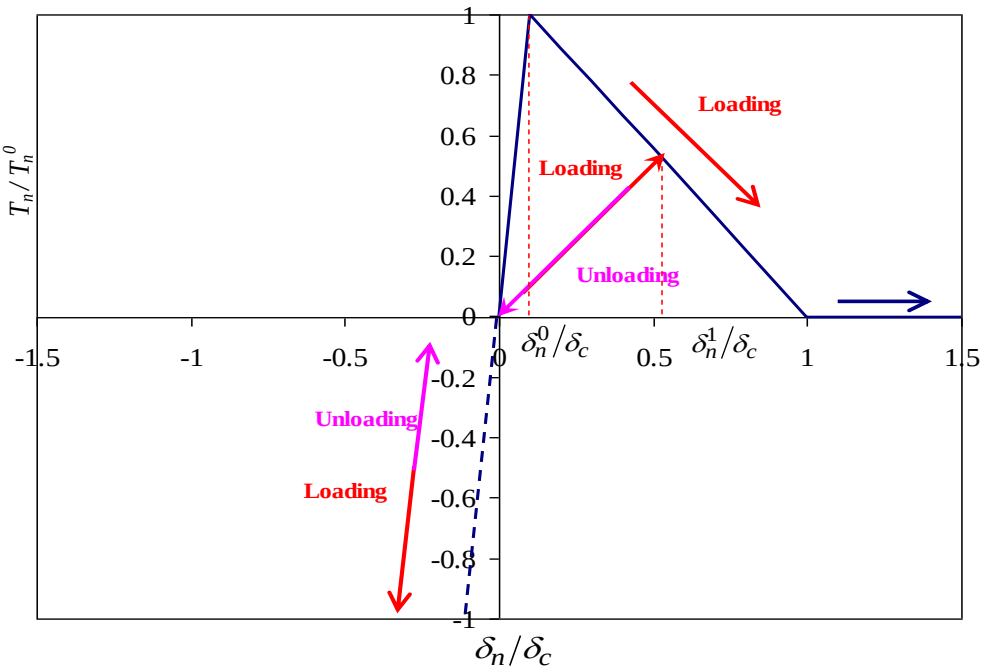

a) Pure tension

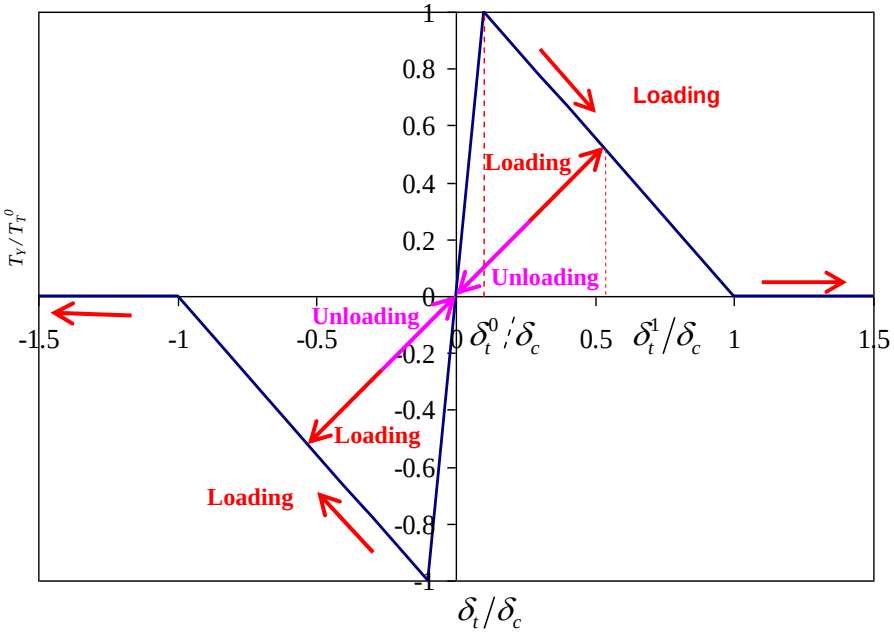

b) Pure shear

Fig. 4.10 Constitutive response of bilinear traction-separation for a) pure tension, and b) pure shear

The cohesive law assumes that normal and tangential tractions (regarding grain interface), T_n and T_T, respectively, are linear functions regarding normal and tangential displacements, δ_n and δ_t, respectively. In the local element directions, the stress strain relations for uncoupled behavior are as follows:

$$\begin{cases} T_n = k_n\delta_n = \dfrac{\delta_n^0}{\delta_n^1}k_n^0(1-D_n)\delta_n \\ T_t = k_t\delta_t = \dfrac{\delta_t^0}{\delta_t^1}k_t^0(1-D_t)(1-D_n)\delta_t \end{cases} \tag{4.16}$$

Where k_n and k_t are present stiffness of the cohesive zone in normal and tangential directions, respectively, which are corresponding to the initial stiffness k_n^0 and k_t^0. δ_n^0 and δ_t^0 are the traction displacements of damage initiation in normal and tangential directions, while δ_n^1 and δ_t^1 are the maximum values of δ_n and δ_t achieved during prior loading. D_n and D_t are damage variables for describing the traction process. It should be noted that Fig. 4.10 is the schematic presentation of cohesive law. As the stiffness of present model is very high, the interpenetration of grains is now allowed in this definition.

→ *The Maximum nominal stress criterion*

Damage is assumed to initiate when the maximum nominal stress ratio given by Eq. 4.17 reaches a value of one:

$$\max\left\{\frac{\langle T_n\rangle}{T_n^0(1-D_n)}, \frac{|T_t|}{T_t^0(1-D_t)(1-D_n)}\right\}=1 \tag{4.17}$$

where T_n^0 and T_t^0 are the material parameters specifying the normal and tangential tractions (i.e., fracture in mode I and II, respectively), corresponding the traction displacements of δ_n^0 and δ_t^0 in normal and tangential directions, respectively.

$\rightarrow$ *Damage evolution for loading and unloading*

After initiation of damage, the constitutive behavior of the degraded material (i.e., within the cohesive zones) at the interface is presented by the following set of coupled irreversible traction – displacement relationships [CLA05]:

$$\begin{cases} T_n = T_n^0(1-D_n),\ D_n = \dfrac{\delta_n-\delta_n^0}{\delta_c-\delta_n^0}\ \text{(loading)} \\ T_n = T_n^0(1-D_n)\dfrac{\delta_n}{\delta_n^1},\ D_n = \dfrac{\delta_n^1-\delta_n^0}{\delta_c-\delta_n^0}\ \text{(unloading)} \end{cases} \tag{4.18}$$

$$\begin{cases} T_t = T_t^0(1-D_t)(1-D_n)\,\mathrm{sgn}(\delta_t),\ D_t = \dfrac{|\delta_t|-\delta_t^0}{\delta_c-\delta_t^0}\ \text{(loading)} \\ T_t = T_t^0(1-D_t)(1-D_n)\dfrac{\delta_t}{|\delta_t^1|},\ D_t = \dfrac{|\delta_t^1|-\delta_t^0}{\delta_c-\delta_t^0}\ \text{(unloading)} \end{cases} \tag{4.19}$$

Where δ_c is a material parameter describing the separation distance at which the cohesive interface no longer supports traction (i.e., the critical opening displacement for total failure). The parameters are assumed to be constant and are given as shown in Table 4.4. Noted that the constants marked with symbol "*" on upper right corner is referenced from Slack and Sadeghi [SLA11].

Elastic Modulus E (GPa)	119
Poisson's ratio ν	0.3
$D_{nc} = D_{nc}$	1
$k_n^0 = k_t^0$ (GPa/µm)	10,000*
$T_n^0 = T_t^0$ (GPa)	2
δ_c (µm)	1*
$\delta_n^0 = \delta_t^0$ (µm)	$0.0002\,\delta_c$ *

Table 4.4 Simulation parameters for cohesive zone

4.3 MML cutting model validation

Compression test is carried out to validate the presented material behavior coupled with two kinds of different damage models (Inter and intra-granular). In balancing the number of grains included in the statistical volume element and the computational requirements, an ensemble of 137 grains is chosen for the following simulations [MAY07]. The grains have an aspect ratio $\left(l/h\right)$ of 1.67 with the length dimension being 30 μm. The aspect ratio of a grain, and the boundary condition and initial disorientation angle distribution are illustrated in Fig. 4.11.

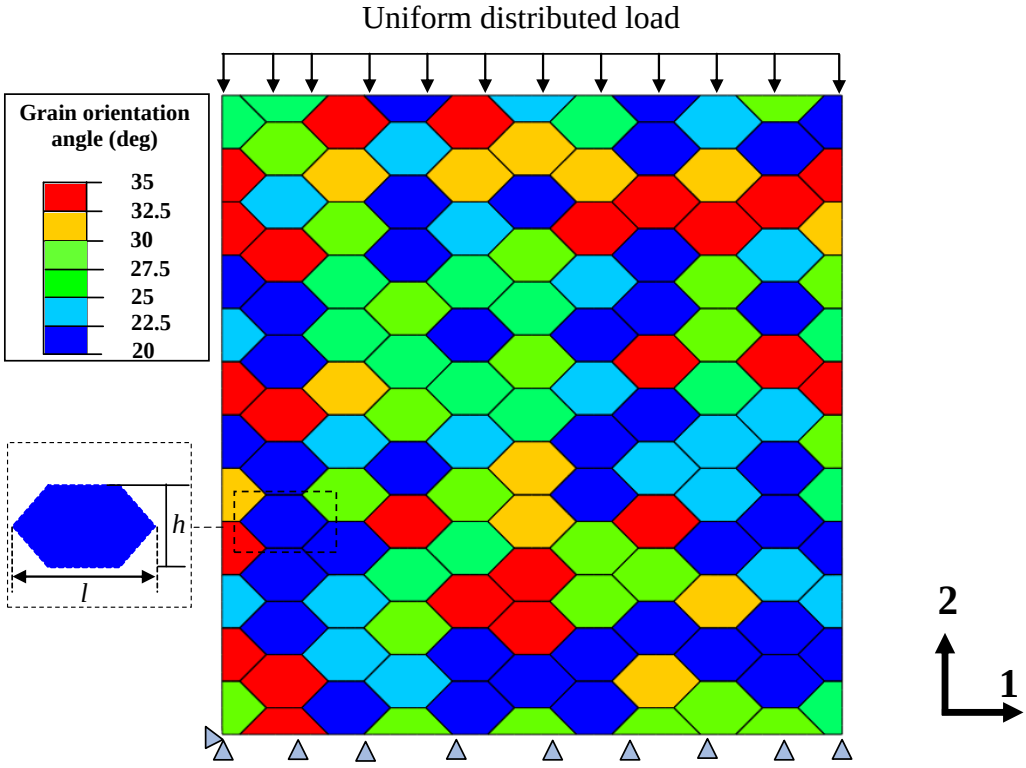

a) Schematic representation of a random distribution of grains for compression validation test

* Slack and Sadeghi [SLA11]

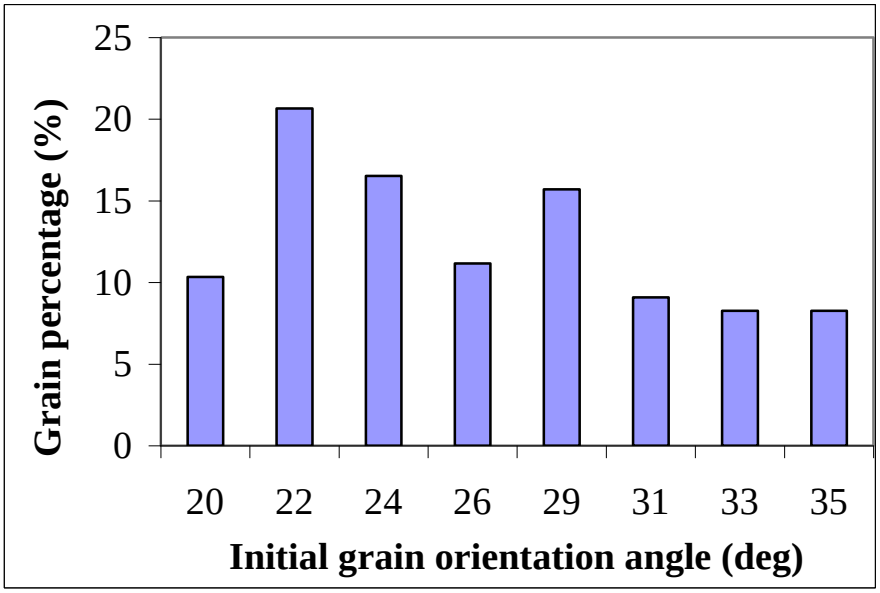

b) Initial grain orientation angle distribution of grains

Fig. 4.11 Illustration of the initial condition for compression validation test

The load is applied with constant strain rate. Notice that here we deform the crystal in uniaxial compression in the 2-direction, i.e. the macroscopic logarithmic (true) strain is defined by $\bar{\varepsilon} = \ln(1+\dot{\varepsilon}t)$, with $\dot{\varepsilon}$ is the prescribed nominal strain rate, while $\bar{\sigma} = V^{-1}\int \sigma^{22} dV$, with V is the total reference configuration volume of the polycrystal [CLA05], equally partitioned into 137 grains.

The parameters of the crystal plasticity model have been identified by comparison of the true-stress vs. true-strain curve obtained numerically to the data derived from a compression test at 25°C (Lee and Lin, 1988 [LEE98]), see Fig. 4.12. The corresponding set of parameters is listed in Table 4.5. They describe the mechanical behavior of HCP Titanium at a constant strain rate $2000s^{-1}$. It should be mentioned that the experimental data used to calibrate above model is from the research work of [LEE98], while the material stiffness degradation process is not given in his work (Actually, this is really hard to define, and this process is seriously affected by many factors: temperature, various strain rate, etc.). However, the material stiffness degradation process is observed in machining process for two aspects: one side is for chip and workpiece separation process, another side is for the chip segmentation process (shear bands). Following the work of Suffis et al. [SUF03], the delayed damage values are adopted in Table 4.5 which is suitable to the cutting process, and the critical damage parameters $d_C{}^{\alpha}$, for the slip system, are considered as 0.3 and 0.999 for the deleted damage part and chip part, respectively.

Calibration test between the model prediction and the experimental results for HCP Titanium alloys is shown in Fig. 4.12. The calibrated parameters are illustrated by Table 4.5 for the crystal plastic model.

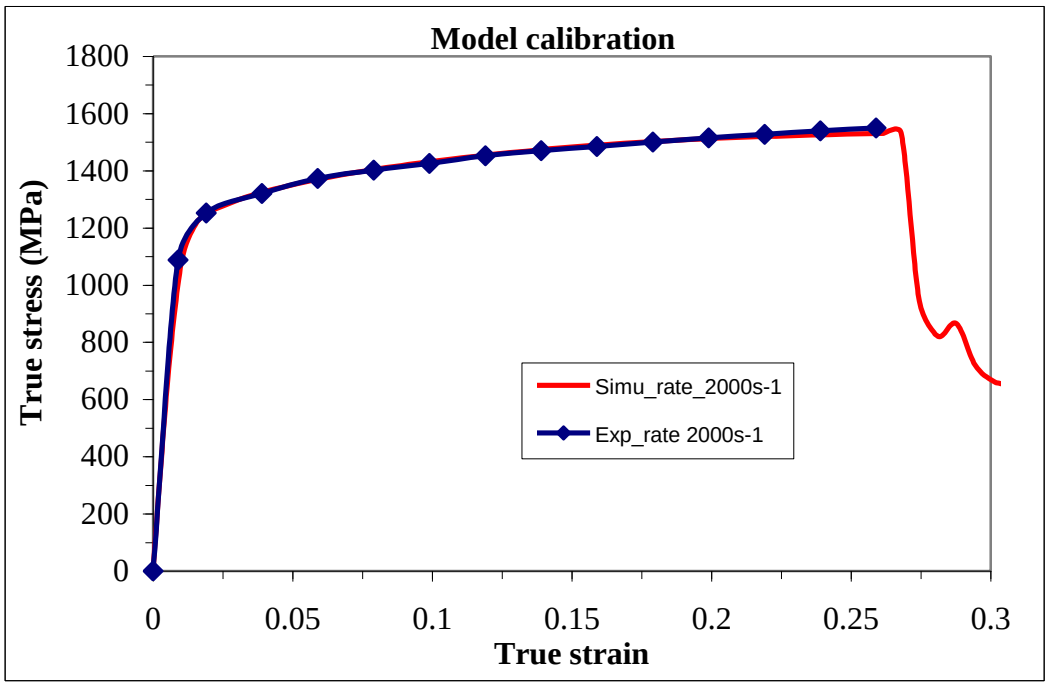

Fig. 4.12 Model calibration on compression test on Ti-6Al-4V based on experiment by Lee and Lin [LEE98] in case of a constant strain rate

Parameter		Prismatic	Basal	Pyramidal <α>	Appendix
E (MPa)		119,000			
ν		0.3			
m		0.75♣			Hardening variables
n		7.41♣			
R_0 (MPa)		280	300	540	
Q (MPa)		400	520	830	
b		2			
c (MPa)		30,000♣			
d		300♣			
T_0 (°C)		25			
T_{melt} (°C)		1630			
ε_p^s		0.2			Damage related parameters
ε_p^c		0.4			
d_C^{α}		0.999			
D	**Chip part**	0.999			
	Damage part	0.3			
τ^c (ms)		0.00004			
a_D		2.25			

Table 4.5 Parameters of the crystal plasticity material model [DIC06]

4.3.1 Parametric study with various temperature

As temperature is one of the most important factors that determine material flow behavior, some additional numerical tests have then been performed with the same set of parameters but at 300 and 500°C keeping the constant strain rate 2000 s^{-1}. Simulation results are shown in Fig. 4.13. Compared to experimental ones, good agreement is obtained for the material flows with various temperatures. So, this material microstructure-level model is able to predict macro material flow behavior with multi-scale material constitutive model considering thermal influence.

♣ DICK and CAILLETAUD [DIC06]

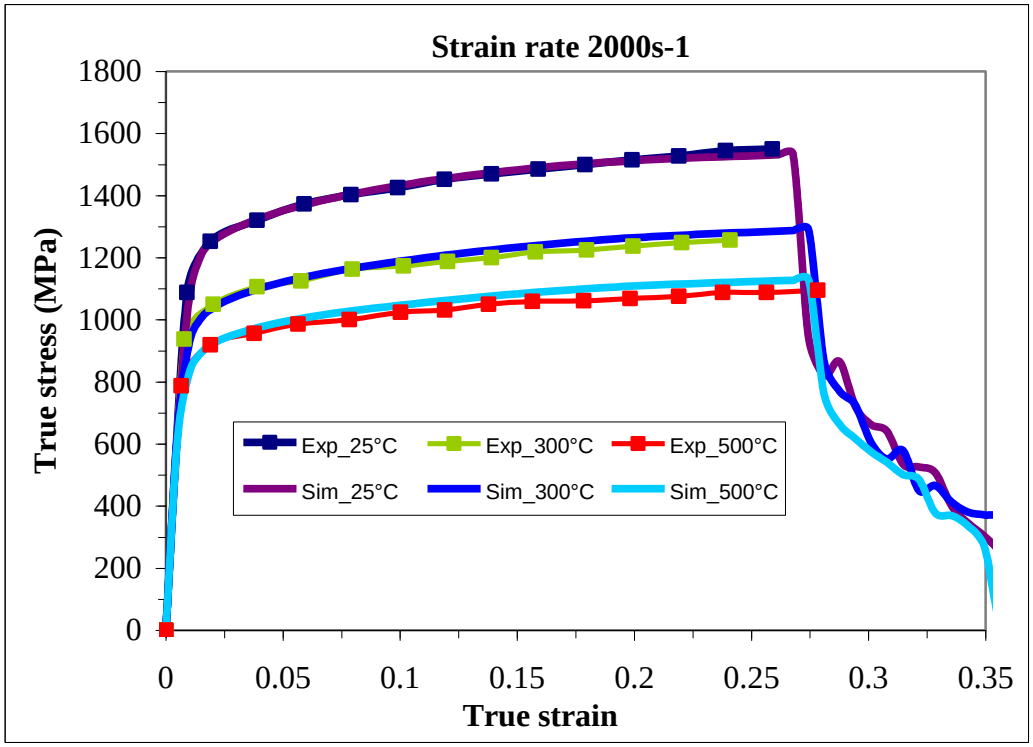

Fig. 4.13 Model prediction vs. experiments for compression of Ti–6Al–4V material at 25°C, 300°C and 500°C [LEE98]

4.3.2 Parametric study with different strain rate

With above calibrated mode, compression tests with different strain rates are also performed to study the influence on the dynamic stress response, and the corresponding results are presented in Fig. 4.14. It can be seen that the curve is not sensitive for the strain rate 800 s^{-1} and 2000 s^{-1}, while the obvious difference appears with the further increased strain rate 6000 s^{-1}. The main reason of low sensitivity for low strain rate is that the small value K set in the crystal visco-plasticity model. However, this simulation results are similar to those experimental values that can be found in the literature [LEE98]

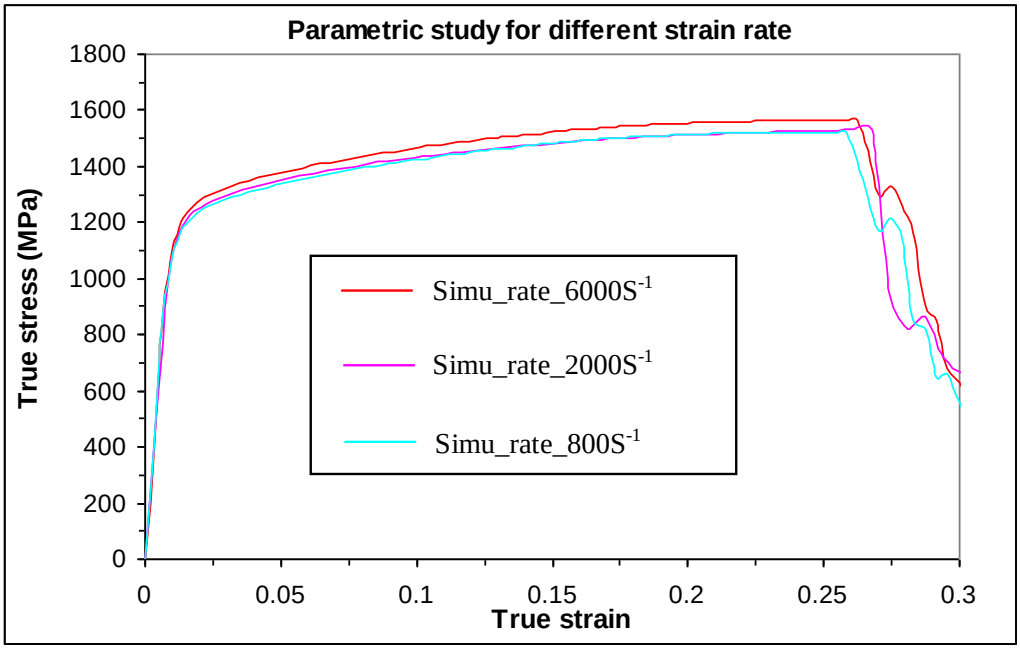

Fig. 4.14 Parametric study of different strain rate with initial temperature 25°C

4.4 Simulation capabilities of the MML cutting model

The lagrangian description is employed to develop the cutting model. The meshed geometrical cutting model is illustrated in

Fig. 4.15. For the workpiece, the UCP is equal to 0.1 mm with a cutting depth of a_p = 3 mm. The active part of the cutting tool is corresponding to an uncoated carbon insert referenced TPKN 1603 PPR with normal rake and flank angles of 0° and 11°, respectively. The tool entering and inclination edge angles are 90° and 0°, respectively. The tool-cutting edge radius is of 30 μm. The tool-workpiece interaction is considered under dry machining conditions. The crystal plasticity model is adopted for grain behavior in the workpiece, and cohesive elements are assigned to grain interface as described above. To improve the understanding on the effect of grain orientation angle (GOA) on both chip formation and surface integrity, the distribution of the orientation angles of grains is arranged in regular staggered columns with 0°, 30°, 45°, 60°.

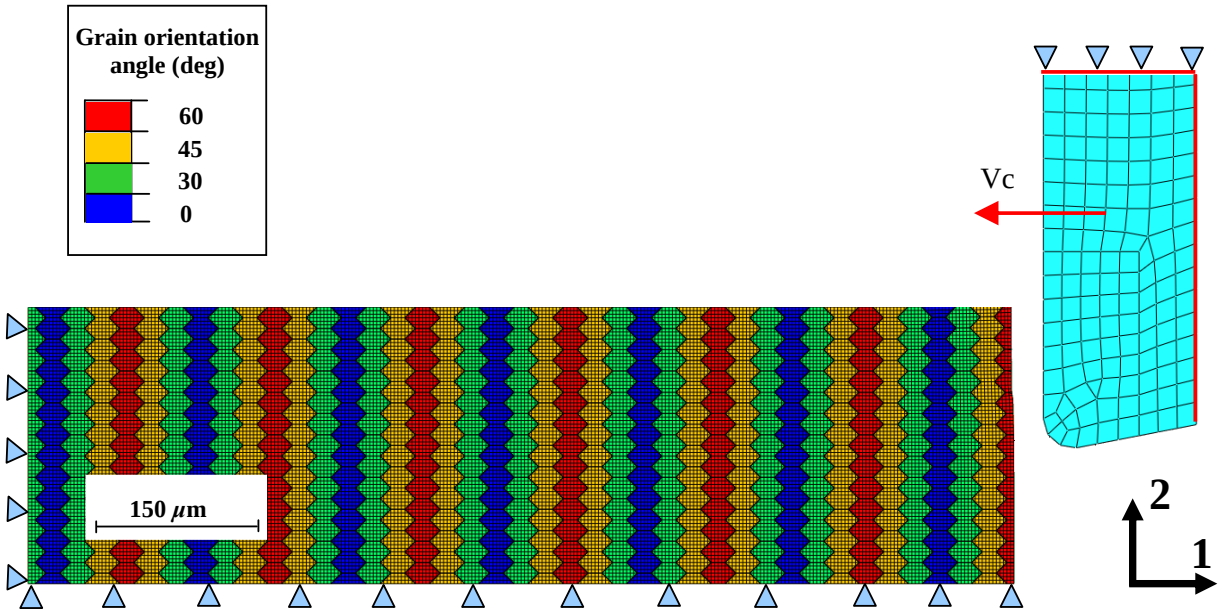

Fig. 4.15 Model mesh and boundary conditions with a regular distribution of GOAs

Boundary conditions: the workpiece is assumed to be fixed on its bottom and left sides, and the cutting tool was allowed to move horizontally from the right to the left at a constant velocity while restrained vertically. The friction contact model of Zorev ([ZOR63]) is adopted in this model, and the coefficient of friction (CoF) is assumed equal to 0.1.

4.4.1 Chip formation prediction based on MML cutting model

4.4.1.1 GOA effect on chip formation

The cutting model is now applied to the polycrystal material structure illustrated in

Fig. 4.15. Cohesive elements are used to model grain interfaces, which imply that two adjacent grains are allowed to slide against each other. Consequently, regular chip segmentations are formed during cutting as shown in Fig. 4.16. A meticulous analysis of chips obtained numerically shows that the segmentation phenomenon is mainly caused by i) shear slip between grains and ii) crystallographic slip in the grains which are deformed by extruding. This is validated by the correspondingly experiment that we have carried out and pointed out by the magnified part of the chip in the shear band presented in Fig. 4.17. Furthermore, it is remarked on the one hand that the "segmentation peak" is always located at the 0° of the GOA that is considered as "soft phase" in material and which shows the largest strain. On the other hand, the "segmentation valley" corresponds to a GOA of 60° that can be regarded as "hard phase" and which leads to the smallest strains. Finally it could be also observed that the

largest relative slip occurs at interface between grains orientated at 45°C (which can be also considered as hard phase compared to the direction of loading) and those at 60°.

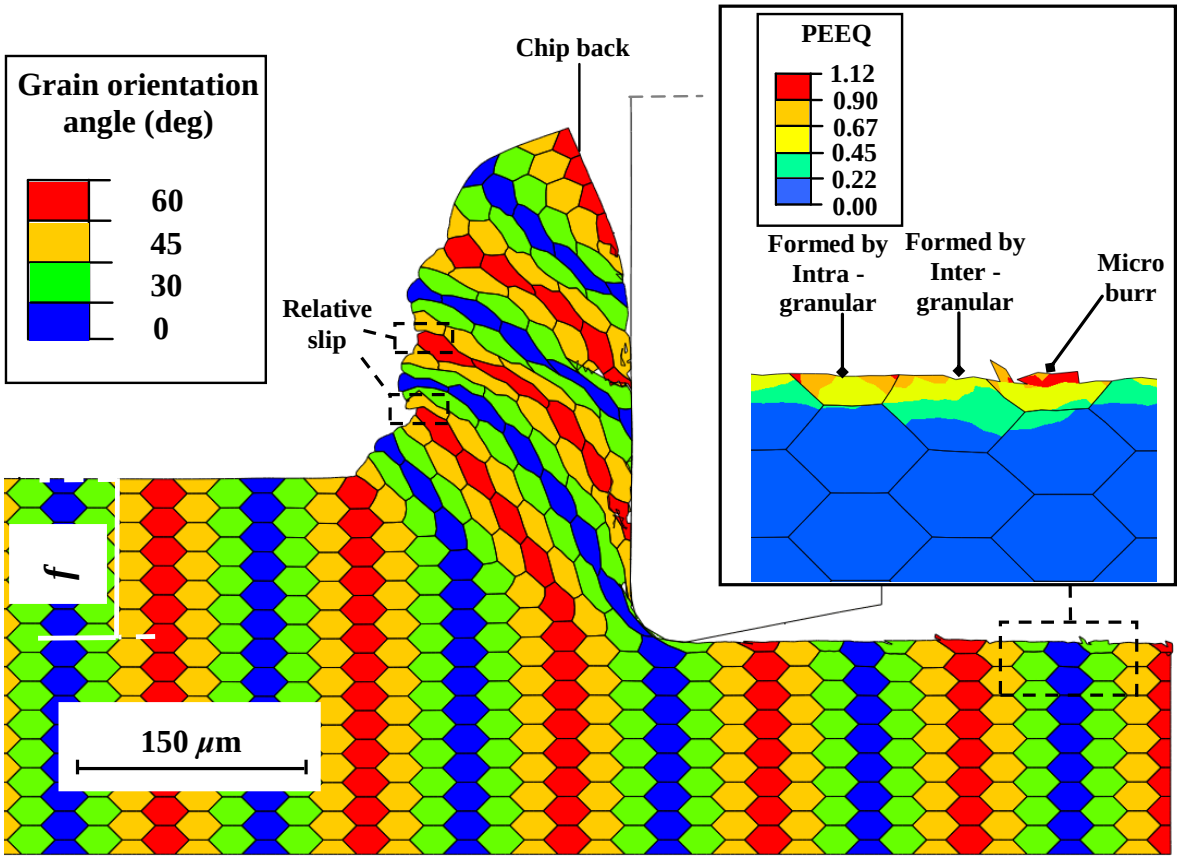

Fig. 4.16 Initial orientation distribution of grains with cutting speed 90 m/min and feed rate 0.1 mm/rev

For the general case, the shape and segmentation of the chip can be observed in Fig. 4.17. Where the numerical and experimental chips differ significantly – which can be attributed to the very different distribution of grain orientation – It is clear that there are some relationships between the chip segmentation and the deformed grain orientation (different for peaks and valleys). It can be also mentioned that the chip segmentation is not really periodic from an experimental point of view when compared to the academic simulation presented in Fig. 4.16. Again this is due to the fact that, in the proposed cutting model, the grain orientations are periodic which implies periodic chip segmentation while those corresponding to the experiments are randomized yielding to a non-periodic segmentation. Certainly, the proposed numerical model with regular grain disposal is an academic case but it helps to bring a physical comprehension of the segmentation phenomenon and its periodicity or not.

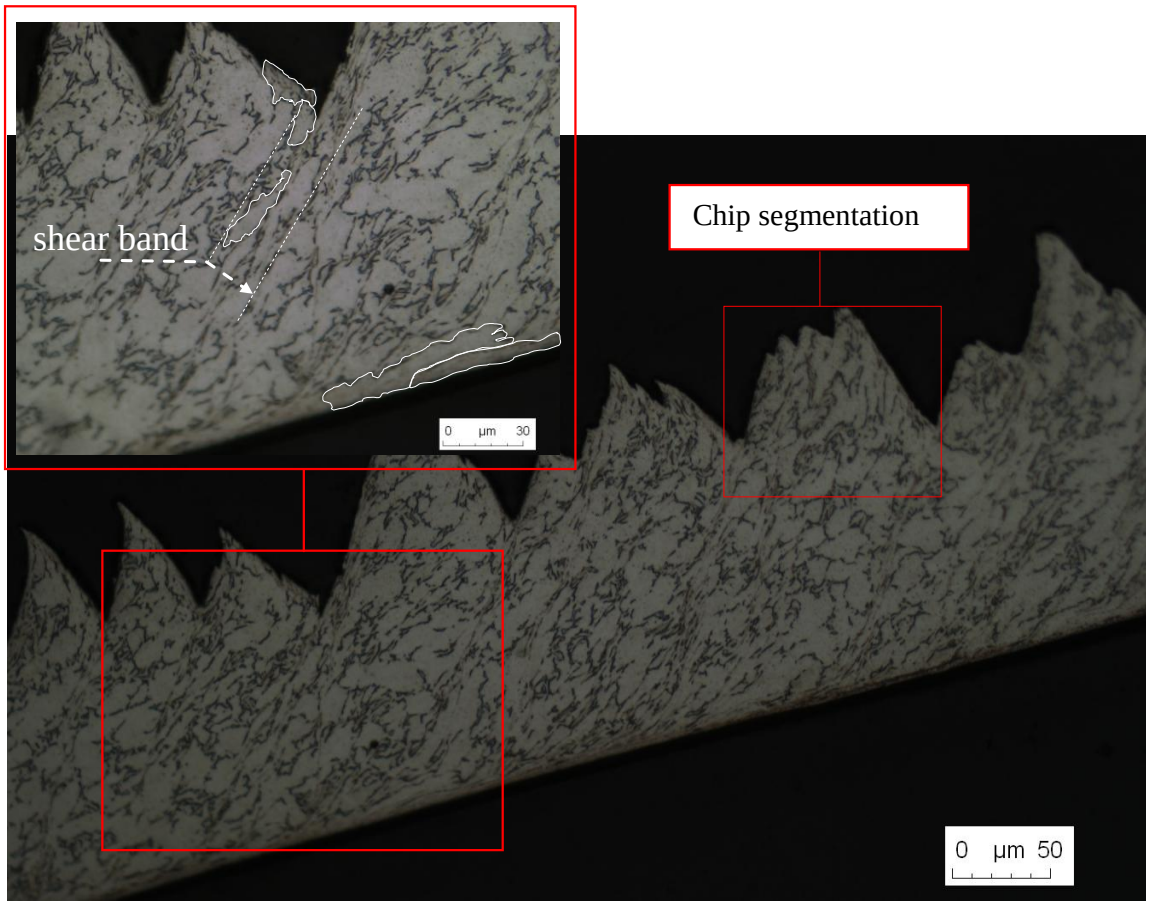

Fig. 4.17 Experimental observation of Ti–6Al–4V chip with cutting speed V_c = 90 m/min and feed rate f = 0.1 mm/rev

To give the reader more global details about the spatial disposition of real segmentations, the back of a chip formed experimentally, cutting speed of 90 m/min with a feed rate of 0.1 mm/rev, is presented in Fig. 4.18. The result shows a weak periodic of these segmentations due to the bifurcation of some segmentations on two or more little segmentations with a randomized distribution.

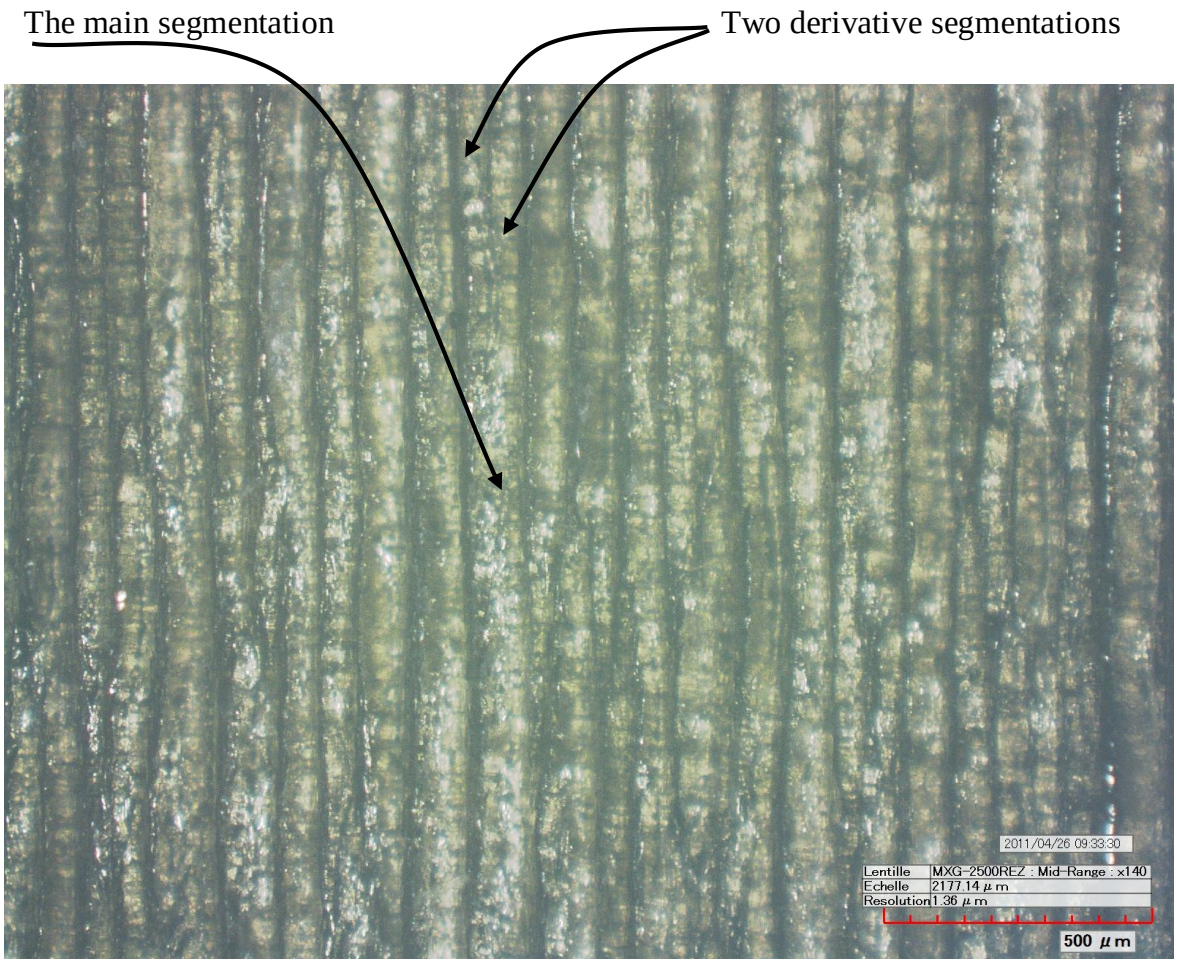

Fig. 4.18 Spatial disposition of real segments at the back of a chip formed experimentally *Vc = 90 m/min* and *f = 0.1 mm/rev*

Another important phenomenon is the new formed surfaces for both the workpiece and the chip. For the new formed surface on the chip back, both the new formed grains caused by both intra-granular and inter-granular damages are squeezed into very fine grains of size from 3 to 5 μm (Fig. 4.16). This is known in the literature as the dynamic recrystallization (DRX) which is a consequence of a catastrophic material failure where grains are subjected to rearrangements. This phenomenon can be observed on the shear band and also on the chip back surface (Fig. 4.17) which was sliding on the rake face. While for the new formed surface of the workpiece (see top right part in Fig. 4.16), micro-burrs occur caused by the intra-granular damage, it seems that inter–granular damage produces smoother surface.

Experimental result of the machined surface is shown in Fig. 4.19, where the machining affected deformation zone is highlighted with dashed red line. It is found that the size of the influenced zone is less than 30 μm (the average grain length *l*), and the grains of the affected

zone show fine grain size compared with that of the unaffected one. This is also observed in the simulation result because of new formed grains by intra-granular damage and the squeezed deformation by the cause of the serious mechanical effect of 0° rake angle.

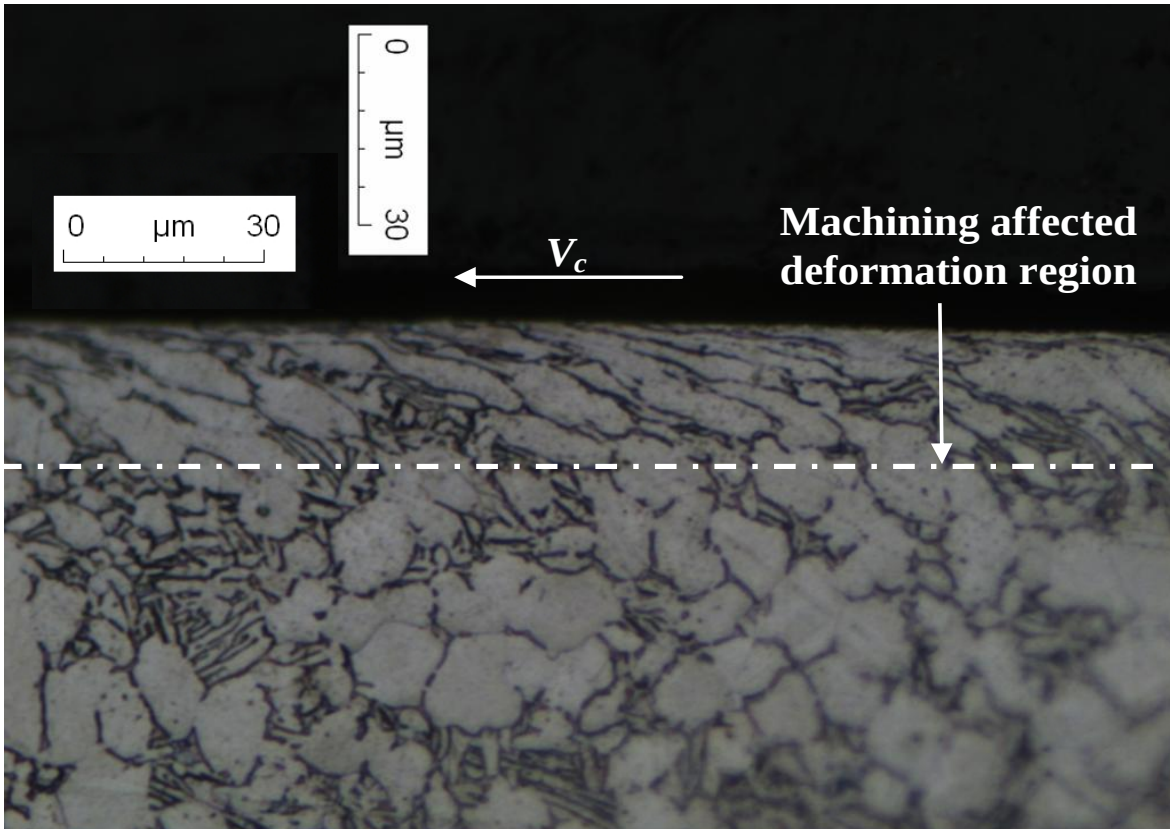

Fig. 4.19 Grain structure photos of the machined surface

To check the influence of random grain distribution, additional simulation test is performed, followed by the random grain distribution in parallel direction compared with Fig. 4.15. From Fig. 4.20 , it can be seen that the aperiodic chip segmentations generate due to the influence of irregular distribution of grain orientation angle, which can well explain the aperiodic chip segmentations observed in experiment even the shape is not the same at present. Similar to Fig. 16, the low value of grain orientation angle locates at “Chip peak”, while high value of grain orientation angle appears at “chip valley”.

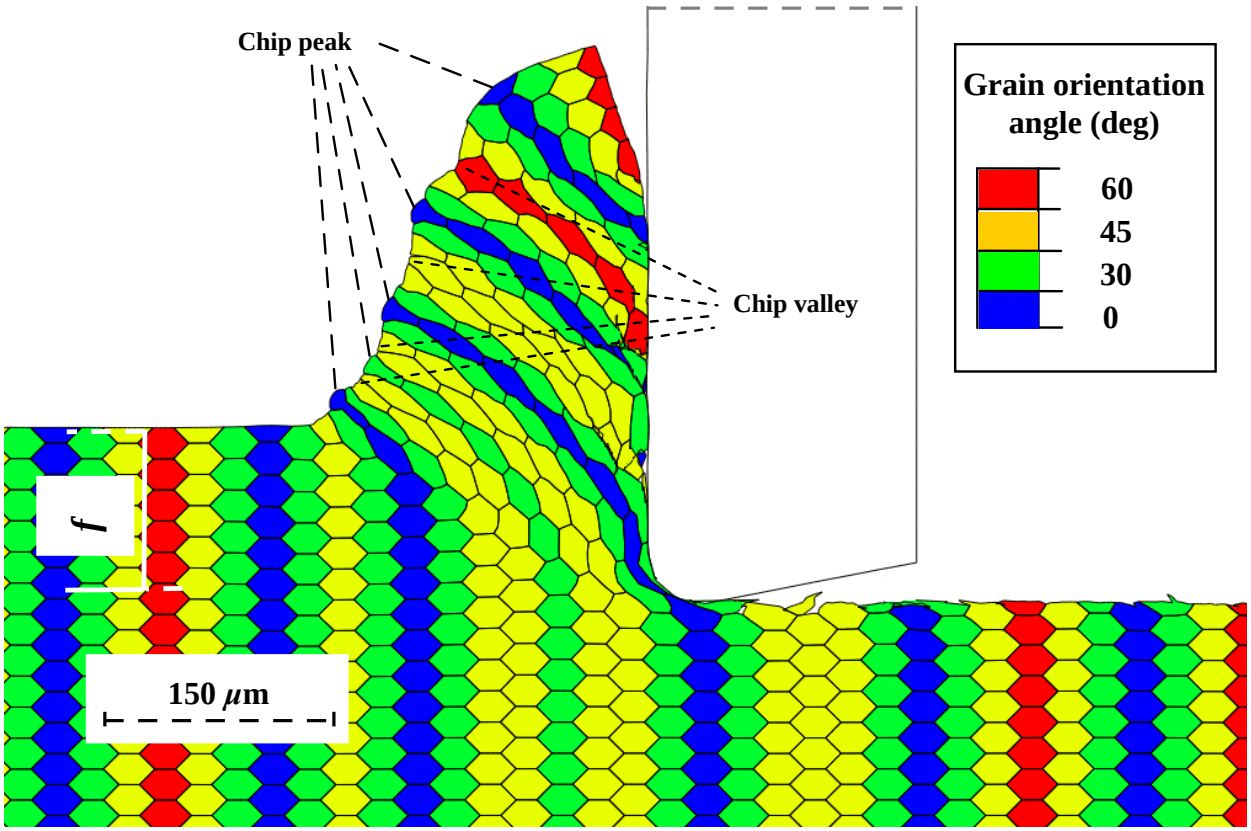

Fig. 4.20 Random grain orientation distribution with cutting speed V_c = 90 m/min and feed rate f = 0.1 mm/rev

For the general case, the formation of chip segmentation can be affected by the distribution of grain orientation according to present study, and "chip peak" and "chip valley" can be determined by the relative low and high grain orientation angles.

4.4.1.2 Cutting speed effect on chip formation considering GOA

From the previous section, it can be seen that the orientation angles of grains greatly affects the chip formation which gives new physical insights on the segmentation of chips. The effect of the cutting speeds (60, 90 and 120 m/min) is investigated here. It is shown from Fig. 4.21 that chip segmentation is more pronounced when the cutting speed increases. This is explained by severe slip between grain interfaces (see dashed pink circles from Fig. 4.21) and the crystallographic slip in the form of plastic deformation. It is noticed that the GOAs 0° and 60° correspond to chip "segmentation peak" and "segmentation valley" respectively. Another interesting observation concerns the tool-chip interface, where it can be observed that the higher is the cutting speed, denser are micro-defects at the chip back.

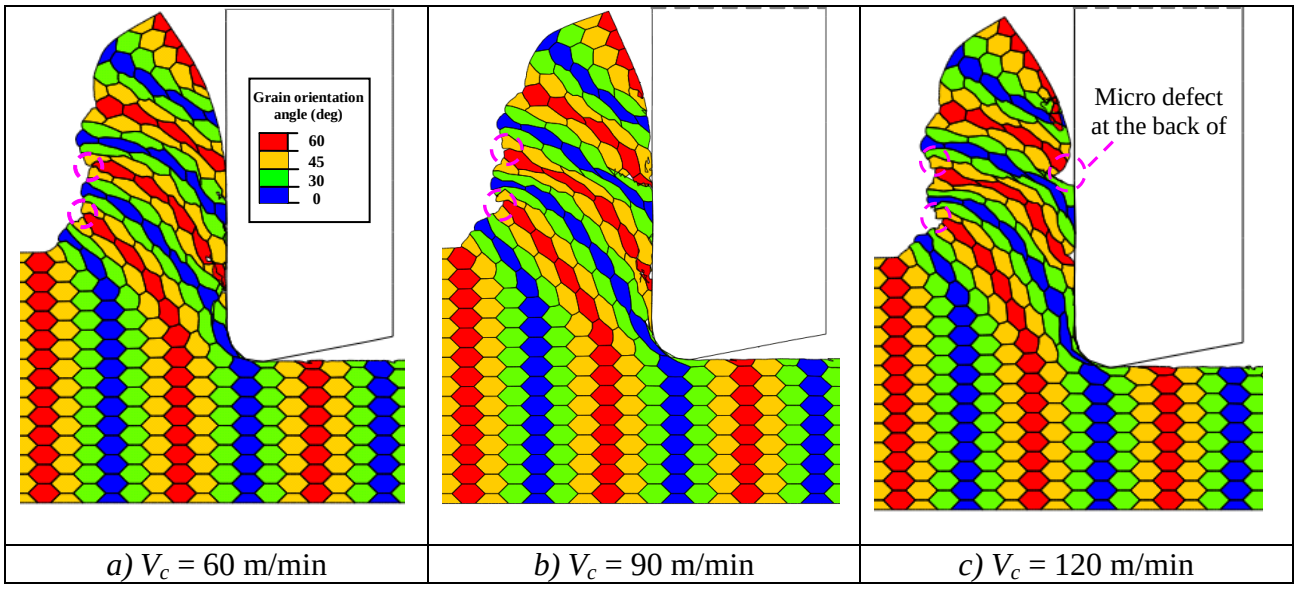

a) V_c = 60 m/min | *b)* V_c = 90 m/min | *c)* V_c = 120 m/min

Fig. 4.21 Effect of cutting speed on the chip morphology for f = 0.1 mm/rev

4.4.1.3 Feed rate effect on chip formation considering GOA

In this section, different feed rates are adopted to study the influence of regular GOA on chip formation process (Fig. 4.22). It should be noticed that the same velocity and displacement are presented for chip simulation results analysis. For the simulation results, the phenomena of chip peak and chip valley locating at high and low GOA are shown again, and the chip is more segmented with the increased feed rate. Further more, three chip segmentations are observed for the feed rate f = 0.15 mm/rev, which means that the frequency of the chip segmentation increases. Besides, the defect is observed at the back of the chip.

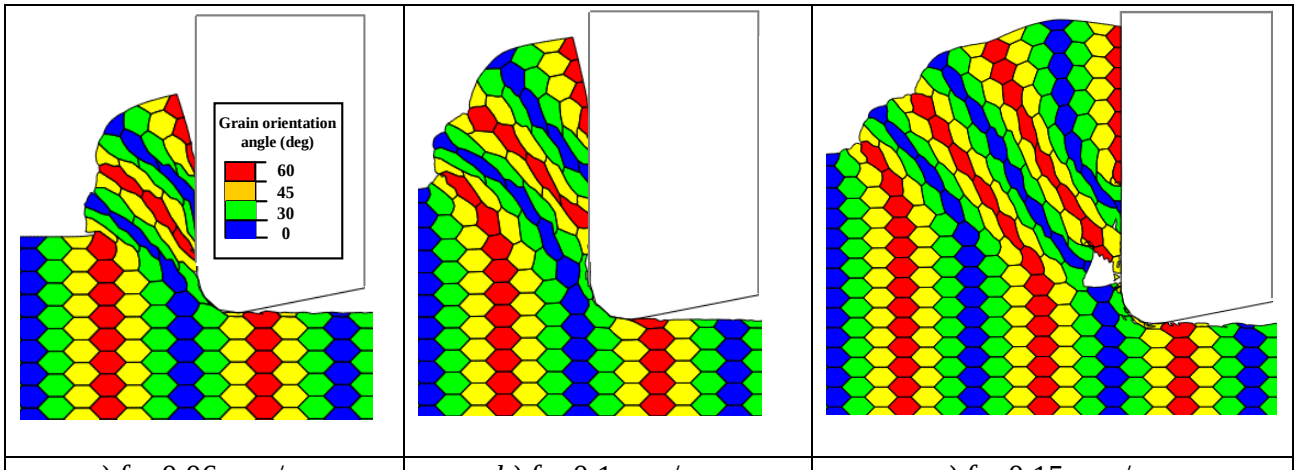

a) f = 0.06 mm/rev | *b)* f = 0.1 mm/rev | *c)* f = 0.15 mm/rev

Fig. 4.22 Distribution of the initial GOA for V_C = 60 m/min

4.4.2 Cutting force study based on MML cutting model

4.4.2.1 Cutting speed effect on cutting force

Based on the experimental set-up presented in Chapter 3 (Fig. 3.1), the average cutting forces have been measured by mean of piezoelectric dynamometer. The objective is to compare the evolutions of cutting forces for various cutting speeds and feed rates with those resulting from numerical simulations based on the MML cutting model. Both, experimental and simulation results show that cutting forces only slightly increase when varying V_c from 30 to 120 m/min with a constant cutting depth and feed rate, see Fig. 4.23. It should be underlined that the dispersion in numerical simulation is higher than that of measurements.

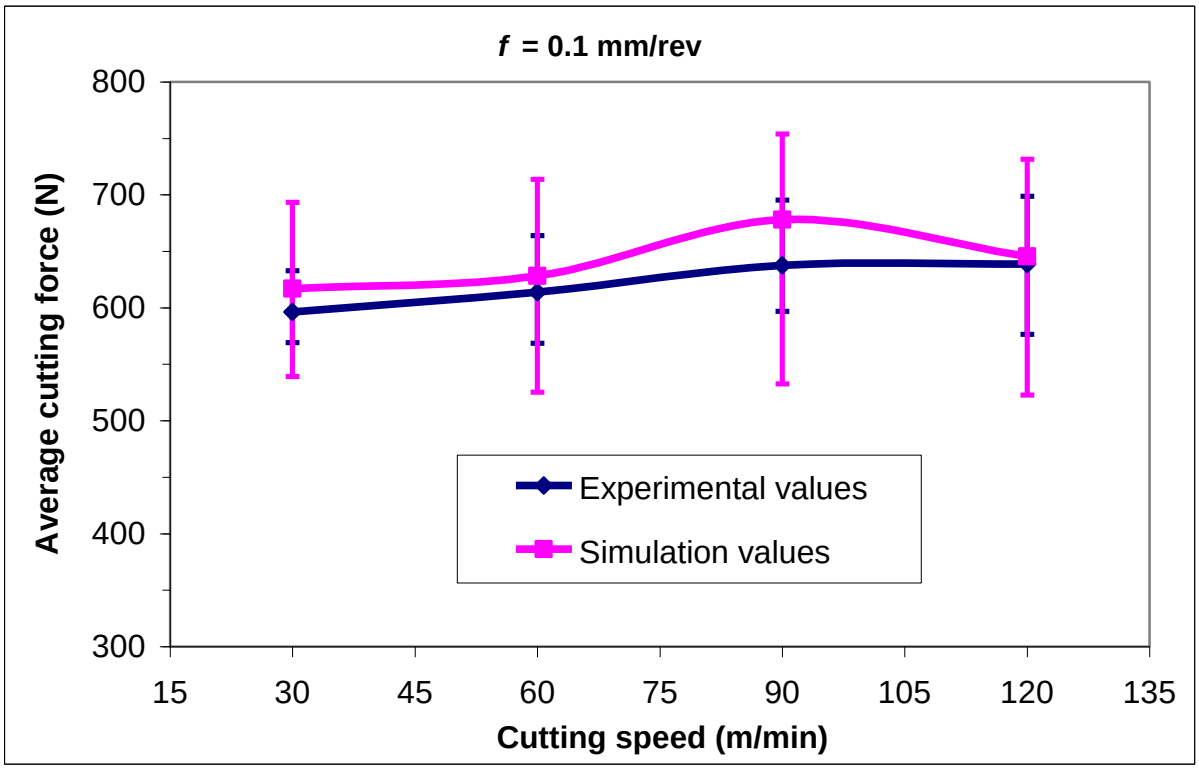

Fig. 4.23 Experimental and numerical cutting forces vs. cutting speed (f = 0.1 mm/rev, a_p = 3mm)

4.4.2.2 Feed rate effect on cutting force

Fig. 4.24 presents the evolution of cutting force when increasing the feed rate from 0.06 to 015 mm/rev with a constant cutting depth and cutting speed. A good agreement is found between numerical and experimental results except the high feed rate of 0.15 mm/rev. This can confirm that the adopted numerical approach is interesting and certainly can bring

physical comprehensions of the tool workpiece interaction and also can help to predict some output parameters such as cutting forces.

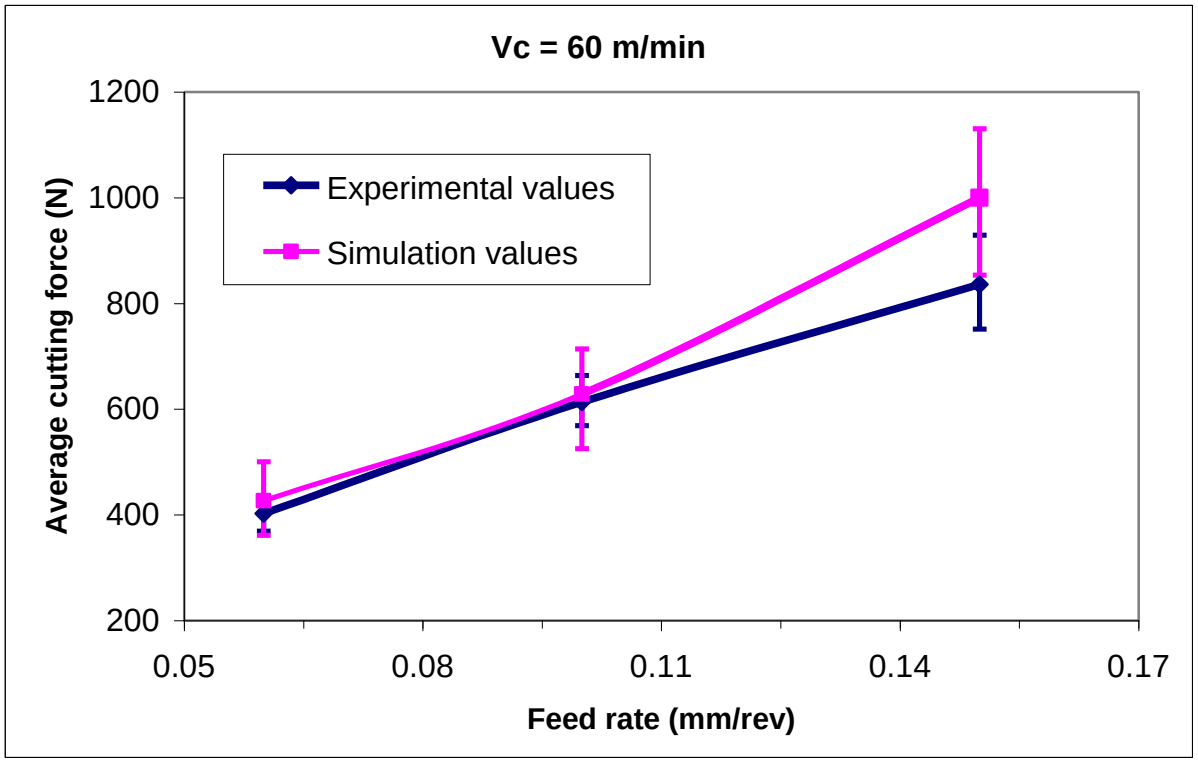

Fig. 4.24 Experimental and numerical cutting forces according to feed rate variation for (V_C = 60 m/min, a_p = 3mm)

4.4.3 PEEQ distribution based on MML cutting model

As the equivalent plastic deformation is one of the most important indicators to evaluate the thermal mechanical effect, and its value is directly related to damage settings for both intra-granular and inter-granular, parametric studies are discussed for different cutting speeds and feed rates.

4.4.3.1 PEEQ distribution with different cutting speeds

To well compare the PEEQ distribution, the machined part which can characterize GOA distribution is extracted for different cutting speeds as presented in the pink square in Fig. 4.25. Wherein the same GOA is arranged in the same column with the distribution of 30°, 0°, 30°, 45°, 60°, 45° from left to right.

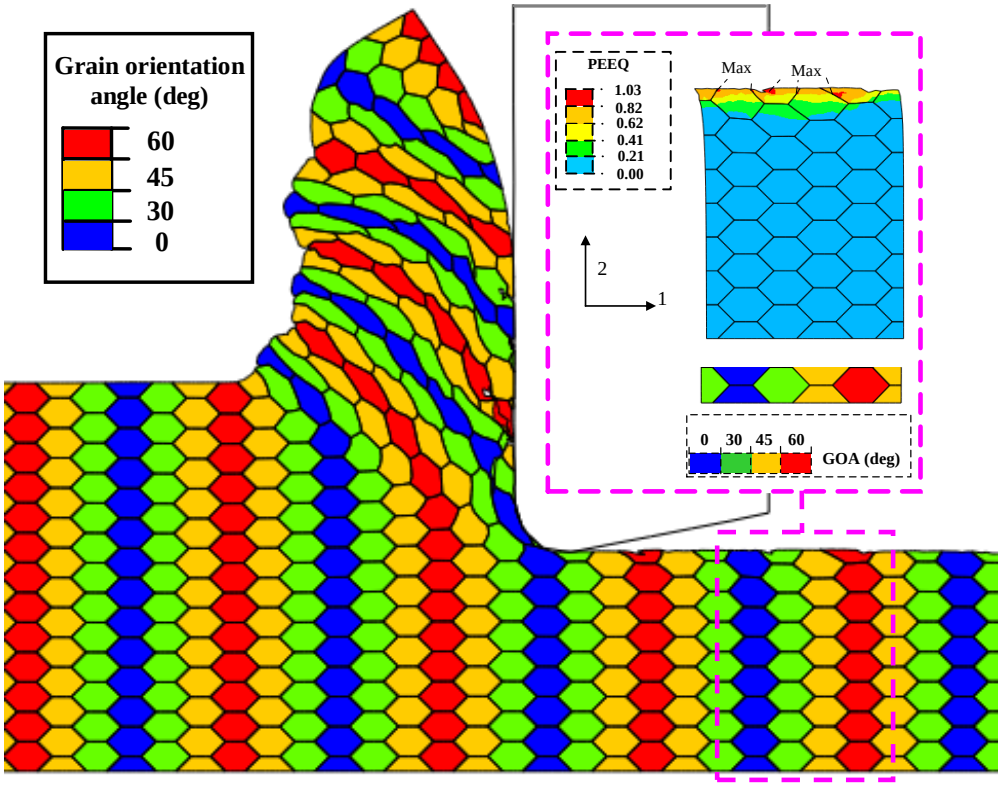

Fig. 4.25 The scheme of the extracted part for PEEQ analysis

For the low cutting speed V_c = 30 m/min, micro burr and micro pit appear at the machined surface generated by intra-granular damage, and the maximum values locate at the intra-granular damage induced defect or the interface between grains, the latter is mainly cased by the heterogeneity of the different GOA. With the increased cutting speed V_c = 60 m/min shows the lowest equivalent plastic strain and the smoothest surface, while the maximum values still locate at the intra-granular damage induced defect or the interface between grains. With further increased cutting speed V_c = 120 m/min, this phenomenon is more obviously, and the micro defect between grain interfaces is found. So, maybe we can say that the increased cutting speed can produce the smoother surface, while it will also introduce the micro defect caused by inter-granular damage beneath the machined surface.

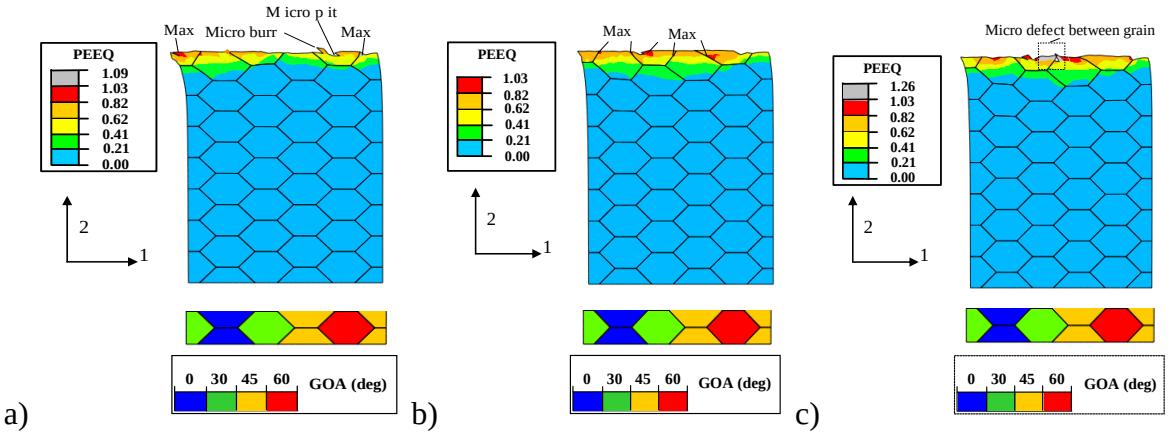

Fig. 4.26 Equivalent plastic strain distribution with fixed GOA and f = 0.1 mm/rev, a) V_c = 30 m/min, b) V_c = 60 m/min, c) V_c = 120m/min

4.4.3.2 PEEQ distribution with different feed rates

Similar to cutting speed study, different feed rates with 0.06 mm/rev, 0.1 mm/rev, 0.15 mm/rev are adopted here for a certain selected part which can cover the concerned GOAs (Fig. 4.27).

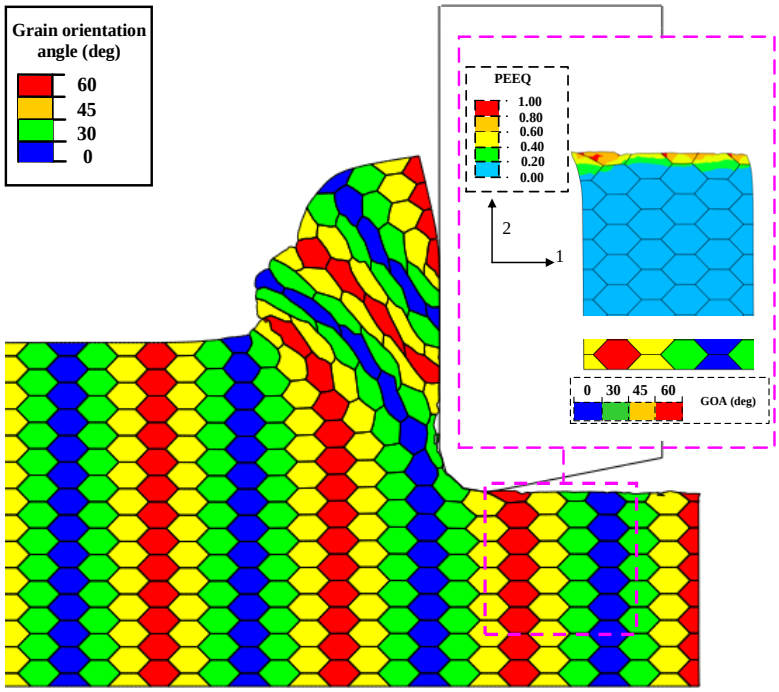

Fig. 4.27 The scheme of the extracted part for PEEQ analysis

In this section, different feed rates are considered to check the influence of the equivalent plastic strain distribution. For the small feed rate 0.06 mm/rev and 0.1 mm/rev, smooth surfaces are given, and the maximum PEEQ mainly distribute at the machined surface obtained by intra-granular damage and grain interface, which is similar to the case of

parametric study of cutting speed. It can be also seen that the highest feed rate of f = 0.15 mm/rev shows the largest PEEQs which locate at the machined surface, and produces the roughest surface, wherein both the micro burr and micro pit are found on the surface. Additionally, all the regions with the PEEQ value larger than 0.20 are located at the first layer grains.

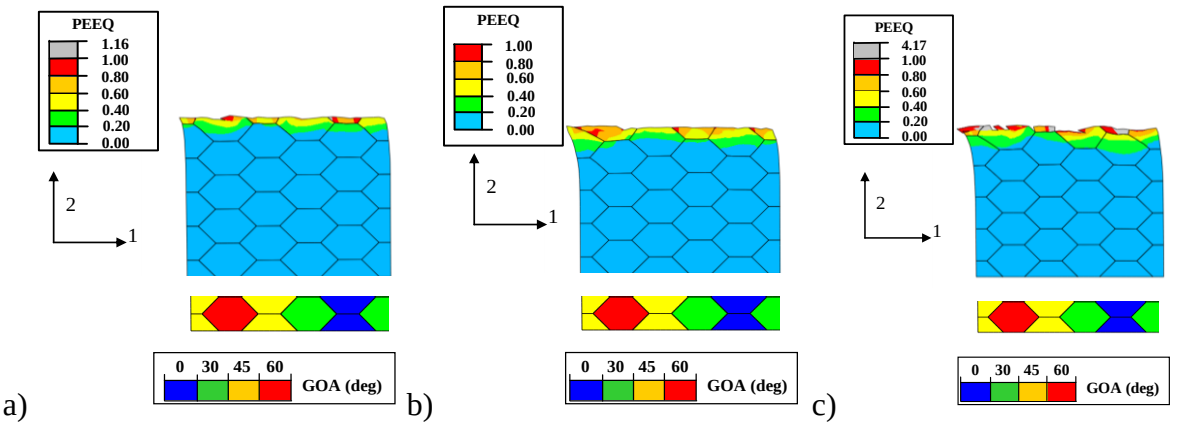

Fig. 4.28 Equivalent plastic strain with fixed GOA and V_c = 60 m/min, a) f = 0.06 mm/rev, f = 0.1 mm/rev, c) f = 0.15 mm/rev

4.4.4 Temperature distribution based on MML cutting model

As temperature distribution on the machined workpiece is one of the most important factors which influence the surface integrity, especially for the RS distribution, it is studied in this section under fixed GOA with different cutting speeds and feed rates, and the same selected parts as described in section 4.41 are adopted for the parametric study for different cutting speeds and feed rates.

4.4.4.1 Temperature distribution with different cutting speeds

Temperature distributions on the selected part for different cutting speed are presented in Fig. 4.29. From the general idea, the temperature increases with the increased cutting speed, and the affected regions with temperature above 80°C locate within one and half grains in direction 2, while the regions with temperature above 135°C are just limited to one layer grain for all the conditions. So, the concerns should focuses on the top layer grain for later parametric study. Concerning to the local part, the influence of GOA is not much, while the maximum temperature usually locates at the new formed grain induced by intra-granular damage for each cutting speed.

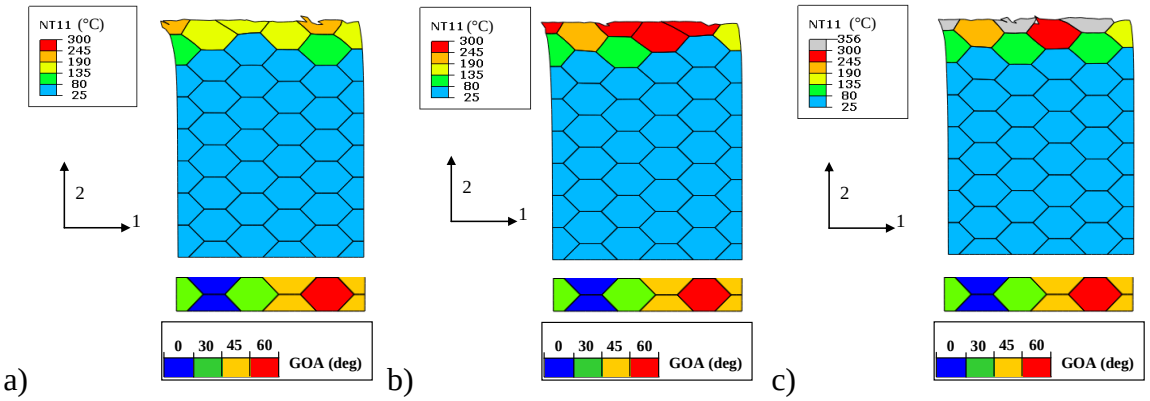

Fig. 4.29 Temperature distribution with fixed GOA and f = 0.1 mm/rev, a) V_c = 30 m/min, b) V_c = 60 m/min, c) V_c = 120m/min

4.4.4.2 Temperature distribution with different feed rates

It can be seen that feed rate f = 0.1 mm/rev shows the lowest temperature, the temperature region from 183°C to 295°C present in the first layer grain. For the smallest feed rate f = 0.06 mm/rev, the temperature distribution on the first layer grain varies between 187 and 295°C which is larger than the case of feed rate f = 0.1 mm/rev, even with smaller feed rate. Furthermore, it should be mentioned that all the highest temperature of the surface is caused by intra-granular damage effect. The highest temperature appears for the case of f = 0.15 mm/rev with the range from 295°C to 562°C for the highly thermal mechanical effect. Again, the GOA effect is not obviously. Nevertheless, all the high temperatures still locate within 2 layer grains (larger than 79°C) for all the feed rates.

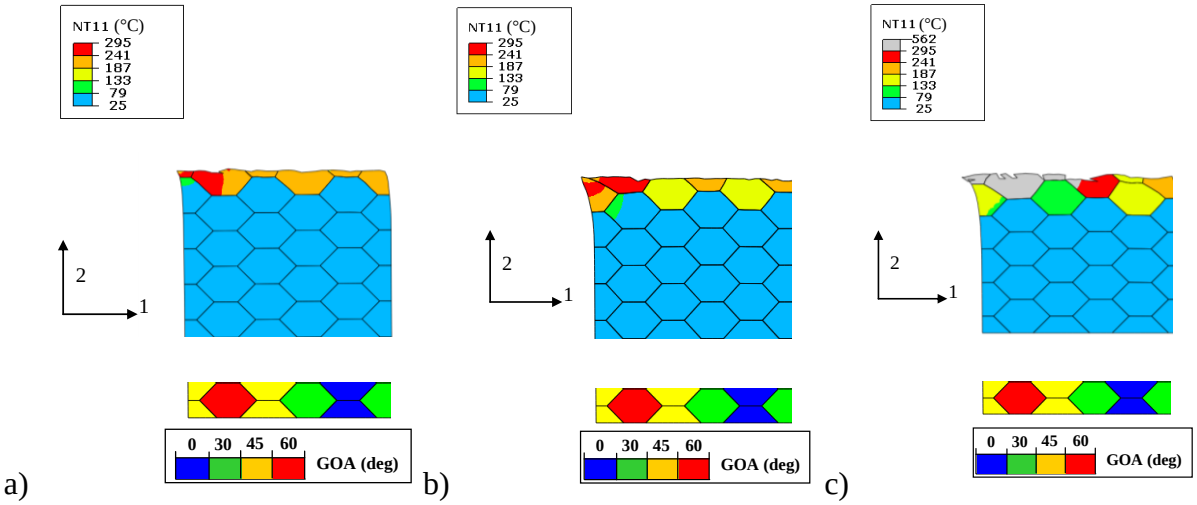

Fig. 4.30 Temperature distribution with fixed GOA and V_c = 60 m/min, a) f = 0.06 mm/rev, f = 0.1 mm/rev, c) f = 0.15 mm/rev

4.4.5 RS distribution based on MML cutting model

Concerning the residual stress (RS) prediction for the machining case, only average value can be given for the conventional methods, even the chip segmentation effect can be captured in the local surface as described by Zhang et al. [ZHA11]. As a result, more detailed information can't be obtained due to the limitation of tradition cutting model. So, this section focuses on the influence of GOA on RS distribution.

It is well known that significant thermal effects result in tensile RS while primarily mechanical effects contribute to compressive RS as well stated by Okushima and Kakino [OKU72]. So, the final RS is the result of the competition of thermal and mechanical effects. To well understand the RS distribution, three distinct regions are divided for the workpiece following the work of Jacobus et al. [JAC00]: region I corresponds to the surface and near-surface layers of the workpiece where mechanical and thermal effects are significant, and there is the sudden change of the stress distribution between near-surface and subsurface. Region II represents the subsurface layer where the machining-induced RSs are purely of a mechanical origin. Region III represents the remainder of the workpiece where the stresses are mainly used to balance above two regions (Fig. 4.31).

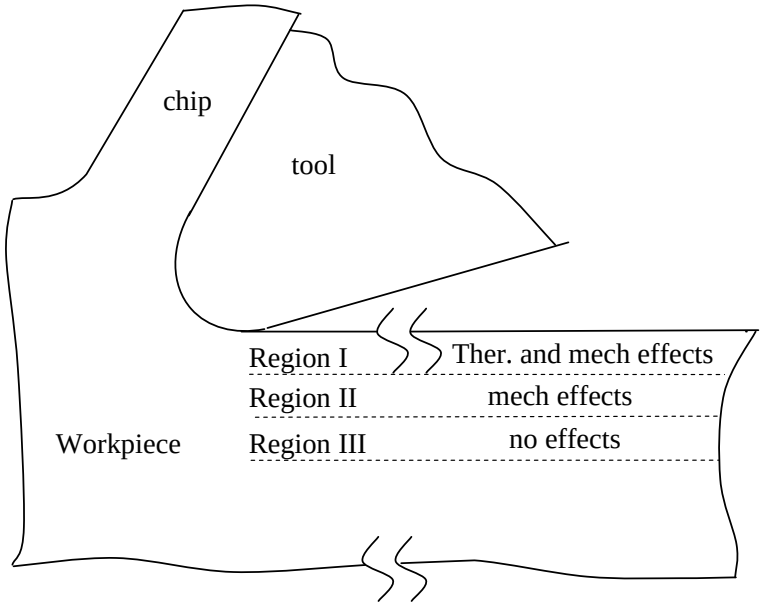

Fig. 4.31 Schematic model for the thermal mechanical effect on RS distribution

4.4.5.1 RS distribution with different cutting speeds

In this subsection, three different cutting speeds are tested to check the effect of cutting speed on residual distribution as presented from Fig. 4.34 to Fig. 4.36. To better and obviously observe the effect of GOA, large discrete angles with 0°, 30°, 45°, 60° are still arranged for workpiece in every cutting speed test, and their individual and average influences on RS distribution are checked, meaning while the correspondingly machined surface where RSs are extracted is also given.

The macro average RS distribution (this is the average value of RS distribution for all the four different orientation angles, as presented from Fig. 4.34 to Fig. 4.36) are addressed firstly in Fig. 4.32. In order to uniform the comparison, region I is considered as the depth of one grain (18 μm), region II is dealt with the continuous depth until zero compressive stress, and the left part is the region III.

As 0° rake angle for cutting tool is adopted here, the strong mechanical effect usually dominates even for low cutting speed V_c = 30 m/min, which induces the compressive RS for the cut surface and the near-surface (region I), and subsurface (region II). When cutting speed increases to 90 m/min, both thermal and mechanical effect increase for the machined work piece: wherein, the surface and near-surface RS distribution don't change compared with cutting speed 30 m/min due to the equivalent increment of thermal and mechanical effects, while subsurface compressive RS increases dues to the domination of mechanical effect. With continuous increased cutting speed, the surface and near-surface compressive RS start to decrease because of the dominated thermal effect, even the mechanical effect increases too. On the contrary, the subsurface compressive stress enhances for the pure increased mechanical effect.

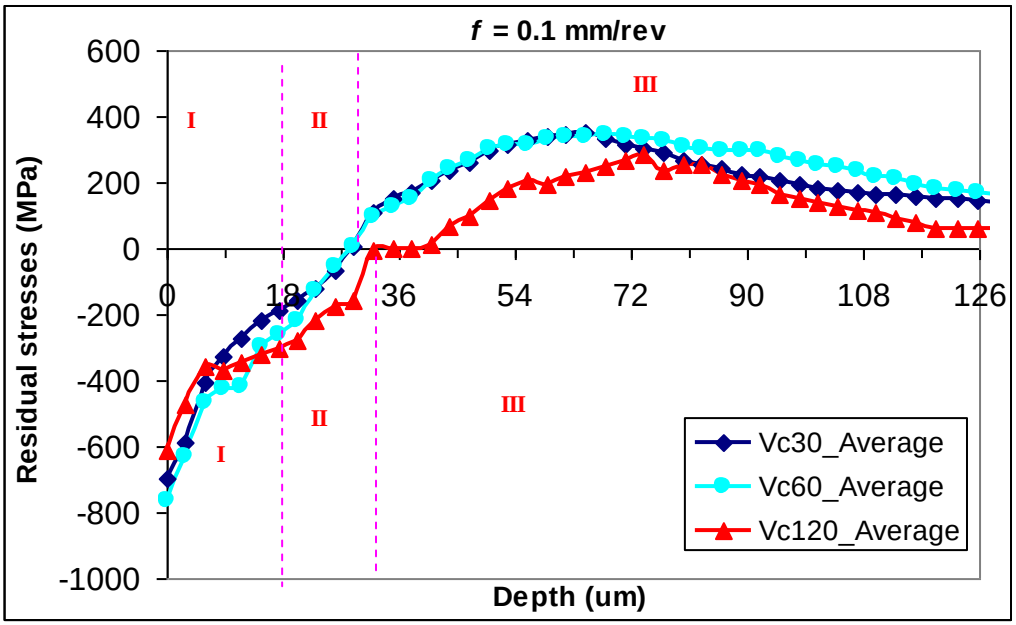

Fig. 4.32 Average RS distribution in circumferential direction for various cutting speeds with f = 0.1 mm/rev

As the mechanical effect of the circumferential RS (direction 1) is mainly dependent on the shear direction load, a single shear load test is preformed to understand the mechanical behavior of different GOA for one single square element with the edge size of 30 μm. Finally, the true stress vs strain curve in direction 1 is presented in Fig. 4.33. It can be seen that these crystal slip systems of grains with 0° and 30° orientation angles are easier to be activated in the form of plastic deformation compared with that of grains with 45° and 60° orientation angles. Noted that 90% of the plastic energy are converted to heat source is dealt with in the program, and then the correspondingly thermal strain will be produced too, which will produce tensile RS to compete with beneficial compressive stress.

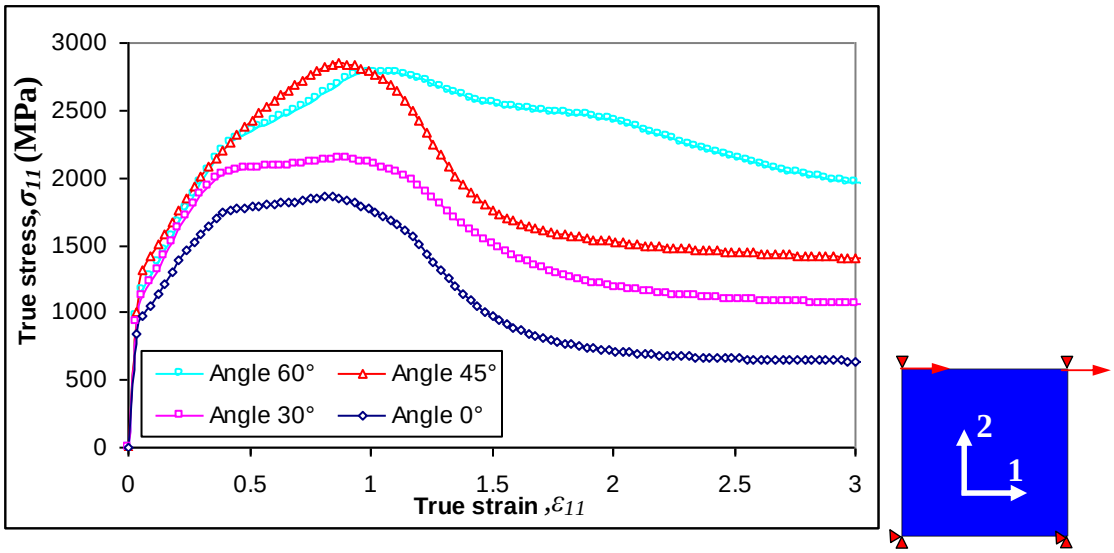

Fig. 4.33 Single element shear test with constant strain rate 2000 s^{-1} for different orientation angles with initial temperature 25°C.

Concerning the influence of GOA on RS distribution: For the low cutting speed V_c = 30 m/min, RSs at surface and near-surface for 0° and 30° orientation angle are lower than the cases for 45° and 60°, but they are inversed for the subsurface RS distribution, which means that the slip systems are hard to be activated for 45° and 60° orientation angles, and this condition is considered as the comparison benchmark evaluation for the later two cutting speeds. With increased cutting speed V_c = 60 m/min, the increased mechanical effect dominates for 0° and 30° while the increased thermal effect majors in the case of 45° and 60° for region I and II compared with V_c = 30 m/min. For the further increased cutting speed V_c = 120 m/min, the surface RS decreases for all the orientation angles, and the RS distributions show serious fluctuation in both region I and II, while the subsurface zone prolongs for all the orientation angles. It seems that V_c = 120 m/min is one critical cutting speed to affect the RS distribution for orientation angle, this is also presented for the average RS distribution in previous Fig. 4.32. Apart from this, the micro defect is observed below machined surface between grain interfaces as illustrated by dashed line (Fig. 4.26 c)). Generally speaking, orientation angles of 30° and 45° show better RS distribution compared with the case for angles of 0° and 60°.

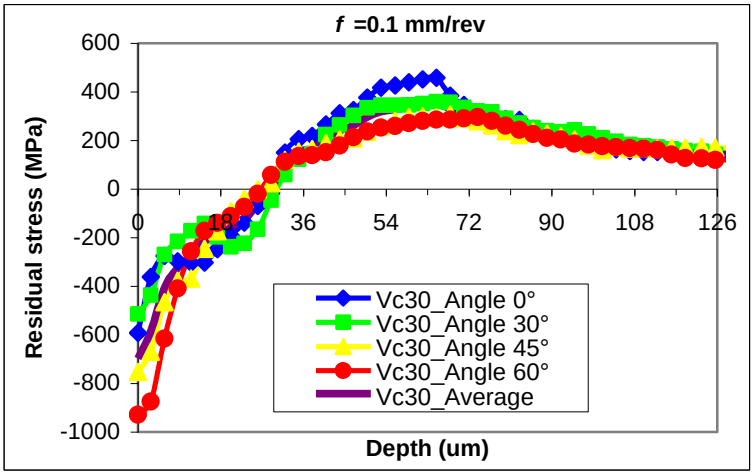

Fig. 4.34 RS profile on circumferential direction, V_c = 30 m/min and f = 0.1 mm/rev

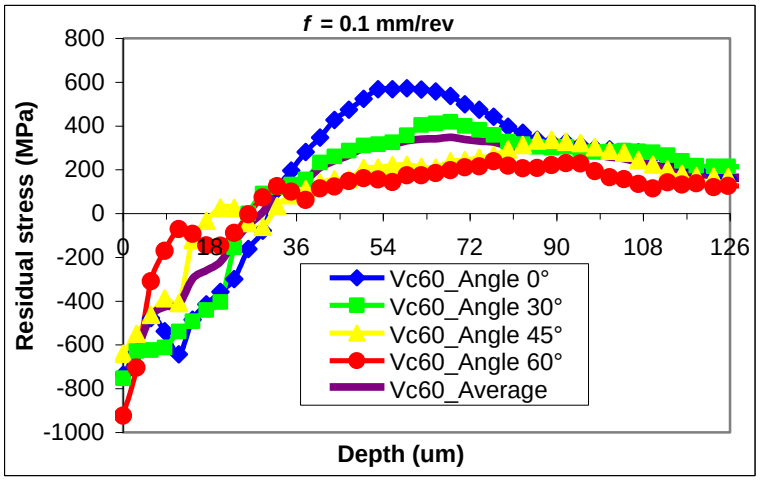

Fig. 4.35 RS profile on circumferential direction, V_c = 60 m/min and f = 0.1 mm/rev

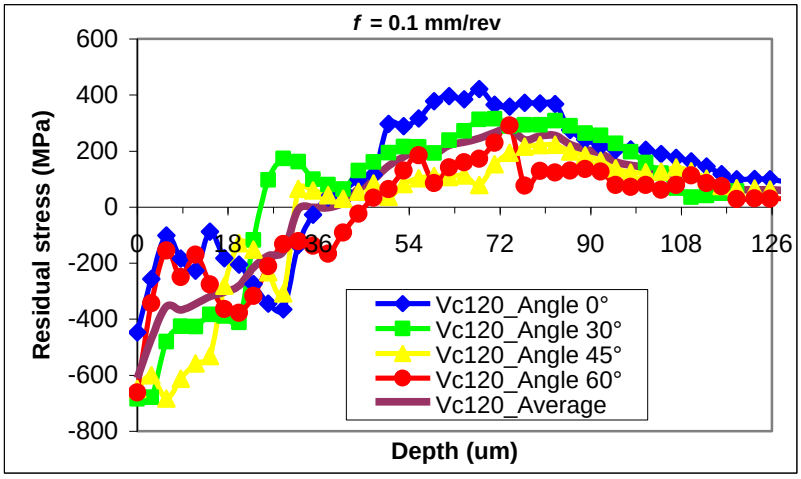

Fig. 4.36 RS profile on circumferential direction, V_c = 120 m/min and f = 0.1 mm/rev

Additionally, it is also found that the intra-granular damage usually induces micro burr and crater on the surface, while inter-granular damage always generates smooth surface. So, if the original workpiece contains very fine grains or produces fine grains during the machining process, more possibilities of the chip/workpiece separation will occur at the grain interface, which can bring the satisfied the surface integrity.

4.4.5.2 RS distribution with different feed rates

Besides cutting speed the feed rate is also one of the important factors that determine surface integrity. So, different feed rates are considered to study the influence of GOA for RS distribution with constant cutting speed V_c = 60 m/min.

Similar to previous section, the average GOA influence is checked for different feed rates (Fig. 4.37). The compressive RS distributions in region I increase when feed rate varies from 0.06 mm/rev to 0.1 mm/rev, while the region II is not influenced. For continuous increment of feed rate to 0.15 mm/min, the surface RS greatly decreases because of the dominated thermal effect, while the RS in subsurface, i.e. region II, increases and prolongs the influencing depth up to 54 μm.

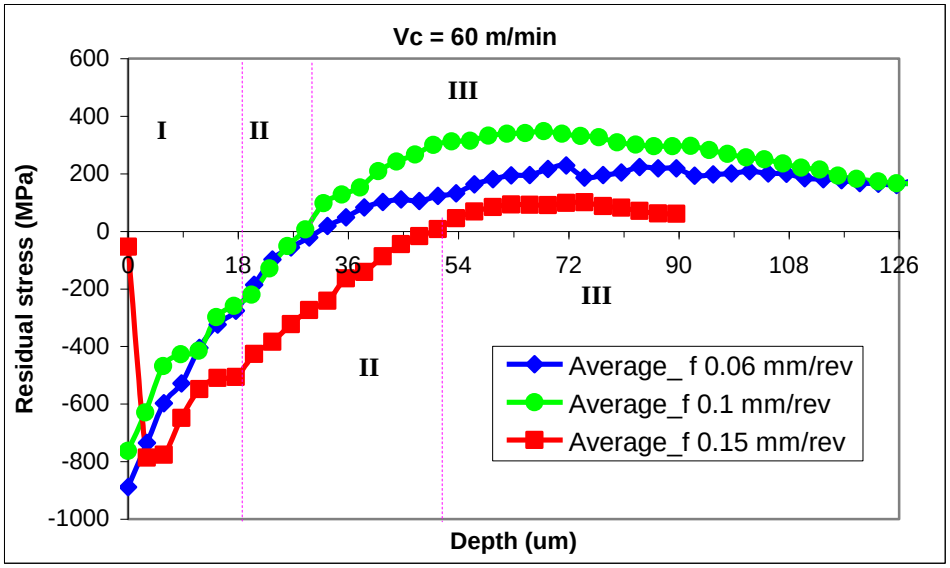

Fig. 4.37 Average RS distribution in circumferential direction for various feed rates with cutting speed V_c = 60 m/min.

Concerning the separate GOA influence, orientation 30° shows the best RS distribution compared with other GOA s for the feed rate 0.06 mm/rev (Fig. 4.38). With increased feed rate 0.1 mm/min, the RS decreases on the surface and increases in near-surface and

subsurface zone for GOA 30°. While this is totally inversed for GOA 60°, the influence for the other orientation angle is not obvious (Fig. 4.39). When the feed rate increases to 0.15 mm/rev, the surface RS present the tendency to positive values, and the value for GOA 30° approaches to 200 MP (Fig. 4.40). However, the RS distribution on subsurface (region II) shows the best in all of the three feed rates for all the GOA s, which is obviously caused by the dominated mechanical effect.

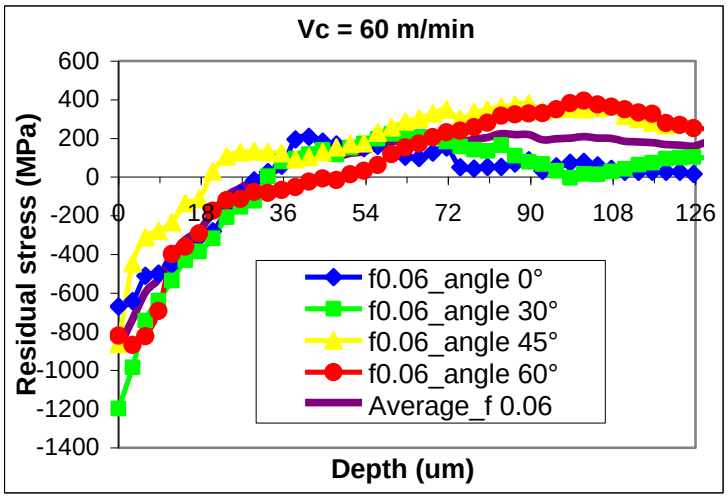

Fig. 4.38 RS profile on circumferential direction for f = 0.06 mm/rev and V_c = 60 m/min

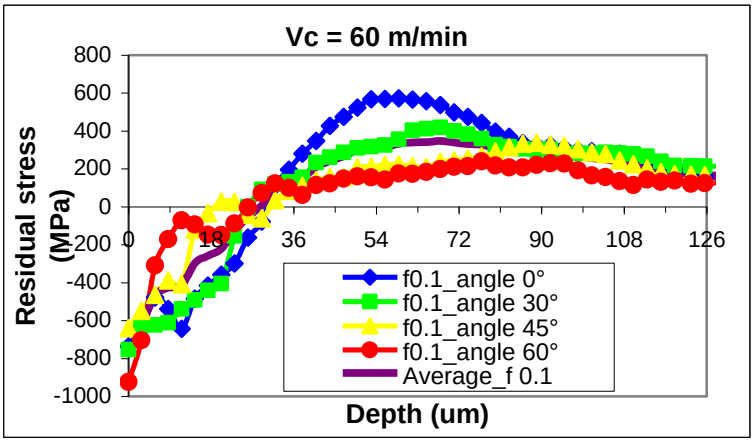

Fig. 4.39 RS profile on circumferential direction for f = 0.1 mm/rev and V_c = 60 m/min

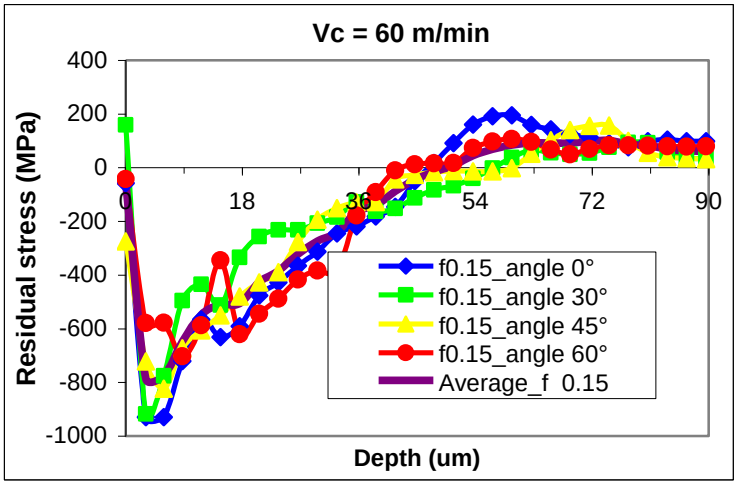

Fig. 4.40 RS profile on circumferential direction for f = 0.15 mm/rev and V_c = 60 m/min

Overall, without considering the positive RS for GOA 30° in the case of feed rate 0.15 mm/rev, GOA 30° and 45° still show good RS distribution. Taking into account the machined surface, inter-granular damage still presents the smoother surface which shows the same phenomena compared to section 4.2.

4.5 Conclusion:

An orthogonal cutting model concerning the material microstructure-level (MML) is proposed. To model the material degradation process yielding to chip formation, the intra-granular damage model (based on crystallographic slip in the grains) and the inter-granular damage model (formalized by zero thickness discrete cohesive elements) were developed and implemented with user subroutines in Abaqus/Explicit. The main steps accompanying the elaboration of this MML cutting model concern firstly the consideration of the cut material behavior at the crystallographic level. The second step treats the average material behavior at the grain level. Finally, the bulk material behavior was considered. The cutting of Titanium alloy Ti–6Al–4V, ideally organized into hexagonal primary α phase, was investigated to illustrate the capabilities of the proposed model.

-.Thanks to this model, the genesis of chip morphology is better understood. The chip formation mechanism is described by shear slip between grain and crystallographic slip within the grains. The influence of the GOA on the segmentation of chip is outlined. It is found that chip peaks are usually located near "soft phase" grains, while the chip valleys usually appear for "hard phase" grains.

-.Besides, based on this study it can be said that from experimental point of view the segmentation periodicity of chip in the case of the cutting of the Titanium alloy Ti–6Al–4V cannot be really regular due the hazardous distribution of the GOAs. Moreover, it was shown that the higher is the cutting speed, more pronounced are both the segmented chip and micro-defects at its back. Similar to the phenomena of the cutting speed study, meanwhile, more segmented chip and micro-defects at chip back are also found with increased feed rate.

-. Additionally, the cutting force prediction based on MML cutting model is well verified by experimental ones for different cutting speed and feed rate, and it found that the model is not suitable for high feed rate larger than 0.15 mm/rev.

- The PEEQ is directly related to damage, which pilots the occurrence of micro defects at the new formed surface and between grain interfaces. It is found that higher cutting speed generate smoother surface, while introduce the defect between grain interfaces. On the contrary, higher feed can bring more micro burr at the machined surface.

- For the temperature study, it is observed that the temperature increases with high cutting speed and high feed rate, while the highest temperature always locates at the intra-granular generated surface. Additionally, the temperature distribution with the region more than 80°C are limited with two lay grains for all the cutting speeds and feed rates investigated.

- Various cutting speeds and feed rates are considered to study the effect of GOA on the RS distribution in the machined workpiece, the simulation shows that orientation angles of 30° and 45° always lead to higher levels of compressive RS distribution which gives insight for material production for high quality machining. At the same time, a cutting speed lower than 120 m/min and a feed rate smaller than 0.15 mm/rev, respectively, are recommended here to get good surface integrity.

The main disadvantage of this method is that no direct material GOA can be obtained for comparison with experimental cutting is possible at present, as there is no real-word material conforming to the parameters used here. Nevertheless, this method allows understanding the reasons for the chip segmentation and surface defects from new aspects, and can be extended to other material cutting prediction.

5 Conclusions and future work

In this research work, numerical simulation approaches and methodologies dictated for multi-physic comprehensions of titanium alloy (Ti–6Al–4V) cutting are presented. Wherein, the bulk material level and material microstructure level (MML) cutting model are developed, and their results in terms of chip formation process and surface integrity are discussed correspondingly.

The important findings made were built up mainly on two cutting model elaborations:

i) Traditional bulk material level cutting model

The macro scale cutting model in bulk material level was developed based on the traditional strain-rate and temperature dependent visco-plastic Johnson Cook constitutive law. This phenomenological material behavior is suitable for problems where strain rates vary over a large range (10^2 to 10^6 s^{-1}). In this cutting model, Hillerborg's fracture energy was adopted for controlling material stiffness degradation process allowing to capture the shear strain localization and producing the segmented chip formation. Also, the frictional contact model was improved from the aspect of the contact mechanics with various coefficients of friction (CoF) and elaborated by considering the influence of temperature on limiting shear stress at the tool/chip interface. This reliable model has the capability to simulate the cutting process even with high coefficient of friction (CoF) and with large cutting edge radius. This model has allowed carrying out parametric studies, confirming the robustness of the proposed model. The numerical results were validated experimentally.

Besides, a methodology allowing residual stress (RS) prediction model of the machined workpiece was also developed. More accurately, it was shown that the segmented chip reflection can affect the RS distribution.

ii) Material Microstructure-level cutting model (MML cutting model)

Based on the crystal viscoplasticity approach, a material microstructure-level cutting model (MML cutting model) was developed in order to account for the microstructure of Ti–6Al–4V. The model includes distinct slip geometry for each grain, anisotropic strengths of different slip families, and different orientation angles.

To capture the material stiffness degradation process, two types of damage laws were introduced. Zero thickness cohesive elements (inter-granular element) were adopted to link with grain interfaces, while the crystallographic scale was used to characterise the intra-granular damage model and consequently to simulate the stiffness degradation process within a grain. Moreover, the delayed damage model was utilized to reduce the mesh dependent problems. Finally, the coupled intra- and inter-granular damage were successfully used in the MML cutting model, which is able to simulate the surface micro scale defect of the machined surface in grains and between them. Besides, the chip formation mechanism is described by shear slip between grains and crystallographic slip in the grains. It was established that "chip peak" and "chip valley" are related to "soft phase" and "hard phase" in this microstructure considered simulation model.

To study the influence of MML cutting model for the integrity of the machined workpiece, the equivalent plastic strain (PEEQ), temperature and residual stress (RS) distributions on the machined workpiece were studied for different cutting speeds and feed rates, the main results are summarized as following:

- The PEEQ is directly related to damage, which pilots the occurrence of the micro defects at the new formed surface and between grain interfaces. It is found that the higher is the cutting speed, the smoother is the predicted cut surface and the more is the defect between grain interfaces for the subsurface. On the contrary, higher is the feed rate, more are the micro burrs on the machined surface.

- It is observed that the temperature increases with both high cutting speed and feed rate, while the highest temperature is always located at the intra-granular generated surface. Additionally, the region where temperature distribution is higher than 80°C are limited within two lay grains for all the cutting speeds and feed rates investigated.

- Various cutting speeds and feed rates were considered to study the effect of the grain orientation angle on the RS distribution in the machined workpiece. The simulation shows that orientation angles of 30° and 45° lead to higher levels of compressive RS than for angles ranging from 0 to 60 degrees. At the same time, a cutting speed lower than 120 m/min and a feed rate smaller than 0.15 mm/rev, respectively, are recommended here to improve the surface integrity.

Recommendations for future work

The present work has clearly demonstrated that the cut material heterogeneities when viewed at the microstructure-level are important parameters to consider in problems with plastic deformation at micro scale such as micro-cutting. The focus of this thesis is mainly centred on how the chip morphology and the RS distribution are affected by the grain orientation angle (GOA). Consequently, the insights and results obtained indicate that further research on the cutting process using physically-based micromechanical models is warranted. In light of what has been evoked in the current work, there are two main areas in which future research efforts should be performed: *i)* improvement of the physics of the constitutive material model and MML cutting model and *ii)* refinement of the FE cutting model to more closely reflect experimental conditions, including the build up of a 3D model.

i) Constitutive material modeling

The present crystal viscoplastic model for primary α phase of Ti–6Al–4V presented in this thesis includes many sources of microstructural heterogeneity. However, it is still open for refinements of the flow rule and the corresponding equations of the internal state variable (ISV) evolution. Modifications and improvements are summarized below:

- Include the dislocation density and dependence of microstructural length scale parameters in the ISV evolution equations, and rewrite the flow rule in the form of the OROWAN equation:

$$\dot{\gamma} = \rho_m b v + \dot{\rho}_m b l \tag{5.1}$$

  where ρ_m is the mobile dislocation density, b is the burgers vector, v is the mean dislocation velocity, and l is the characteristic dislocation spacing.

- Incorporate a more thorough treatment of the dislocation mechanism responsible for deformation in the lamellar regions as more experimental evidence becomes available [SAV04].

- Re-determine the slip system flow exponent from macroscopic stress strain data based on the above new definition.
- The implementation of the constitutive model for zero thickness cohesive elements should be improved too, to meet the real engineering applications, based on experimental calibration.
- Thermal effect is not included into the present cohesive element, the user element coupled with temperature should be considered for the next step.

ii) Towards a FE multi-physical cutting model

The FE cutting models elaborated during this thesis correspond to the highly idealized 2D plane strain problem in case of orthogonal cutting. Consequently, the simulation results are limited to predict the chip formation and surface integrity within 2D. In future work, we are firmly convinced that a significant effort should be devoted to develop more detailed descriptions of the machined material and cutting process in order to capture the conditions of practical experiment. So, a list of items that should be considered for next generation FE multi-physical cutting models can be summarized below:

- In our conviction, 2D cutting model is not enough for modeling the orthogonal cutting simulation. The multi-phase structure with a 3D model of the workpiece should be considered next.
- As the more important features of the cohesive and crystal plasticity constitutive models are implemented with user subroutines, the calculation time increases more than five or six times compared with traditional model. So, a new algorithm that will allow fast calculation should be considered.
- Another important assumption is that phase transformation is not considered in the present study, this must be considered in the next steps in link with plasticity at the microstructure level.
- Several methods can be used to measure the local orientations of a microstructure. Among them the Electron Back Scattered Diffraction, (EBSD), seems to be a powerful device to measure the crystallographic orientations and the distribution of phases, the distribution of the inter-granular interface etc. Such equipment could be used to feed numerical models and, consequently, help effectively to better apprehend the role of crystal plasticity in cutting processes.

References

[ABA10] **ABAQUS/EXPLICIT** Theory and user manuals. Version 6.7.1, 2007.

[ALL97] **ALLIX O** and **DEÜ J F**. Delay-damage modelling for fracture prediction of laminated composites under dynamic loading. Eng. Trans., 1997, 45, 29-46.

[ALL99] **ALLIX O**, **DEU J F** and **LADEVÈZE P**. A delay damage meso-model for prediction of localization and fracture of laminates subjected to high rate loading. 1999, ECCM 99.

[ANK80] **ANKEM S** and **MARGOLIN H.** The role of elastic interaction stresses on the onset of plastic flow for oriented two ductile phase structures. Metallurgical and Materials Transactions A, 1980, 11(6), 963–972.

[ARR05] **ARRAZOLA P J**, **UGARTE D**, **MONTOYA J**, **VILLAR A,** and **MARYA S**. Finite element modeling of chip formation process with Abaqus/explicit^{TM} 6.3. In: Proceedings of VIII International Conference on Computational Plasticity. CIMNE, Barcelona, 2005.

[ARR09] **ARRAZOLA P J**, **GARAY A, IRIARTE L M, ARMENDIA M, MARYA S**, and **LE MAÎTRE F**. Machinability of titanium alloys (Ti–6Al–4V and Ti555.3). Journal of Materials Processing Technology, 2009, 209 (5), 2223–2230.

[ASA11] **ASAD M, MABROUKI T, GIRARDIN F, ZHANG Y**, and **RIGAL J F**. Towards a physical comprehension of material strengthening factors during macro to micro-scale milling. MECHANIKA, 2011, 17(1), 97-104.

[ASA11a] **ASAD M**. Elaboration of concepts and methodologies to study peripheral down – milling process from macro to micro scales. PhD thesis, INSA de Lyon, 2011.

[BAC52] **BACKER W R, MARSHALL E R,** and **SHAW M C**. The size effect in metal cutting. Transaction of ASME, 1952, 74, 61–72.

[BAD08] **BADU B.** Physically based model for plasticity and creep of Ti-6Al-4V. Licence thesis, Luleå University of Technology, Department of Applied Physics and Mechanical Engineering, 2008.

[BÄK03] **BÄKER M**. The influence of plastic properties on chip formation. Computational Materials Science, 2003, 28(3-4), 556–562.

[BÄK05] **BÄKER M**. Finite element investigation of the flow stress dependence of chip formation. Journal of Materials Processing Technology, 2005, 167(1), 1–13.

[BÄK06] **BÄKER M**. Finite element simulation of high-speed cutting forces. Journal of Materials Processing Technology, 2006, 176(1-3), 117–126.

[BAR62] **BARENBLATT G I**. The mathematical theory of equilibrium cracks in brittle fracture. 1962, 7, 55–129.

[BAR01] **BARRY J, BYRNE G,** and **LENNON D.** Observations on chip formation and acoustic emission in machining Ti-6Al-4V alloy. International Journal of Machine Tools and Manufacture, 2001, 41 (7), 1055–1070.

[BAR05] **BARGE M, HAMDI H, RECH J**, and **BERGHEAU J M**. Numerical modelling of orthogonal cutting: influence of numerical parameters. Journal of Materials Processing Technology, 2005, 164-165, 1148–1153.

[BON08] **BONNET C**, **VALIORGUE F, RECH J,** and **HAMDI H**. Improvement of the numerical modeling in orthogonal dry cutting of an AISI 316l stainless steel by the introduction of a new friction model. CIRP Journal of Manufacturing Science and Technology, 2008, 1(2), 114–118.

[BOU09] **BOUDIFA M, SAANOUNI K,** and **CHABOCHE J L**. A micromechanical model fro inelastic ductile damage prediction in polycrystalline metals for metal forming. International journal of mechanical sciences, 2009, 51, 453-464.

[BRI89] **BRINKSMEIER, E**. State-of-the-art of non-destructive measurement of sub-surface material properties and damages., Precision Engineering, 1989, 11 (4), 211-224.

[BRO03] **BROCKMAN R A**. Analysis of elastic-plastic deformation in tial polycrystals. International Journal of Plasticity, 2003, 19(10), 1749–1772.

[CAL07] **CALAMAZ M, COUPARD D, NOUARI M,** and **GIROT F.** A finite element model of high speed machining of ta6v titanium alloy. In: Proceedings of 6th international conference high speed machining, San Sebastian, Spain, 2007, (21–22).

[CAL08] **CALAMAZ M, COUPARD D,** and **GIROT F.** A new material model for 2D numerical simulation of serrated chip formation when machining titanium alloy

Ti-6Al-4V. International Journal of Machine Tools and Manufacture, 2008, 48 (3-4), 275–288.

[CAL09] **CALAMAZ M, LIMIDO J, NOUARI M, ESPINOSA C, COUPARD D, SALAÜN M, GIROT F,** and **CHIERAGATTI R**. Toward a better understanding of tool wear effect through a comparison between experiments and SPH numerical modelling of machining hard materials. Int. Journal of Refractory Metals & Hard Materials, 2009, 27, 595–604.

[CAS07] **CASTANY P, PETTINARI-STURMEL F, CRESTOU J, DOUIN J,** and **COUJOU A**. Experimental study of dislocation mobility in a Ti-6Al-4V alloy. Acta Materialia, 2007, 55(18), 6284–6291.

[CER99] **CERETTI E, LUCCHI M,** and **ALTAN T.** FEM simulation of orthogonal cutting: serrated chip formation. J. Mater. Processing Technol., 1999, 95(13), 17–26.

[CHA02] **CHANDRA N, LI H, SHET C,** and **GHONEM H**. Some issues in the application of cohesive zone models for metal-ceramic interfaces. International journal of Solids and Structures, 2002, 39, 2827-2855.

[CHE04] **CHEN L, EL-WARDANY TI,** and **HARRIS WC**. Modeling the effects of flank wear land and chip formation on residual stresses, CIRPAnnals—Manufacturing Technology, 2004, 53(1), 95–98.

[CHI06] **CHILDS T H C.** Friction modelling in metal cutting. Wear, 2006, 260 (3), 310–318.

[CHU02] **CHUZHOY L, DEVOR R E, KAPOOR S G,** and **BAMMANN D J**. Microstructure-level modeling of ductile iron machining. Journal of Manufacturing Science and Engineering, 2002, 124(2), 162–169.

[CHU03A] **CHUZHOY L, DEVOR R E, KAPOOR S G, BEAUDOIN A J**, and **BAMMANN D J**. Machining simulation of ductile iron and its constituents, part 1: Estimation of material model parameters and their validation. Journal of Manufacturing Science and Engineering, 2003, 125(2), 181–191.

[CHU03B] **CHUZHOY L, DEVOR R E,** and **KAPOOR S G**. Machining simulation of ductile iron and its constituents, part 2: Numerical simulation and experimental

validation of machining. Journal of Manufacturing Science and Engineering, 2003, 125(2), 192–201.

[CLA05] **CLAYTON J D**. Dynamic Plasticity and Fracture in High Density Polycrystals: Constitutive Modeling and Numerical Simulation. Journal of Mechanics and Physics of solids, 2005, 53, 261-301.

[DIC06] **DICK T** and **CAILLETAUD G**. Fretting modelling with a crystal plasticity model of Ti6Al4V. Computational Materials Science, 2006, 38, 113-125.

[DIN01] **DINESH D, SWAMINATHAN S, CHANDRASEKAR S,** and **FARRIS T N**. An intrinsic size effect in machining due to the strain gradient. In: Proceedings of ASME IMECE, 2001, 197–204.

[DIR01] **DIRIKOLU M H, CHILDS T H C,** and **MAEKAWA K**. Finite element simulation of chip flow in metal machining. International Journal of Mechanical Sciences, 2001, 43(11), 2699–2713.

[DUG60] **DUGDALE D S**. Yielding of steel sheets containing slits. Journal of the Mechanics and Physics of Solids, 1960, 8(2), 100–104.

[EZU97] **EZUGWU E O** and **WANG Z M**. Titanium alloys and their machinability—a review. J Mater Process Technol, 1997, 68, 262–274.

[ESP03] **ESPINOSA H D** and **ZAVATTIERI P D**. A grain level model for the study of failure initiation and evolution in polycrystailline brittle materials Part I: Theory and numerical implementation. Mechanics of Materials 2003, 35, 333-364.

[EZU03] **EZUGWU E O, BONNEY J,** and **YAMANE Y**. An overview of the machinability of aeroengine alloys. J. Mater. Process. Technol., 2003, 134, 233-235.

[EZU09] **EZUGWU E O, BONNEY J, D A SILVA R B, MACHADO A R,** and **UGWOHA E**. High productivity rough turning of Ti-6Al-4V alloy, with flood and high-pressure cooling. Tribology Transactions, 2009, 52 (3), 395–400.

[FIE72] **FIELD M, KAHLES J F** and **GAMMETT J T**. A review of measuring methods for surface integrity. Annals of the CIRP, 1972, 21(2), 219-238.

[FIE73] **FIELD, M.** Surface integrity - A new requirement for improving reliability of aerospace hardare. 18th Annual National SAMPE Symposium Los Angeles, April 3-5, 1973, California.

[FIL07] **FILICE L, MICARI F, SETTINERI L,** and **UMBRELLO D.** Wear modelling in mild steel orthogonal cutting when using uncoated carbide tools. Wear, 2007, 262 (5-6), 545–554.

[FRO82] **FROST H J and ASHBY M F.** Deformation-Mechanism Maps. Pergamon Press, Elmsford, 1982, 1-16.

[GIO88] **GIOVANOLA H.** Adiabatic shear banding under pure shear loading. Part II: Fractographic and metallographic observation. Mechanics of Materials, 1988, 7, 73–87.

[GOH06] **GOH C H, MCDOWELL D L,** and **NEU RW**. Characteristics of plastic deformation field in polycrystalline fretting contacts. Journal of the mechanics and physics of solids 2006, 54 (2), 340-367.

[GUO00] **GUO Y B** and **DORNFELD D A.** Finite element modeling of burr formation process in drilling 304 Stainless Steel. J. Mfg. Sci. Engng., 2000, 122(4), 612–619.

[GUO02] **GUO Y B** and **LIU C R**. 3D FEA modelling of hard turning. Journal of manufacturing science and engineering 2002, 124 (2), 189–199.

[GUO04] **GUO Y B.** A FEM study on mechanisms of discontinuous chip formation in hard turning. J. Mat. Proc. Tech., 2004, 155, 1350-1356.

[GUO06] **GUO Y B, WEN Q,** and **WOODBURY K A**. Dynamic material behavior modeling using internal state variable plasticity and its application in hard machining simulations. Journal of Manufacturing Science and Engineering, 2006, 128(3), 749–759.

[HAG08] **HAGLUND AJ, KISHAWY HA,** and **ROGERS RJ.** An exploration of friction models for the chip-tool interface using an arbitrary lagrangian-eulerian finite element model. Wear, 2008, 265 (3-4), 452–460.

[HAS99] **HASHIMURA M, CHANG Y P,** and **DORNFELD D.** Analysis of burr formation in orthogonal cutting. J. Mfg. Sci. Engng., 1999, 121(1), 1-7.

[HIL76] **HILLERBORG A, MODÉER M,** and **PETERSSON PE.** Analysis of crack formation and crack growth in concrete by means of fracture mechanics and finite elements. Cement and concrete research, 1976, 6, 773–782.

[IWA84] **IWATA K, OSAKADA K**, and **TERASAKA Y**. Process modeling of orthogonal cutting by the rigid-plastic finite element method. Journal of Engineering Materials and Technology, 1984, 106(2), 132–138.

[JAC00] **JACOBUS K, DEVOR R E,** and **KAPOOR S G**. Machining – induced residual stress: Experimention and modeling. Journal of manufacturing science and engineering. Transaction of the ASME, 2000, 122, 20-31.

[JBE04] **J. BENSON D** and **OKAZAWA S**. Contact in a multi-material Eulerian finite element formulation. Computer Methods in Applied Mechanics and Engineering, 2004, 193(39-41), 4277–4298.

[JIA04] **JIANG H** and **SHIVPURI R**. Prediction of chip morphology and segmentation during the machining of titanium alloys. Journal of Materials Processing Technology, 2004, 150(1-2), 124–133.

[JIN04] **JING S** and **LIU C R.** The influence of material models on finite element simulation of machining. ASME. J. Mfg. Sci. Engng., 2004, 126(4), 849-857.

[JOH84] **JOHNSON G C** and **BAMMANN D J.** A discussion of stress rates in finite deformation problems. International Journal of Solids and Structures, 1984, 20 (8), 725–737.

[JOH85A] **JOHNSON G R** and **COOK W H.** Fracture characteristics of three metals subjected to various strains, strain rates, temperatures and pressures. Engng. Fract. Mech., 1985, 21(1), 31–48.

[JOH85B] **JOHNSON K L**. Contact mechanics, Cambridge university press, Cambridge, 1985.

[JOS04] **JOSHI S S** and **MELKOTE S N**. An explanation for the size-effect in machining using strain gradient plasticity. Journal of Manufacturing Science and Engineering, 2004, 126(4), 679–684.

[KIM99] **KIM K W, LEE W Y,** and **SIN H C**. A finite element analysis for the characteristics of temperature and stress in micro-machining considering the size

effect. International Journal of Machine Tools and Manufacture, 1999, 39(9), 1507–1524.

[KLA73] **KLAMECKI B E**. Incipient chip formation in metal cutting—a three-dimensional finite element analysis. PhD thesis, University of Illinois at Urbana-Champaign, Urbana, 1973.

[KOM81] **KOMANDURI R** and **TURKOVICH B F.** New observations on the mechanism of chip formation when machining titanium alloys. Wear, 1981, 69, 179–188.

[KOM02] **KOMANDURI R** and **HOU ZB.** On thermoplastic shear instability in the machining of a titanium alloy (Ti–6Al–4V). Metallurgical and Materials Transactions A, 2002, 33, 2995–3010.

[KOU02] **KOUNTANYA R K.** Process mechanics of metal cutting with edge radiused and worn tools. PhD dissertation, 2002, University of Michigan.

[KRO61] **KRÖNER E**. on the plastic deformation of polycrystals, Acta Metall., 1961, 9, 156-165.

[LAC98] **LACOME J L**. Analyse de la méthode particulaire SPH—Application à la détonique. PhD report, Doctorat de l'INSA, Département GMMUMRMIP UPS, Toulouse, 1998.

[LAR73] **LARSEN-BASSE J** and **OXLEY P L B**. Effect of strain rate sensitivity on scale phenomena in chip formation. In: In Proceedings of 13th International Machine Tool Design and Research Conference, 1973, 209-216.

[LEE51] **LEE E H** and **SHAFFER B W**. The theory of plasticity applied to a problem of machining. ASME Jour. App. Mech., 1951, 73, 404–413.

[LEE98] **LEE W S** and **LIN C F**. Plastic deformation and fracture behaviour of Ti–6Al–4V alloy loaded with high strain rate under various temperatures. Materials Science and Engineering A, 1998, 241, 48–59.

[LES00] **LESUER D R.** Experiment investigations of material models for Ti–6Al–4V titanium and 2024-T3 Aluminum, Technical report, 2000.

[LI02] **LI K, GAO X L** and **SUTHERLAND J W.** Finite element simulation of the orthogonal metal cutting process for qualitative understanding of the effects of

crater wear on the chip formation process. Journal of Materials Processing Technology, 2002, 127 (3), 309–324.

[LEM02] **LEMAITRE J** and **CHABOCHE J L**. Mechanics of solid materials. Version 2, 2002.

[LIM07] **LIMIDOA J, ESPINOSAA C, SALAÜNA M,** and **LACOME J L**. SPH method applied to high speed cutting modeling. International Journal of Mechanical Sciences, 2007, 49 (7), 898-908.

[LIN92] **LIN Z C** and **LIN S Y.** A coupled finite element model of thermo-elastic-plastic large deformation for orthogonal cutting. J. Eng. Mater. Tech. Trans. ASME, 1992, 114, 218–226.

[LIU00] **LIU C** and **GUO YB.** Finite element analysis of the effect of sequential cuts and tool-chip friction on residual stresses in a machined layer. International Journal of Mechanical Sciences, 2000, 42 (6), 1069–1086.

[LIU06] **LIU K** and **MELKOTE S N.** Material strengthening mechanisms and their contribution to size effect in micro-cutting.-Journal of Manufacturing Science and Engineering, 2006, 128(3), 730–738.

[LO00] **LO S P**. An analysis of cutting under different rake angles using the finite element method. Journal of Materials Processing Technology, 2000, 105(1-2), 143–151.

[LUT77] **LUTTERVELT C A V** and **PEKELHARING A J.** The split shear zone - mechanism of chip segmentation. Annals of CIRP, 1977, 25 (1), 33 – 37.

[LUT03] **LUTJERING G** and **WILLIAMS JAMES C.** Titanium. Springer - Verlag, 2003.

[LUT09] **LUTHER T** and **KONKE C.** Polycrystal models for the analysis of intergranular crack growth in metallic materials. Engineering fracture Mechanics, 2009, 76, 2332-2343.

[MAB06] **MABROUKI T** and **RIGAL J F**. A contribution to a qualitative understanding of thermo-mechanical effects during chip formation in hard turning. J. Mat. Proc. Tech., 2006, 176, 214–221.

[MAB08] **MABROUKI T, GIRARDIN F, ASAD M,** and **RIGAL JF**. Numerical and experimental study of dry cutting for an aeronautic aluminium alloy (A2024 -

T351). International Journal of Machine Tools and Manufacture, 2008, 48(11), 1187–1197.

[MAL04] **MALL S, NAMJOSHI S A** and **PORTER W J.** Effects of microstructure on fretting fatigue crack initiation behavior of Ti–6Al–4V. Materials Science and Engineering A, 2004, 383(2), 334–340.

[MAT08] **MATWEB**. http://www.matweb.com/ (Access date: 2008)

[MAY04] **MAYEUR J R**. Three dimensional modeling of Titanium-Aluminium alloys with application to attachment fatigue, Georgia Institute technology, thesis, 2004.

[MAY07] **MAYEUR J R** and **MCDOWELL D L**. A three-dimensional crystal plasticity model for duplex Ti-6Al-4V. International Journal of Plasticity, 2007, 23(9), 1457–1485.

[MIL02] **MILLS K C.** Recommended values of thermo physical properties for selected commercial alloys, Abington Hall, Abington, Cambridge, Woodhead Publishing Limited, 2002.

[MER44] **MERCHANT E**. Basic mechanics of the metal-cutting process. Transaction of the ASME, Jour. App. Mech., 1944, 66, 168–175.

[MUR04] **MURTAGIAN G R**. Surface integrity on grinding of Gamma Titanium Aluminide intermetallic compounds. Thesis, Georgia institutive of technology, 2004.

[MOV00] **MOVAHHEDY M, GADALA M S,** and **ALTINTAS Y**. Simulation of the orthogonal metal cutting process using an arbitrary Lagrangian - Eulerian finite-element method. Journal of Materials Processing Technology, 2000, 103(2), 267–275.

[MUR87] **MURA T**. Micromechanics of defects in solids. Second revised version, Dordrecht, The Netherlands:Martinus Nijhoff Publishers, 1987.

[NAS07] **NASR M N A, Ng E G**. Elbestawi M A. Modelling the effects of tool-edge radius on residual stresses when orthogonal cutting AISI 316L. International Journal of Machine Tools & Manufacture, 2007, 47, 401–411.

[OBI96] **OBIKAWA T** and **USUI E**. Computational machining of titanium alloy—finite element modeling and a few results. Journal of Manufacturing Science and Engineering, 1996, 118(2), 208–215.

[OBI97] **OBIKAWA T, SASAHARA H, SHIRAKASHI T,** and **USUI E**. Application of computational machining method to discontinuous chip formation. Journal of Manufacturing Science and Engineering, 1997, 119(4B), 667–674.

[OBI00] **OBIKAWA T, YAMANE Y, CHILDS T H C,** and **MAEKAWA K**. Metal machining: theory and applications. Arnold, Paris, 2000.

[OBI09] **OBIKAWA T, TAKEMURA Y, AKIYAMA Y, SHINOZUKA J,** and **SASAHARA H**. Microscopic phase-dependent residual stresses in the machined surface layer of two-phase alloy. Journal of Materials Processing Technology, 2009, 209(9), 4496–4501.

[OHB05] **OHBUCHI Y** and **OBIKAWA T**. Adiabatic shear in chip formation with negative rake angle. International Journal of Mechanical Sciences, 2005, 47(9), 1377–1392.

[OKU72] **OKUSHIMA K** and **KAKINO Y**. A study of residual stress produced by cutting. Mem. Fac. Eng., Kyoto Univ., Jpn., 1972, 34, 234 - 248.

[ÖZE00] **ÖZEL T** and **ALTAN T**. Process simulation using finite element method – prediction of cutting forces, tool stresses and temperatures in high-speed flat end milling. International Journal of Machine Tools and Manufacture, 2000, 40(5), 713–738.

[ÖZE06] **ÖZEL T**. The influence of friction models on finite element simulations of machining. International Journal of Machine Tools and Manufacture, 2006, 46(5), 518–530.

[OWE99] **OWEN D R J** and **VAZ M.** Computational techniques applied to high-speed machining under adiabatic strain localization conditions. Computer Methods in Applied Mechanics and Engineering, 1999, 171 (3-4), 445–461.

[PIR03] **PIRONDI A** and **BONORA N.** Modeling ductile damage under fully reversed cycling. omputational Materials Science, 2003, 26, 129–141.

[PRA11] **PRASAD K** and **KUMAR V**. Isothermal and thermo mechanical fatigue behaviour of Ti–6Al–4V titanium alloy, Materials Science and Engineering A, 2011, 528, 6263–6270.

[PUE07] **PUERTA VELÁSQUEZ JD, BOLLE B, CHEVRIER P, GEANDIER G,** and **TIDU A**. Metallurgical study on chips obtained by high speed machining of a Ti-6 wt.%Al-4 wt.%V alloy. Materials Science and Engineering: A., 2007, 452-453, 469–474.

[RAC04] **RACZY A, ELMADAGLI M, ALTENHOF W,** and **ALPAS A**. An eulerian finite-element model for determination of deformation state of a copper subjected to orthogonal cutting. Metallurgical and Materials Transactions A, 2004, 35(8), 2393-2400.

[RAM02] **RAMESH A.** Prediction of process-induced microstructural changes and residual stresses in orthogonal hard machining. PhD dissertation, 2002, Georgia Institute of Technology.

[RAN09] **RANDLE V** and **ENGLER** O. Introduction to Texture Analysis Macrotexture, Microtexture, and Orientation Mapping. CRC Press, 2009.

[REC64] **RECHT R F.** Catastrophic thermoplastic shear. J. app. Mech, 1964, 86, 189-193.

[REC04] **RECH J, CALVEZ C L,** and **DESSOLY M.** A new approach for the characterization of machinability–application to steels for plastic injection molds. Journal of Materials Processing Technology, 2004, 152(1), 66–70.

[SAA09] **SAANOUNI K, LESTRIEZ P,** and **LABERGERE C.** 2D adaptive FE simulations in finite thermo-elasto-viscoplasticity with ductile damage: Application to orthogonal metal cutting by chip formation and breaking. International Journal of Damage Mechanics, 2009. doi: 10.1177/1056789509343688

[SAN11] **SANDVIK**. www.sandvik.coromant.com. (Accessed February 2011)

[SAV04] **SAVAGE M F, TATALOVICH J,** and **MILLS M J**. Anisotropy in the room temperature deformation of α-β colonies in titanium alloys: role of the α-β interface. Philosophical Magazine, 2004, 84 (11), 1127 – 1154.

[SCH00] **SCHIMMEL R J, MANJUNATHAIAH J,** and **ENDRES W J.** Edge radius variability and force measurement considerations. ASME, J. Mfg. Sci. Engng., 2000, 122(3), 590-593.

[SCH02] **SCHMAUDER S**. Computational mechanics. Annu. Rev. Mater. Res, 2002, 32, 437–65.

[SEM83] **SEMIATIN S L** and **RAG S B.** Shear localization during metal cutting. Journal of Materials Science and Engineering, 1983, 61, 185–192.

[SHA54] **SHAW M C, DIRKE S O, SMITH P A, COOK N H, LOEWEN E G,** and **YANG C T.** Machining titanium. In: MIT report, Massachusetts Institute of Technology, 1954.

[SHA84] **SHAW M C**. Metal Cutting Principles. Clarendon Press, Oxford, 1984.

[SHE03] **SHET C** and **DENG X**. Residual stresses and strains in orthogonal metal cutting. International Journal of Machine Tools and Manufacture, 2003, 43(6), 573–587.

[SHI74] **SHIRAKASHI T** and **USUI E**. Simulation analysis of orthogonal metal cutting mechanism. Proceedings of the first international conference on production engineering, Tokyo, Part I, pages 535–540, 1974.

[SHI90] **SHIH A J, CHANDRASEKAR S,** and **YANG H T.** The finite element simulation of metal cutting processes with strain-rate and temperature effects. ASME Publication PED, 1990, 43, 11–24.

[SHI02] **SHI G Q, DENG XM,** and **SHET C.** A finite element study of the effect of friction in orthogonal metal cutting. Finite Elements in Analysis and Design, 2002, 38(9), 863–883.

[SIM98] **SIMO J C** and **HUGHES T J R.** Computational Inelasticity, Springer-Verlag, New York, 1998.

[SIM06A] **SIMONEAU A, NG E** and **ELBESTAWI M A**. Chip formation during microscale cutting of a medium carbon steel. International Journal of Machine Tools and Manufacture, 2006, 46(5), 467–481.

[SIM06B] **SIMONEAU A, NG E** and **ELBESTAWI M A**. Surface defects during microcutting. International Journal of Machine Tools and Manufacture, 2006, 46(12-13), 1378–1387.

[SIM10] **SIMA M** and **ÖZEL T.** Modified material constitutive models for serrated chip formation simulations and experimental validation in machining of titanium alloy Ti-6Al-4V. International Journal of Machine Tools and Manufacture, 2010, 50(11), 943–960.

[SLA11] **SLAK T** and **SADEGHI, F**. Cohesive zone modeling of intergranular fatigue damage in rolling contacts. Tribology international, 2011, 44, 797-804.

[SUB08] **SUBBIAH S** and **MELKOTE S N.** Effect of finite edge radius on ductile fracture ahead of the cutting tool edge in micro-cutting of Al2024-T3. Mater. Sci. Engng. A, 2008, 474(1-2), 283–300.

[SUF03] **SUFFIS A**, **LUBRECHT T AA**, and **COMBESCURE A**. Damage model with delay effect analysis and numerical studies of the evolution of the characteristic damage length. International journal of solids and structures, 2003, 40, 3463-3476.

[SUN09a] **SUN S, BRANDT M,** and **DARGUSCH M S.** Characteristics of cutting forces and chip formation in machining of titanium alloys. International Journal of Machine Tools and Manufacture, 2009, 49(7-8), 561–568.

[SUN09b] **SUN J** and **GUO YB.** A comprehensive experimental study on surface integrity by end milling Ti-6Al-4V. Journal of Materials Processing Technology, 2009, 209, 4036–4042.

[ULU11] **ULUTAN D** and **OZEL T**. Machining induced surface integrity in titanium and nickel alloys: A review. International Journal of Machine Tools & Manufacture, 2011, 51, 250-280.

[UMB04] **UMBRELLO D, HUA J,** and **SHIVPURI R.** Hardness-based flow stress and fracture models for numerical simulation of hard machining AISI 52100 bearing steel. Mater. Sci. Engng. A, 2004, 374(1-2), 90–100.

[UMB08] **UMBRELLO D**. Finite element simulation of conventional and high speed machining of Ti-6Al-4V alloy. Journal of Materials Processing Technology, 2008, 196 (1-3), 79–87.

[USU82] **USUI E** and **SHIRAKASHI T**. Mechanics of machining-from "descriptive" to "predictive" theory. In: Proceedings of the winter annual meeting of the American Society of Mechanical Engineers. PED. ASME, New York, 1982, l7, 13-35.

[VAZ01] **VAZ M** and **OWEN D R J**. Aspects of ductile fracture and adaptive mesh refinement in damaged elasto-plastic materials. Int. J. Numer. Meth. Engng., 2001, 50(1), 29–54.

[VAZ07] **VAZ JR M, OWEN D R J, KALHORI V, LUNDBLAD M,** and **LINDGREN L M.** Modelling and simulation of machining processes. Arch. Comput. Methods Engng., 2007, 14(2), 173-204.

[VYA99] **VYAS A** and **SHAW M C.** Mechanics of saw-tooth chip formation in metal cutting. Journal of Manufacturing Science and Engineering, 1999, 121(2), 163–172.

[WAN08] **WANG JS, GONG YD, ABBA G, CHEN K, SHI JS** and **CAI GQ**. Surface generation analysis in micro end-milling considering the influences of grain. Microsyst Technol, 2008, 14, 937–942.

[WEN06] **WEN Q, GUO Y B,** and **TODD B A.** An adaptive FEA method to predict surface quality in hard machining. J. Mater. Processing Technol., 2006, 173(1), 21–28.

[XU94] **XU X P** and **NEEDLEMAN A**. Numerical simulations of fast crack growth in brittle solids. Journal of the Mechanics and Physics of Solids, 1994, 42(9), 1397–1434.

[YAN02] **YANG X and LIU C R.** A new stress based model of friction behaviour in machining and its significant impact on residual stresses. Int. J. Mech. Sci., 2002, 44, 703–723.

[ZHA08] **ZHANG M.** CRYSTAL PLASTICITY MODELING OF TI-6AL-4V AND ITS APPLICATION IN CYCLIC AND FRETTING FATIGUE ANALYSIS. PhD thesis, Georgia Institute of Technology, April 2008.

[ZHA11] **ZHANG Y, UMBRELLO D, MABROUKI T, RIZZUTI S, NELIAS D,** and **GONG Y.** On methodologies inside two different commercial codes to simulate the cutting operation. Advanced Materials Research, 2011, 223, 162-171. CIRP Conference on Modeling of Machining Operations, Sintra, Portugal.

[ZOR63] **ZOREV N N**. Inter-relationship between shear processes occurring along tool face and shear plane in metal cutting, international research in production engineering. ASME, 1963, 42 – 49.

FOLIO ADMINISTRATIF

THESE SOUTENUE DEVANT L'INSTITUT NATIONAL DES SCIENCES APPLIQUEES DE LYON

NOM : ZHANG DATE de SOUTENANCE : September 29, 2011

Prénoms : Yancheng

TITRE : Numerical simulation approaches and methodologies for multi-physic comprehensions of Titanium alloy (Ti-6Al-4V) cutting

NATURE : Doctorant Numéro d'ordre : 2011ISAL0098

Ecole doctorale : MECANIQUE, ENERGETIQUE, GENIE CIVIL, ACOUSTIQUE (MEGA)

Spécialité : Mécanique

RESUME :
The objective of this study is to model material removal with cutting tool in the case of the machining of Titanium alloy (Ti–6Al–4V) and to bring a multi-physic comprehension of chip formation and the tool/workpiece interaction by adopting finite element approaches and methodologies.
For that, the present contribution begins by a macroscopic modeling of the orthogonal cutting process. The cut material behavior considered is supposed based on JC law. Moreover, in order to simulate properly the chip genesis, the material fracture energy concept is adopted for controlling the material damage evolution. This allows capturing the shear strain localization and consequently the chip segmentation for a given set of cutting parameters. The frictional contact model considers the influence of temperature on the limiting shear stress at the tool/chip interface. As a result, this reliable model has the capability to simulate the cutting process even with high coefficient of friction and with large cutting edge radius. The parametric study carried out by referring to this model shows a very interesting corroboration with experimental results.
In a second step, the present research work presents a material microstructure-level cutting model (MML cutting model) for cutting simulation. The crystal plasticity theory is adopted for modeling the cutting of the Titanium alloy Ti–6Al–4V in orthogonal case. In this model, the grains of the studied material are explicitly considered, and their orientation angles and slip system strength anisotropy are considered as the main source of the microstructure heterogeneity in the cutting material. To simulate the material degradation process, the continuum intra-granular damage and discrete cohesive zone inter-granular damage models are developed, wherein the zero thickness cohesive elements are implemented to simulate the bond between grain interfaces. The material model is validated by a comparison of compression tests from literature.
Finally, simulation results demonstrate the possibility to capture the influence of the microstructure on the material removal in terms of chip formation. It is demonstrated that the grain orientation angle plays an important role for the chip segmentation and its periodicity during the cutting process. This certainly can affect the evolution of the cutting force. Additionally, the surface integrity is discussed based on the MML cutting model for different cutting speeds and feed rates. Indeed, a parametric study shows that the surface integrity is seriously affected by the machining parameters, and the affected region is limited within three layer grains for the present MML cutting model.

MOTS-CLES :Finite element simulation, Orthogonal cutting model, Johnson-Cook, Fracture energy, Damage evolution, Limiting shear stress, Material microstructure-level cutting model (MML cutting model), Crystal plasticity, Intra-granular damage model, Inter-granular damage model, Vumat user routine, Ti–6Al–4V, Surface integrity.

Laboratoire (s) de recherche :

Laboratoire de Mécanique des Contacts et des Structures

Directeur de thèse:
Tarek MABROUKI, Daniel NELIAS

Président de jury :

Composition du jury :
Amine AMMAR, Olivier CAHUC, Domenico UMBRELLO, Hédi HAMDI, Jean François RIGAL, Mathias SEVE, Tarek MABROUKI, Daniel NELIAS